

University of New Hampshire

University of New Hampshire Scholars' Repository

Doctoral Dissertations

Student Scholarship

Summer 1973

A DATA UNFOLDING TECHNIQUE AS APPLIED TO ULTRASOFT X-RAY DETECTORS UTILIZED IN A SOUNDING ROCKET EXPERIMENT

JOHN THOMAS APOSTOLOS

Follow this and additional works at: <https://scholars.unh.edu/dissertation>

Recommended Citation

APOSTOLOS, JOHN THOMAS, "A DATA UNFOLDING TECHNIQUE AS APPLIED TO ULTRASOFT X-RAY DETECTORS UTILIZED IN A SOUNDING ROCKET EXPERIMENT" (1973). *Doctoral Dissertations*. 1033. <https://scholars.unh.edu/dissertation/1033>

This Dissertation is brought to you for free and open access by the Student Scholarship at University of New Hampshire Scholars' Repository. It has been accepted for inclusion in Doctoral Dissertations by an authorized administrator of University of New Hampshire Scholars' Repository. For more information, please contact Scholarly.Communication@unh.edu.

74-7028

APOSTOLOS, John Thomas, 1942-
A DATA UNFOLDING TECHNIQUE AS APPLIED TO
ULTRA-SOFT X-RAY DETECTORS UTILIZED IN A
SOUNDING ROCKET EXPERIMENT.

University of New Hampshire, Ph.D., 1973
Physics, general

University Microfilms, A XEROX Company, Ann Arbor, Michigan

A DATA UNFOLDING TECHNIQUE AS APPLIED TO ULTRA-SOFT
X-RAY DETECTORS UTILIZED IN A SOUNDING ROCKET EXPERIMENT

by

JOHN T. APOSTOLOS

A THESIS

Submitted to the University of New Hampshire

In Partial Fulfillment of

The Requirements for the Degree of

Doctor of Philosophy

Graduate School

Department of Physics

AUGUST, 1973

This thesis has been examined and approved

Robert E. Houston

W R Webber

L. C. Balling

Reuch. N. Jr. Ory

Richard E. Cole

25 June 1973

Date

ACKNOWLEDGEMENTS

The author wishes to thank his adviser, Dr. Robert E. Houston, Jr., for inspiration and guidance during this study.

Thanks are also in order to L. A. Friling and R. Simmons for payload development and support, and to A. Knight and A. Anderson for aid with the machine work.

Mrs. June Spinney was responsible for the typing.

TABLE OF CONTENTS

Acknowledgments	i
Table of Contents	ii
List of Figures	iv
Abstract	vii
I. INTRODUCTION	1
II. UNFOLDING	7
1. Popular Techniques	8
2. Power Spectrum Analysis in Communication Theory	12
3. Kernal Modification	16
4. Absorption Photon Detector	20
5. Implementation of the Kernal Modification	26
III. PHOTON DETECTION TECHNIQUES	45
1. Photoemission	45
2. General Design of Detectors	58
3. Detectors with Low Resolution Capability	62
IV. ULTRA-SOFT X-RAY DETECTOR	67
1. Geometry	67
2. Detector Characteristics	73
a. Angular Response	73
b. Photocathodes	73
c. Absorbers	78
d. Spectral Response	78
3. Electronics	80
4. Calibration	90

V. SOUNDING ROCKET FLIGHT	99
1. Objective	99
2. Payload	101
3. Results	101
VI. CONCLUSION	112
VII. BIBLIOGRAPHY	113
APPENDIX	116

LIST OF FIGURES

Figure 1	Direct Solutions to the Integral Equations for Orders 1, 3, and 20, for a line Source	11
Figure 2	A Filter as a Two Port Device	15
Figure 3	Power Spectrum/Unfolding Analogy	16
Figure 4	Comparison of Legendre Windows	27
Figure 5	Typical Photon Absorber Detector Data	28
Figure 6	Legendre Solution of a Two Component Spectrum .	30
Figure 7	Fractional Error Allowed in the Data for a Required Resolution	33
Figure 8	No. of Absorbers Vs. % Resolution Possible	34
Figure 9	Raw Data from Fe ⁵⁵ - Co ⁵⁷ Sources	36
Figure 10	Decomposition of Fe ⁵⁵ - Co ⁵⁷ Source	38
Figure 11	34 Å Window	40
Figure 12	50 Å Window	41
Figure 13	70 Å Window	42
Figure 14	100 Å Window	43
Figure 15	Absorption Coefficient of Al	44
Figure 16	Photocathode Geometry	47
Figure 17	Photocathode Geometry for Large Grazing Angles and/or High Energies	47
Figure 18	Al Photocathode Efficiency	51
Figure 19	Multiple Reflection - Absorption Photocathode .	51
Figure 20	Photoelectric Yield of CsI, LiF	54

Figure 21	Efficiency of Various Alkali Halides	55
Figure 22	Average Efficiency of MgF ₂ Sheets Set at a Grazing Angle of 20° (Aug., 1971, NRL) ...	56
Figure 23	Aging of MgF ₂ and LiF	57
Figure 24	Effect of Alkali Coatings	57
Figure 25	Multiple Photocathode Config.....	59
Figure 26	Electron Collection Scheme	59
Figure 27	Conic Photocathode	60
Figure 28	Collimation-Deflection Plate Configuration	60
Figure 29	Multiple Reflection-Absorption Photocathodes ..	60
Figure 30	Low Pass Reflector Detector	61
Figure 31	Critical Angle of Reflection Vs. Photon Energy for Aluminum	63
Figure 32	Low Pass Detector Configuration	64
Figure 33	Low Pass CR. Reflector Filter	64
Figure 34	Band Pass Reflector	66
Figure 35	Basic X-Ray Detector	68
Figure 36	X-Ray Detector Electron Collection	69
Figure 37	Detector (H.V. Side)	71
Figure 38	Detector (Electronics Side)	72
Figure 39	Detector Calculated Angular Response	74
Figure 40a	Photocathode	75
Figure 40b	Absorbers	75
Figure 41	Efficiency of MgF ₂ (5-100Å)	76

Figure 42	Efficiency of MgF_2 (100-3000 Å)	77
Figure 43	Detector U-V Response	79
Figure 44	Carbon-Absorber — Photocathode Response	81
Figure 45	Spiraltron Electron Gain	82
Figure 46	Spiraltron Output Current	82
Figure 47	Pulse Counting Circuit	83
Figure 48	Block Diagram of Electronics	85
Figure 49	Post Pre-Amp Electronics	86
Figure 50	Pre-Amp and Scale Compressor	87
Figure 51	Scale Compression Amplifier	89
Figure 52	Pulse Rate Vs. Compression Amp Output	89
Figure 53	3500 Å Aluminum Bin	93
Figure 54	2500 Å Aluminum Bin	94
Figure 55	1500 Å Aluminum Bin	95
Figure 56	500 Å Aluminum Bin	96
Figure 57	Lyman α Intensity	103
Figure 58	5-30 Å Solar X-Ray Intensity	104
Figure 59	Rocket Altitude	105
Figure 60	Solar Spectrum of the Top of the Atmosphere ...	107
Figure 61	D(H) Vs. Altitude	108
Figure 62	Transmission of 25 Å X-Rays as a Function of Altitude	109
Figure 63	Theoretical and Experimental Absorption	110
Figure 64	Graph of Kernal K_{mod}^{10}	131

AN ABSTRACT OF
A DATA UNFOLDING TECHNIQUE AS APPLIED
TO ULTRA-SOFT X-RAY DETECTORS UTILIZED
IN A SOUNDING ROCKET EXPERIMENT

by

JOHN T. APOSTOLOS

A technique of unfolding data and the detection of photons in the 10-400^oÅ wavelength range using external photoelectric devices are discussed. These techniques are used in the design and construction of a 5-150^oÅ ultra-soft x-ray detector system (described in detail) for a sounding rocket experiment in which x-ray flux from the sun in the upper D and lower E region of the ionosphere was measured.

CHAPTER I

INTRODUCTION

The motivation for the development of a rocket borne 5-150Å x-ray detector was the need for solar x-ray data in the D and E regions of the ionosphere. Byram et al. [1], Friedman [2], Friedman [3], Hinteregger [4], Hinteregger [5], Drake [6], Sengupta [7], Sengupta [8], and Grader et al. [10] have measured (or reported on measurements of) solar x-rays in certain bands in the 2-100Å wavelength range. The Friedman group [1-3] has developed detectors in the 2-8Å, 44-60Å, and 44-100Å regions, but later efforts by this group [2-3] do not cite the data from the 44-100Å detector, apparently because of experimental difficulties with the glyptal window. None of these detectors was completely shielded from the intense ultra-violet radiation ($\lambda > 2000\text{Å}$), a point Friedman [2] emphasizes. Hinteregger [4-5] uses a grating spectrometer to obtain his results which are excellent in the 500-1300Å range, but below 300Å Hinteregger [4] observes that the measurements are uncertain by as much as a factor of ten. Van Allen's group [6-8] reports on 2-12Å x-rays measured on Explorer 33 and Explorer 35 at distances ranging from 32,000 km to 859,000 km for Explorer 33 and at least 250,000 miles for Explorer 35 as it is in lunar orbit. In addition, Van Allen's detectors (as Friedman's) may not be completely shielded against the u-v radiation. Cornell et al. [9]

and Grader [10] have constructed flow-through proportional counters, but they do not report data below 140 km, a distance well outside the D region. Aitken [11] gives a summary of the various detectors and their limitations. The information from these reports indicates that accurate measurements of solar x-rays below 100 km do not exist in the 5-150 $\overset{\circ}{\text{A}}$ range, and that many of the fluxes reported above 100 km by the previously mentioned investigators may well be contaminated by u-v radiation.

An experiment designed to measure electron densities and some of the associated radiations producing the electrons in the D and E regions of the ionosphere was developed for the Goddard Space Flight Center/National Aeronautics and Space Administration's Mobile Launch Expedition in 1964 (Larson [12]). A 2-8 $\overset{\circ}{\text{A}}$ Geiger-Muller x-ray detector was utilized primarily to determine if ionospheric conditions were quiet or disturbed at the time of any particular rocket flight. Current theory (Sengupta [7]) holds that solar x-rays in the 10-100 $\overset{\circ}{\text{A}}$ range are primarily responsible for the formation of a major portion of the E region ionization. A relatively constant Lyman α radiation produces the steady state D region electrons while 1-10 $\overset{\circ}{\text{A}}$ x-rays, which are markedly enhanced during solar flares, are thought to cause large increases in D region electron density during disturbed solar conditions.

Because of the importance of 5-150 $\overset{\circ}{\text{A}}$ x-rays in ionospheric electron production and the lack of reliable flux information in this range, it was decided to attempt to design, construct, and fly a new type of x-ray detector which could

operate in the D and lower E regions in the 5-150 $\overset{\circ}{\text{A}}$ range. The detector was to be allowed only a small portion of a Nike-Tomahawk payload space (less than one cu. ft.), and only three telemetry channels.

It was essential to develop a new technology, in view of the fact that all the previously flown x-ray detectors did not have adequate u-v rejection. Some degree of energy resolution for 5-150 $\overset{\circ}{\text{A}}$ photons was deemed essential to the experiment, and it was also decided to make the x-ray detector capable of detecting weak x-ray sources (x-ray stars) since low energy data ($\lambda > 70\overset{\circ}{\text{A}}$) from such sources would be extremely useful. Once above the atmosphere (200 km), it was reasoned that the x-ray scattering from the sun would be small [13], thus permitting observation of stellar sources. This required versatility compounded the detector problem since the x-ray flux from the sun can reach 10^9 photons/second/cm² in the 5-150 $\overset{\circ}{\text{A}}$ range while that expected from a stellar x-ray source is the order of 200 photons/second/cm² or less.

Ultrasoft x-ray (10-100 $\overset{\circ}{\text{A}}$) and extreme vacuum ultraviolet (100-500 $\overset{\circ}{\text{A}}$) photon detection techniques are quite different from techniques applicable in other spectral regions. The high absorption properties of all materials in this region dictate the use of windowless detectors; that is, detectors which do not require enclosures as do Geiger or proportional counters. The detectors must also be extremely insensitive to ultra-violet radiation since the u-v ($\lambda > 2000\overset{\circ}{\text{A}}$) usually is orders of magnitude more intense than the x-rays. Photoelectric detectors, in which quanta incident upon a photo-

cathode produce photoelectrons and secondary electrons which are detected by some type of electron detector, are the only practical devices. Gas flow proportional counters can be used for $\lambda < 80\text{\AA}$, but require a constant replenishment of gas, and are usually sensitive to u-v radiation.

The goal of deducing the energy spectrum of the photons with a photoelectric detector provided motivation for a new technique in which the incident spectrum could be unfolded using a series of absorber windows. The energy resolution using this unfolding technique is shown to be comparable to the resolution of gas proportional counters [9,10], which rely upon the relationship between the number of ion-electron pairs produced by a photon and the photon's energy. Typical values of energy resolutions of proportional counters in the range 50-150 \AA lie between 50-150%.

The photoelectric detector can basically be relied upon only for photon counting, since there is only a weak tie between the energy of the secondary electrons and the photoelectron [14]. In order to obtain information about the incident photon spectrum, some means of modifying the energy response of the photon detection is necessary. A simple, but effective, way to modify the response is the use of a time varying absorber thickness in front of the photon counter. The 5-150 \AA x-ray detector was therefore modeled on this varying absorber principle; however in actual practice four different thicknesses of absorber were used for a relatively low resolution (50%) capability. Unfolding the incident

spectrum with such an arrangement of absorber thickness is found to be a special case of the problem of solving the Fredholm [15] integral equation of the first kind. The Fredholm equation can be stated in the following form:

$$D(t) = \int_a^b k(t,E) I(E) dE$$

where $D(t)$ is the data as a function of absorber thickness, $k(t,E)$ is the detector response, and $I(E)$ is the incident energy spectrum. The main difficulty in the solution of $I(E)$ is the insensitivity of $D(t)$ to changes in $I(E)$; or conversely, the property that small changes in $D(t)$ can effect a large change in $I(E)$. Hence, the success of the solution depends, to a large extent, on the accuracy of the data.

While the Fredholm equation has been studied by a large number of people in recent years [16], almost all of the techniques start with a matrix approximation of the Fredholm equation. These matrix techniques are not general, and almost always require a priori information about the spectrum.

The author has chosen to approach the problem in a more general manner analogous to the techniques used in communications theory. These techniques of power spectrum analysis can be best classified as a form of numerical or digital filtering. The power of this new approach is that with no a priori knowledge of the spectrum, the maximum amount of information about the spectrum can be extracted from the data. This technique of unfolding is used to achieve the

low resolution capability of a rocket borne 5-150⁰A x-ray detector, and also is used in a ground based unfolding experiment using higher energy x-ray lines.

Because of the basic importance of the unfolding technique, it is the topic discussed first in the thesis in Chapter II. Those who are primarily interested in instrumental details are referred to Chapter III for general consideration of ultra-soft x-ray photon detection and to Chapter IV for details of the 5-150A ultra-soft x-ray detector.

CHAPTER II

UNFOLDING

The decomposition of a continuous spectrum is complicated by problems related to the experimental errors in the observed data itself. Solving for the actual input spectrum using the spectrally distorted detector data, which is usually distorted as a result of finite resolving power, has become known as unfolding. The equation associated with most unfolding problems is the one-dimensional Fredholm equation of the first kind [15],

$$D(t) = \int_a^b k(t,E) I(E) dE$$

where $D(t)$ is the data, usually the intensity distribution of a physical observable, $k(t,E)$ is the response of the detector, and $I(E)$ is the unknown spectrum. Since the prime spectrum of interest in this work is the solar photon energy spectrum, it is judicious to derive the actual integral equation which must be solved.

If a source of photons stationary in time existed, and one were able to count each photon emitted and measure its energy exactly over an infinite period of time, an energy distribution $dN/dE(E)$ could be defined such that

$$\delta N = \frac{dN}{dE} \delta E$$

where δN is the number of photons/sec emitted between energies E and $E + \delta E$. That the source be stationary means that finite observation periods separated in time should give the same statistical results; that is, the energy probability distribution function (probability that a photon emitted is in a specified energy range) does not change with time. Let $k(t, E)$ be a physical transfer function which is the probability that a photon of energy E will be detected. In the case of the actual photon detector; t , the parameter which effects this probability, is the thickness of an absorber.

$$\delta N(t) = k(t, E) \frac{dN}{dE} (E) \delta (E)$$

Since a finite observation period is available, the data from an interval of energy $E, E + \delta E$ is

$$\delta D(t) = k(t, E) \frac{dN}{dE} \delta E + \delta E_r(t)$$

where $E_r(t)$ is the statistical error. And therefore,

$$\int \delta D(t) = D(t) = \int_0^{\infty} k(t, E) \frac{dN}{dE} dE + E_r(t).$$

If one assumes a Poisson distribution, the error should be $\sqrt{N(t)}$ where $N(t)$ is the total number of counts accumulated for the value t .

1. Popular Techniques

Most of the available literature in the past few years [16-27] approaches the unfolding problem with a matrix formulation; that is, the Fredholm equation is usually approximated by a linear system of equations. The interval of

integration is divided up into N segments and approximated by the following expression:

$$\sum_{i=1}^N k_{ji} w_i \left(\frac{dN}{dE} \right)_i = D_j + E_j$$

where $\{ w_i \}$ are the weights that depend upon the integration quadrature formula chosen, k_{ji} is equal to $k(t_j, E_i)$, $\left(\frac{dN}{dE} \right)_i$ is equal to $\frac{dN}{dE}(E_i)$, D_j is equal to $D(t_j)$, and E_j is equal to $E(t_j)$. In matrix notation,

$$(1) \quad [A] \left[\frac{dN}{dE} \right] = [D] + [E]$$

where $\left[\frac{dN}{dE} \right]$, $[D]$ and $[E]$ are column vectors.

The exact solution of equation (1) is:

$$(2) \quad \left[\frac{dN}{dE} \right] = [A]^{-1} [D] + [A]^{-1} [E]$$

The order N of the matrix representation is to some extent arbitrary. The larger N becomes the more closely the matrix equation approximates the original integral equation, but the matrix $[A]$ may become "ill conditioned"; that is, $[A]^{-1}$ will possess elements that become exceedingly large. As a result of the growth of the elements of $[A]^{-1}$, the error vector $[A]^{-1} [E]$ may not become small for arbitrarily large N . It is usually found that as N increases, the solutions first become more accurate but then eventually become worse for physically realizable accuracy in the data. It has been shown that numerical solutions of the Fredholm equation are not only

non-unique, but may also be subject to severe oscillations [18]. An example of a severe oscillation in a solution has been worked out by the author. The equation

$$D(t) = \int_0^{\infty} e^{-\mu \rho t} I(\mu) d\mu$$

has been directly solved numerically in the form of a weighted summation over the derivatives of the data. The result for $I(\mu)$ equal to a line source for which the data is the function e^{-e^x} is pictured on the next page, while the calculations and a complete explanation of the graphs are presented in Appendix B (F^{ℓ} corresponds to the ℓ^{th} derivative of the data).

It follows that one does not always desire the "exact" solution as given by (2), but more properly seeks a vector which satisfies equation (1), together with certain subsidiary conditions. Such a solution is usually called an appropriate solution. The matrix formulation unfolding techniques fall into three categories:

1. Iteration [20]
2. Least Squares [16]
3. Smoothing Methods [16,26]

The iterative technique attempts to generate successive approximations which converge to an appropriate solution.

The least squares method expands $\frac{dN}{dE}$ with a set of functions $\psi_i(E)$ such that $\left(\frac{dN}{dE}\right) = W(E) \sum_i a_i \psi_i$. Substituting $\frac{dN}{dE}$ into the Fredholm equation minus the errors, one obtains $D_j = \sum_{i=1}^N a_i S_{ji}$ where $S_{ij} = \int k_j(E) W \psi_i de$. The quantity to be minimized is

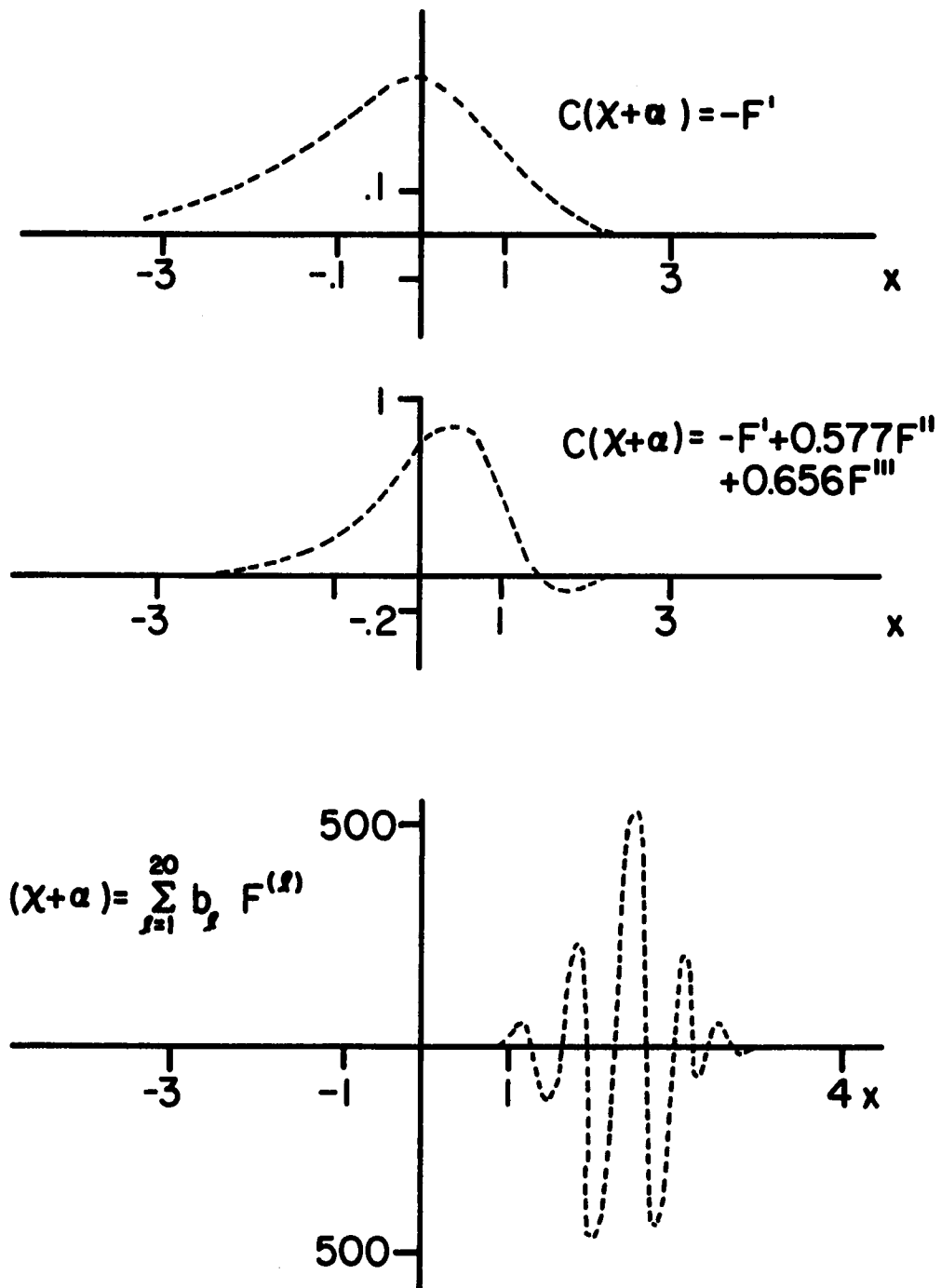


FIG. 1--DIRECT SOLUTIONS TO THE INTEGRAL EQUATION FOR ORDERS 1, 3, AND 20 FOR A LINE SOURCE

$$Q = \sum_{j=1}^m \left(D_j - \sum_{i=1}^N a_i S_{ji} \right)^2$$

Least squares techniques require some a priori knowledge of the spectrum in the form of an appropriate function describing the spectrum. Smoothness techniques consist in finding the solution of

$$\sum_{i=1}^N K_{ji} W_i \left(\frac{dN}{dE} \right)_i = D_j + E_j$$

which minimizes the quantity

$$\sum_{j=1}^m E_j^2 = \sum_{j=1}^m \left(\sum_{i=1}^N a_{ji} \left(\frac{dN}{dE} \right)_i - D_j \right)^2$$

subject to smoothness constraints.

The ability of any of these methods to provide appropriate solutions can be verified only through testing and experience.

2. Power Spectrum Analysis in Communications Theory

It is worthwhile to review the fundamentals of power spectrum analysis in communications theory. Such a study will provide the motivation and insight for the unfolding technique described in the next section.

A filter is a device or physical process that operates on a time history and usually changes the time history in some manner.

The most basic mathematical conception of a filter results by use of the unit impulse response function and the convolution integral. If $x(t)$ is the unfiltered time history and $v(t)$

is the output of the filter (Figure 2), then

$$(3) \quad v(t) = \int_{-\infty}^{\infty} h(\lambda) x(t-\lambda) d\lambda$$

where $h(\lambda)$ is the unit impulse response function (for example, see Ref. [28-30]). The input voltage, $v(t)$, is expressible as a Fourier integral of the form

$$(4) \quad x(t) = \int_{-\infty}^{\infty} g(f) e^{j2\pi ft} df$$

where f is the frequency variable. Multiplying both sides of the above equation by $x(t)$; then integrating with respect to t ; and then using Parseval's theorem; one obtains

$$(5) \quad \int_{-\infty}^{\infty} x^2(t) dt = \int_{-\infty}^{\infty} |g(f)|^2 df$$

Since $x(t)$ is a voltage, the left hand side of (5) represents the total energy of the disturbance $x(t)$. It is then possible to interpret $|g(f)|^2$ as an energy density on the frequency scale; i.e., the spectrum of $x(t)$.

An important way of defining the power spectrum is by use of a filter [31]. If the input voltage $x(t)$ is passed through the filter $h(\lambda)$ (Figure 2) for only a finite time, equation (3) becomes

$$v(t) = \int_{-T}^T h(\lambda) x(t-\lambda) d\lambda$$

Substitution of equation (4) into the above expression yields

$$v(t) = \int_{-\infty}^{\infty} df e^{j2\pi ft} g(f) \left[\int_{-T}^T d\lambda h(\lambda) e^{-2\pi f\lambda j} \right]$$

Using Parseval's theorem the above becomes

$$(6) \quad \int_{-T}^T v^2(t) = W_V = \int_{-\infty}^{\infty} |g(f)|^2 |H(f,h)|^2 df$$

where W_V is the power spectrum of the filter output voltage $v(t)$, and

$$H(f,h) = \int_{-T}^T d\lambda h(\lambda) e^{-2\pi f\lambda j}$$

If $H(f)$, the transfer function of the filter, can be made into a very narrow-band filter (which will necessitate $T \rightarrow \infty$ [29]), then W_V approaches the power spectrum, W_X , of the input voltage, $x(t)$. For example, if $|H(f)|^2$ approaches a delta function, $\delta(f \pm f_0)$, then $W_V \rightarrow W_X$.

An important interpretation of the filter is that of an operator on the input voltage, $x(t)$; that is, the action of the filter is $v(t) = P[x(t)]$ where $P = \int_{-\infty}^{\infty} d\lambda h(\lambda) \int \delta(t' - t + \lambda)$. The filter is not restricted to analog operation, but can be some form of digital (computer, for example) processing. The operation then becomes

$$v(t_i, h) = \sum_{k=1}^m h_k x(t_{i+k}) = P x(t)$$

where the $\Delta\lambda$ term has been absorbed into the set $\{h_k\}$.

The transfer function of the filter then becomes

$$H(f,h) = \sum_{k=1}^m h_k e^{-2\pi t_k f j}$$

The process of folding data is an example of digital processing. If the data is folded at some period Δt , then

$$Px(t_i) = \sum_{k=0}^m x(t_i + k\Delta t) = \int_{-\infty}^{\infty} df g(f) e^{j2\pi f t_i} \left(\sum_{k=0}^m e^{(j2\pi \Delta t f)k} \right)$$

The transfer function is seen to be

$$H(f) = \sum_{k=0}^m e^{(j2\pi \Delta t f)k}$$

It can be shown that

$$|H(f)| = \frac{\sin(m\pi \Delta t f)}{\sin(\pi \Delta t f)}$$

$|H(f)|$ is a highly peaked function at $f = \ell/\Delta t$ (ℓ an integer), which approaches a delta function as m approaches infinity.

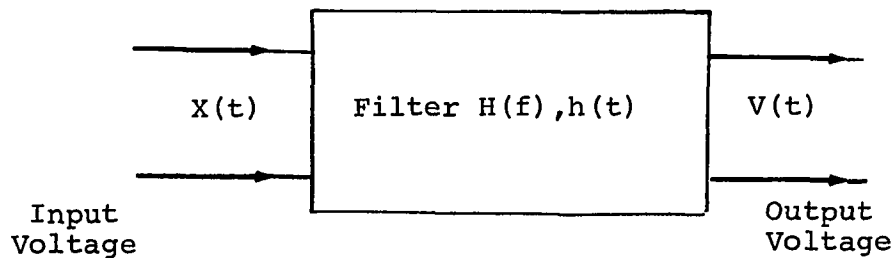


Figure 2

A Filter As A Two Port Device

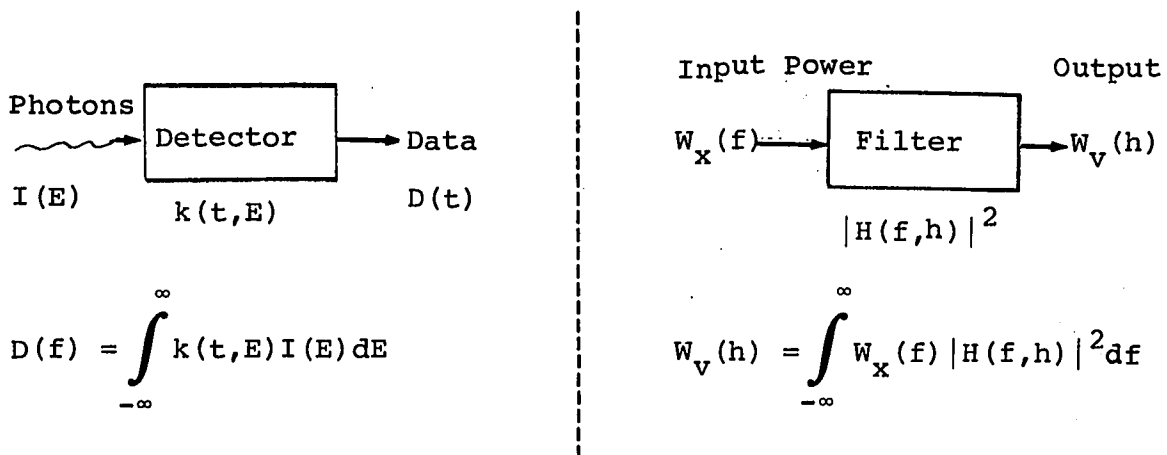


Figure 3

Power Spectrum/Unfolding Analogy

An analogy (Figure 3) can now be drawn between the results of this section and the unfolding problem of the photon detector (see Figure 3). The difference in the two cases is that the filter is forced into a form such that it has a narrow translatable bandpass, while the photon detector usually has a rather broad response in the energy domain. The implication is that some processing of the photon data analogous to forcing the filter into a bandpass form is a natural way in which to proceed in unfolding the data.

3. Kernel Modification

Making use of the insight provided by the last section it is now possible to proceed toward a solution to the unfolding problem. The word "solution" means the extraction of all the information about the spectrum consistent with the errors in the data. It is convenient to temporarily discard the error term in the Fredholm equation.

$$(7) \quad D(T) = \int_0^{\infty} k(T, E) \frac{dN}{dE} dE$$

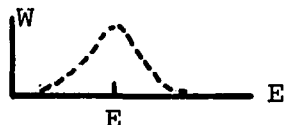
In the spirit of power spectrum analysis the data $D(T)$ will be processed by a linear operator $P(E)$, such that

$$P(E) D(T) = \int_0^{\infty} P(E) K(T, E') \frac{dN}{dE'} dE'$$

The function, $P(E)K(T, E')$ must be forced into the form of a function which exhibits the behavior of a sliding spectral window such that

$$P(E) D(T) = \int_0^{\infty} W(E-E') \frac{dN}{dE'} dE'$$

where $W(E-E')$ is of the form



Since the data will be discrete rather than continuous in any practical case, the operator can be represented as a weighted summation over all the data points. That is,

$$P(E) D(T) = \sum_{\ell=1}^N a_{\ell}(E) D(T_{\ell}).$$

Operating on both sides of equation (7) one obtains

$$P(E) D(T) = \sum_{\ell=1}^N a_{\ell}(E) D(T_{\ell}) = \int_0^{\infty} \sum_{\ell=1}^N a_{\ell}(E) K(T_{\ell}, E') \frac{dN}{dE'} dE'$$

The modified kernel is the function

$$K_{\text{mod}}^N(E, E') = \sum_{\ell=1}^N a_{\ell}(E) K(T_{\ell}, E')$$

If the set of functions $\{K(T_\ell, E)\}$ form a linearly independent set in the domain of E it should be possible to determine a set of coefficients $\{a_\ell\}$ such that a spectral window can be synthesized. The problem of what function to expand; and the problem of control of the values of the $\{a_\ell\}$ are of prime importance. Whenever a function, such as the spectral window, is expanded in a finite sum of linearly independent functions, side lobes appear. As the spectral window width desired decreases for a given number of expansion functions, the side lobes increase in amplitude. It is therefore desirable to choose a window function without discontinuities or infinitesimal width. A function similar to a gaussian would be desirable while a delta function would not. Examples of this phenomenon, which must certainly be related to the oscillatory problems reported in matrix formulation techniques, are given later in the chapter.

Inserting the error back into equation (7) and operating on both sides of the equation with the operator P results in the following expression from which the importance of controlling the set $\{a_\ell\}$ is inferred.

$$P(E) D(T) = \int_0^\infty \sum_{\ell=1}^N a_\ell K(T_\ell, E') \frac{dN}{dE'} dE' + \sum_{\ell=1}^N a_\ell E(T_\ell)$$

The total error in the spectral window output is

$$E_T = \sum_{\ell=1}^N a_\ell E(T_\ell) ,$$

which may become very large if the set $\{a_\ell\}$ is not controlled in amplitude. This problem is clearly related to the problem of an ill-conditioned (Section I) matrix in the matrix formulation.

The problem of operating on the data to achieve a spectral window is best summed up as follows: (1) A suitable spectral window function should be chosen; and (2) a set of coefficients $\{a_\ell\}$ such that the function

$$K_{\text{mod}}^N = \sum_{\ell=1}^N a_\ell K(T_\ell, E')$$

provides a reasonable fit to the spectral window function, must be found. It should be possible to determine the set $\{a_\ell\}$ that gives a least-squares fit to the spectral window function in several ways; for example, simple matrix inversion, use of a simplex type computer program [32], or if the set $\{K(T_\ell, E)\}$ form a well-known set, the coefficients are easily derivable (as in the next section). A least-squares fit subject to the constraint of a maximum value on the elements of the set $\{a_\ell\}$ is also possible through the use of a simplex type program. Further optimization of the modified kernel (reduction of side lobes) is possible through the use of non-linear optimization programs [33].

The important point to be made is that given the data, it is possible to synthesize the optimum spectral window consistent with the number of data points available and with the noise in the data.

4. Absorption Photon Detector

In the x-ray detector designed for 5-150⁰A x-rays, the kernel $K(t_\ell, E)$ is of the form

$$K(t_\ell, E) = e^{-\mu \rho t_\ell} \beta(\mu)$$

where μ is the mass absorption coefficient for aluminum, and β is the static response of the detector to an incident spectrum (static in that only the first part of the kernel, $e^{-\mu \rho t_\ell}$ changes with thickness t_ℓ).

It is judicious to switch from the variable E (energy) to the variable μ (mass absorption). The Fredholm equation then becomes (minus the error term),

$$D(t_\ell) = \int_0^{\infty} e^{-\mu \rho t_\ell} I(\mu) \beta(\mu) d\mu$$

where $I(\mu) = \frac{dN}{d\mu}(\mu)$

The only parameters to be determined now are the thickness ratios or thickness differences of the absorbers. If a solution which is possible in terms of well known orthogonal polynomials is desired, there appears to be two possible thickness ratios. The solution for logarithmic thickness variations are covered in Appendix C, and give rise to Laguerre polynomials. Equispaced thicknesses give rise to Legendre polynomials and will be covered in this section since this method is used in the experiment.

A word is in order about the choice of the spectral window function. The function

$$\left(\frac{ez}{a} e^{-z/a}\right)^P$$

seems to be an ideal choice in that it resembles a gaussian and peaks at $z=a$ with a maximum value of one. The variable z is defined as $z = \rho \mu t_0$ where t_0 is the initial value of thickness. By sampling at equispaced thicknesses the following Fredholm equation (minus error) is obtained:

$$(8) \quad D(Nt_0) = \int_0^{\infty} e^{-N\mu t_0 \rho} I(\mu) \beta(\mu) d\mu$$

where N is an integer. Operating on the data leads to the following equation

$$\sum_{N=1}^m a_N D(Nt_0) = \int_0^{\infty} \sum_{N=1}^m a_N \left(e^{-\rho \mu t_0}\right)^N I(\mu) \beta(\mu) d\mu$$

where the modified kernel is defined as

$$K_{\text{mod}}^m(\mu) = \sum_{N=1}^m a_N \left(e^{-\mu t_0 \rho}\right)^N$$

The functions, $\left(e^{-\mu t_0 \rho}\right)^N$, form a linearly independent set, and it is only a matter of finding the pertinent orthogonal polynomials to convert to for determination of the $\{a_N\}$. The interval in which the functions are defined is $(0,1)$, and the weighting function is 1; therefore, the appropriate polynomials are the odd Legendre polynomials with odd prolongation.

The odd Legendre polynomials are of the form

$$P_{2N+1}(x) = \sum_{\ell=0}^N x^{2\ell+1} \binom{2\ell+2N+2}{2N+1} \binom{2N+1}{N-\ell} \frac{(-1)^{N-\ell}}{2^{2N+1}}$$

or, gathering factors

$$(9) \quad P_{2N+1}(x) = \sum_{\ell=0}^N C_{\ell N} x^{2\ell+1}$$

An odd function $f(x)$ can be expanded in odd Legendre polynomials.

That is

$$f(x) \cong \sum_{N=0}^m A_N P_{2N+1}(x) dx$$

where

$$A_N = (4N+3) \int_0^1 f(x) P_{2N+1}(x) dx \quad (10a)$$

The synthesis of a spectral window can now be realized.

Using the transformation

$$x = e^{-z}, \quad dx = -e^{-z} dz$$

define the function

$$g(z) = f(e^{-z}).$$

Transforming (10a), it is seen that

$$A_N = (4N+3) \int_0^{\infty} g(z) e^{-z} P_{2N+1}(e^{-z}) dz$$

in an expansion of $g(z)$ of the form

$$g(z) \approx \sum_{N=0}^m A_N P_{2N+1}(e^{-z}).$$

Simplifying further by using equation (9)

$$(10b) \quad A_N = (4N+3) \sum_{\ell=0}^N C_{\ell N} \int_0^{\infty} g(z) e^{-z(2\ell+2)} dz$$

$$\text{and} \quad g(z) \approx \sum_{N=0}^m A_N \sum_{\ell=0}^N C_{\ell N} e^{-(2\ell+1)z}$$

or, interchanging sums

$$(11a) \quad g(z) \approx \sum_{\ell=0}^m \left(\sum_{N=\ell}^m A_N C_{\ell N} \right) e^{-(2\ell+1)z}$$

If $g(z)$ is the desired modified kernel, then

$$(11b) \quad K_{\text{mod}}^m = \sum_{\ell=0}^m a_{\ell} e^{-\mu \rho t_0 (2\ell+1)} \quad \text{where}$$

$$(11c) \quad a_{\ell} = \sum_{N=\ell}^m A_N C_{\ell N}$$

from the equation for $g(z)$ above.

The coefficient a_{ℓ} is the data weighting at $t_0, 3t_0, 5t_0, \text{ etc.}$, $\rho \mu t_0 = z$, and t_0 is some initial value of t .

There are two cases of interest; the delta function and the old favorite, $\left(\frac{ez}{a} e^{-z/a}\right)^P$. Before embarking on the calculations, a bit of foresight (hindsight in fact) will prove useful in controlling the spectrum of the a_{ℓ} 's. It turns out

that the a_ℓ 's for large M become prohibitively large. This growth is related to the "ill conditioned" matrix phenomena. An additional degree of freedom in determination of the coefficients a_ℓ is obtained by expanding the function, $g(z)$ as a function of $z-b$, where b is a parameter to be determined.

Case I: Delta Function

With $g(z) = \delta(z-b-z_0)$ it is seen, using (10b), that

$$A_N = (4N+3) \sum_{\ell=0}^N C_{\ell N} \int_0^\infty dz \delta(z-b-z_0) e^{-z(2\ell+2)},$$

which upon integration is

$$(4N+3) \sum_{\ell=0}^N C_{\ell N} e^{-b(2\ell+2)} e^{-z_0(2\ell+2)}.$$

Using equation (11)

$$g(z) = \delta(z-b-z_0) \cong \sum_{\ell=0}^m a_\ell e^{-(2\ell+1)z}$$

where

$$a_\ell = \sum_{N=\ell}^m A_N C_{\ell N}.$$

Letting $z \rightarrow z+b$, one obtains

$$\delta(z-z_0) \cong \sum_{\ell=0}^m a_\ell e^{-(2\ell+1)b} e^{-(2\ell+1)z}.$$

Using $a'_\ell = a_\ell e^{-(2\ell+1)b}$, the above reduces to

$$\delta(z-z_0) \cong K_{\text{mod}}^m = \sum_{\ell=0}^m a'_\ell e^{-(2\ell+1)z}$$

By manipulation of b , the set $\{a'_\ell\}$ can be controlled.

Case II: Old Favorite

With $g(z) = \left(\frac{e[z-b]}{z_0} e^{-\frac{[z-b]}{z_0}} \right)^P$ it is seen, using (10b),

$$\text{that } A_N = (4N+3) \left(\frac{e}{z_0} \right)^P \sum_{\ell=0}^N C_{\ell N} \int_0^\infty (z-b)^P e^{-\frac{(z-b)P}{z_0}} e^{-z(2\ell+2)} dz$$

Letting $z \rightarrow z+b$, one obtains

$$A_N = (4N+3) \left(\frac{e}{z_0} \right)^P \sum_{\ell=0}^N C_{\ell N} e^{-b(2\ell+1)} \int_0^\infty z^P e^{-z} \left(\frac{P}{z_0} + 2\ell+2 \right) dz$$

The integral can be found by making the substitution

$$y = z(P/z_0 + 2\ell + 2).$$

The integral becomes

$$\begin{aligned} \int_0^\infty z^P e^{-z(P/z_0 + 2\ell + 2)} dz &= (P/z_0 + 2\ell + 2)^{-(P+1)} \int_0^\infty y^P e^{-y} dy \\ &= (P/z_0 + 2\ell + 2)^{-(P+1)} \Gamma(P+1) \end{aligned}$$

See Appendix D for computation of the integral using Stirling's approximation for $\Gamma(N)$. Again, as in the case of the delta function calculations, with

$$a_\ell = \sum_{N=\ell}^m A_N C_{\ell N},$$

one lets $z \rightarrow z+b$ with the result that

$$g(z+b) = \left(\frac{ez}{z_0}\right)^P e^{-z/z_0} (P) .$$

The modified kernel is seen to be

$$K_{\text{mod}}^m = \left(\frac{ez}{z_0}\right)^P e^{-z/z_0} (P) \cong \sum_{\ell=0}^m a'_\ell e^{-(2\ell+1)z}$$

with $a'_\ell = a_\ell e^{-(2\ell+1)b}$.

It is illuminating at this point to compare the windows, $\delta(z-z_0)$, and $\left(\frac{ez}{z_0} e^{-z/z_0}\right)^P$. Figure 4 is a graph of both kernels in z space ($m = 15$ in both cases). Although the delta function has a sharper main lobe, the function $\left(\frac{ez}{z_0} e^{-z/z_0}\right)^P$ has much smaller side lobes.

5. Implementation of the Kernel Modification

The use of either of the windows $\left(\frac{ez}{z_0} e^{-z/z_0}\right)^P$ or $\delta(z-z_0)$ begins with experimental curves of data (count rate) vs. thickness of absorber. The data will be monotonically decreasing for any spectrum, as seen in Figure 5.

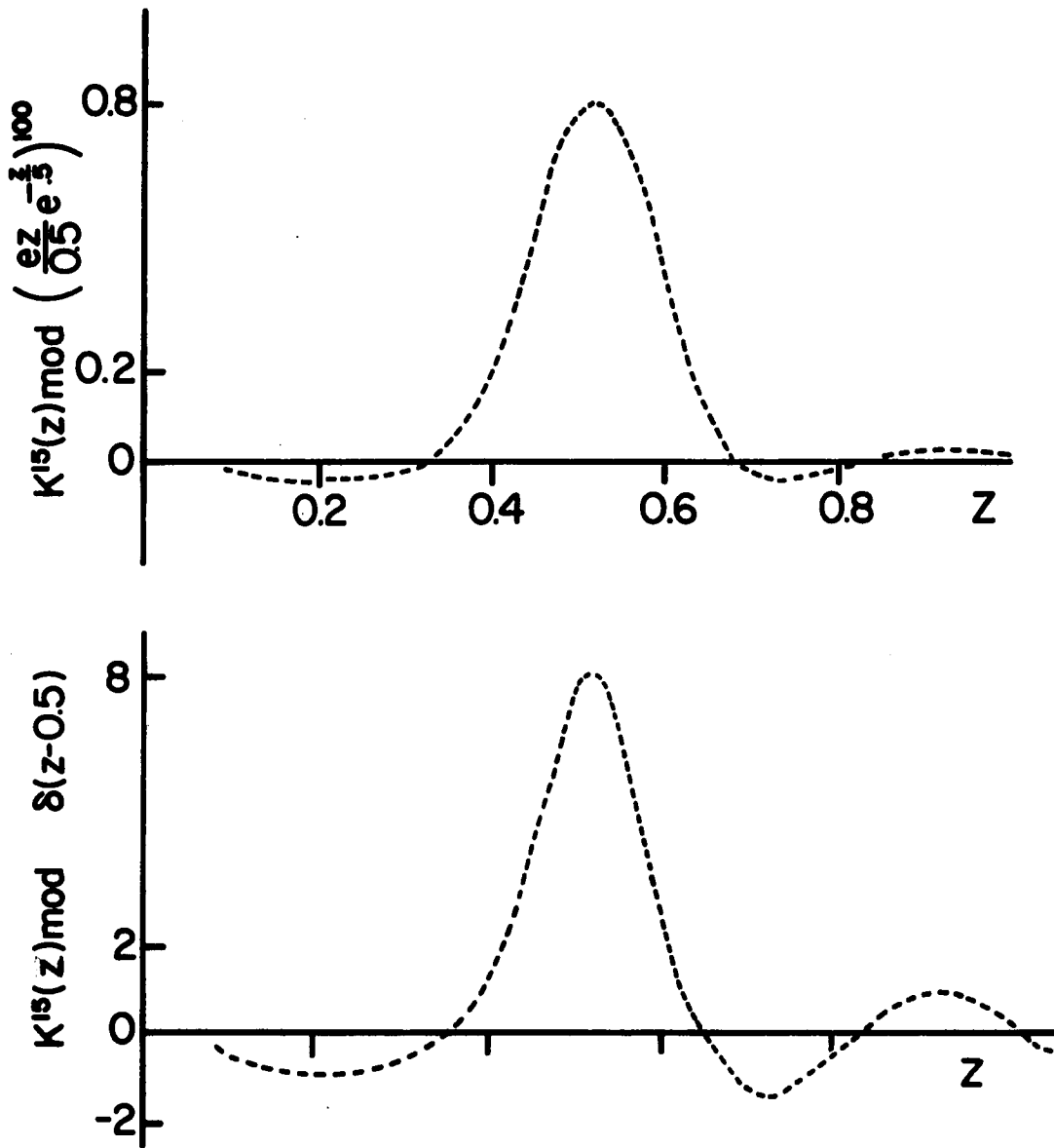


FIG. 4--COMPARISON OF LEGENDRE WINDOWS

$D(T)$, count rate
(arbitrary units)

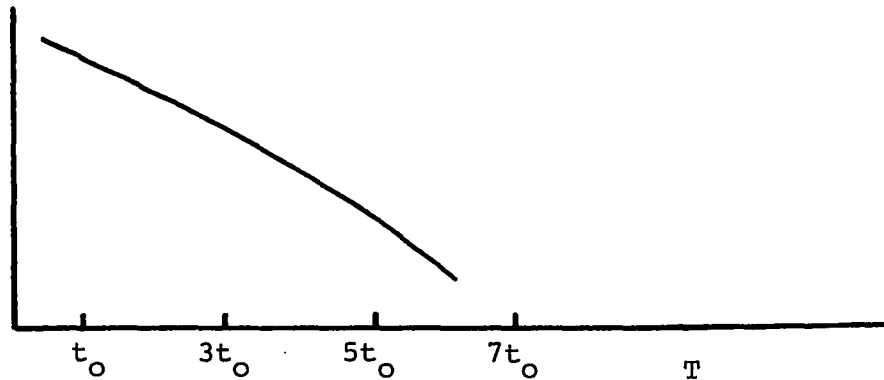


FIGURE 5

TYPICAL PHOTON ABSORBER DETECTOR DATA

In the Legendre method, the operation on the data is

$$P D(t) = \sum_{\ell=0}^m a_{\ell}(\mu) D([2\ell+1]t_0)$$

with modified kernel

$$K_{\text{mod}}^m = \sum_{\ell=0}^m a_{\ell}(\mu t_0 \rho) e^{-(2\ell+1)\mu t_0 \rho}$$

The practical limits over which the windows can be centered in μ space are determined by the range of the set of data points. As an instructive example, take a two component spectrum, $I(\mu) = \delta(\mu - \mu_1) + \delta(\mu_2 - \mu)$. Then using equation (8)

$$D(t) = e^{-\mu_1 t} + e^{-\mu_2 t}$$

where $\mu = z/t$, leads to the expression

$$D(t) = e^{-z_1 t/t_0} + e^{-z_2 t/t_0}.$$

Integerizing it leads to the expression

$$D(Nt_0) = e^{-z_1(2\ell+1)} + e^{-z_2(2\ell+1)} \quad N = 2\ell+1$$

Let $z_1 = 0.4$, $z_2 = 0.6$, $m = 15$

$$\text{then } W_0(z_0) = \sum_{\ell=0}^m a_{\ell}(z_0) \left(e^{-z_1(2\ell+1)} + e^{-z_2(2\ell+1)} \right)$$

where $W_0(z_0)$, the window output, is the result of sliding a spectral window,

$$K_{\text{mod}}^{15} = \sum_{\ell=0}^{15} a_{\ell}(z_0) e^{-(2\ell+1)z},$$

centered about z_0 from $z_0 = 0$ to 10. The $a_{\ell}(z_0)$'s are computed, using the results of the last section, by LEG2, a computer program described in Appendix G. This $W_0(z_0)$ is shown in Figure 6 with $m=15$, $K_{\text{mod}}^{15} \cong \delta(z-z_0)$. Note that the two delta functions are resolved. In the soft x-ray range

$$\mu = \rho/c E^{-2.8}$$

$$\frac{E_2}{E_1} = \left(\frac{z_1}{z_2} \right)^{.36} = (.67)^{.36} = 1.15$$

This corresponds to a resolution of

$$100 \frac{(E_2 - E_1)}{\sqrt{E_1 E_2}} = 14\%$$

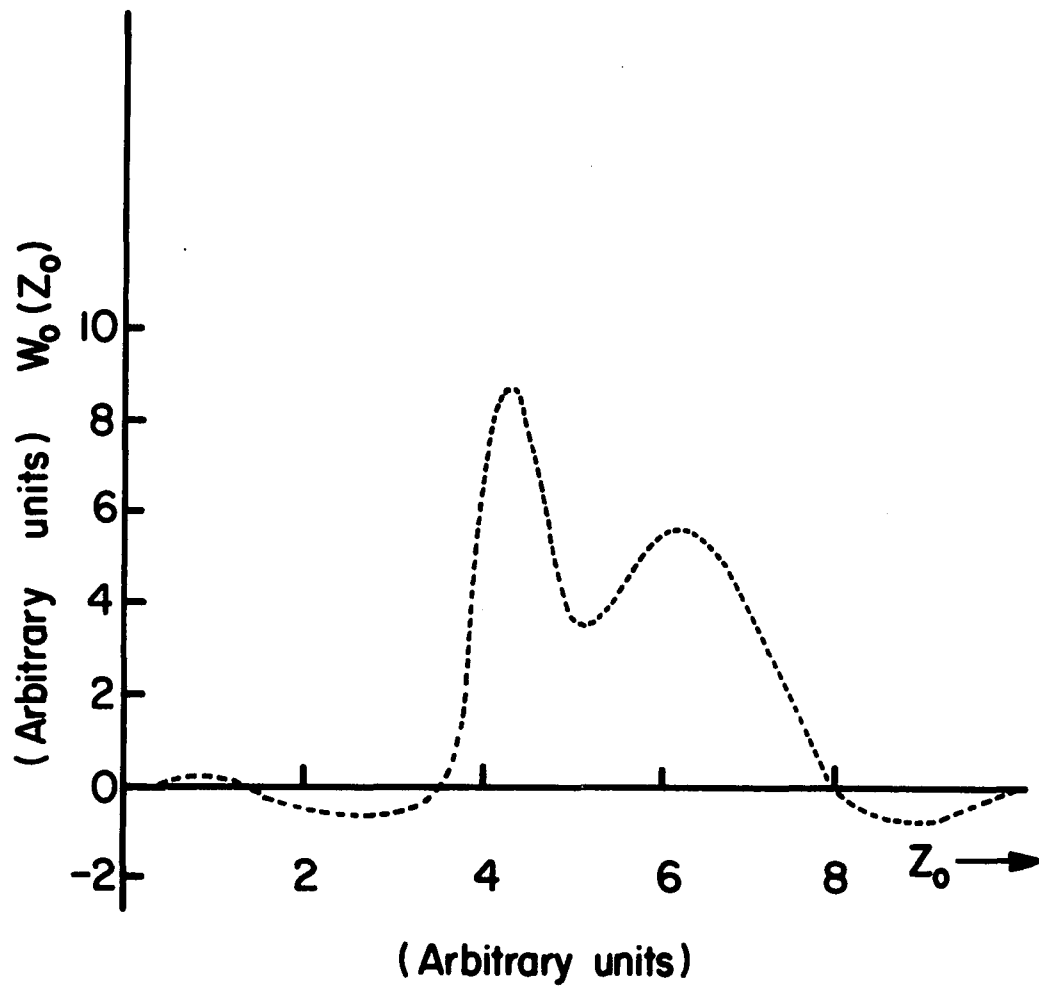


FIG. 6--LEGENRE SOLUTION OF A TWO COMPONENT SPECTRUM

The difference in peak height is due to the change in window shape as a function of z , and/or the existence of side lobes.

The question of practical spectral resolution attainable is of fundamental importance. The practical Fredholm equation is

$$(12) \quad D(t) = \int_0^{\infty} k(t, E) I(E) dE + E(t)$$

where $E(t)$ is the error in the data, $D(t)$. The spectral window output is

$$W_0(\mu_0) = \sum_{\ell=0}^m a_{\ell}(\mu_0) D(Nt_0),$$

which upon use of equation (12) becomes

$$W_0(\mu_0) = \int_0^{\infty} \sum_{\ell=0}^m a_{\ell} K(Nt_0, E) I(E) dE + \sum_{\ell=0}^m a_{\ell} E(Nt_0)$$

with $N = 2\ell + 1$.

Let $E(t) = D(t) \beta(t)$ where $\beta(t)$ is the fractional error in $D(t)$.

The error in $W_0(\mu_0)$ is then

$$\sum_{\ell=0}^m a_{\ell}(\mu_0) D(Nt_0) \beta_N.$$

A sum of squares type of error is represented by

$$(13) \quad E = \sqrt{\sum_{\ell=0}^m a_{\ell}^2(\mu_0) D^2(Nt_0) \beta_N^2}.$$

For a spectral line of strength P , the

$$\frac{\text{Spectrum Window Signal}}{\text{Noise}} = \left(\frac{S}{N}\right) = \frac{P}{E} .$$

If β is not a function of N , solving equation (13) for β gives

$$(14) \quad \beta \left(\frac{S}{N}\right) = \frac{P}{\sqrt{\sum_{\ell=0}^m a_{\ell}^2 D^2(Nt_0)}} .$$

Letting $D(Nt_0) = \frac{P}{E}$ and using equation (14) it is seen that

$$\beta = \frac{E}{\left(\frac{S}{N}\right)} \sqrt{\frac{1}{\sum_{\ell=0}^m a_{\ell}^2(\mu_0)}} .$$

Let β be the fractional error allowed in the data for a desired S/N in the spectral window output for a line source. The graph of Figure 7 gives a reasonable estimate of the accuracy required in the data ($S/N = 6$) for a desired spectral resolution. The graph was derived using $z_0 = .5$ and the $\delta(z-z_0)$ window, ($z_0 = \mu_0 t_{0\rho}$). Setting $z_0 = .5$ gives a good average value for β since β is a weak function of z_0 . No attempt was made to control the spectrum of the set $\{a_{\ell}\}$ (i.e., $b=0$). The graph on Figure 8 indicates the number of absorbers required for a given resolution. It is apparent that as the number of absorbers increases, the error allowed in the data for a reasonable result decreases rapidly. This phenomena is related to the ill condition matrix case in the matrix formulation unfolding.

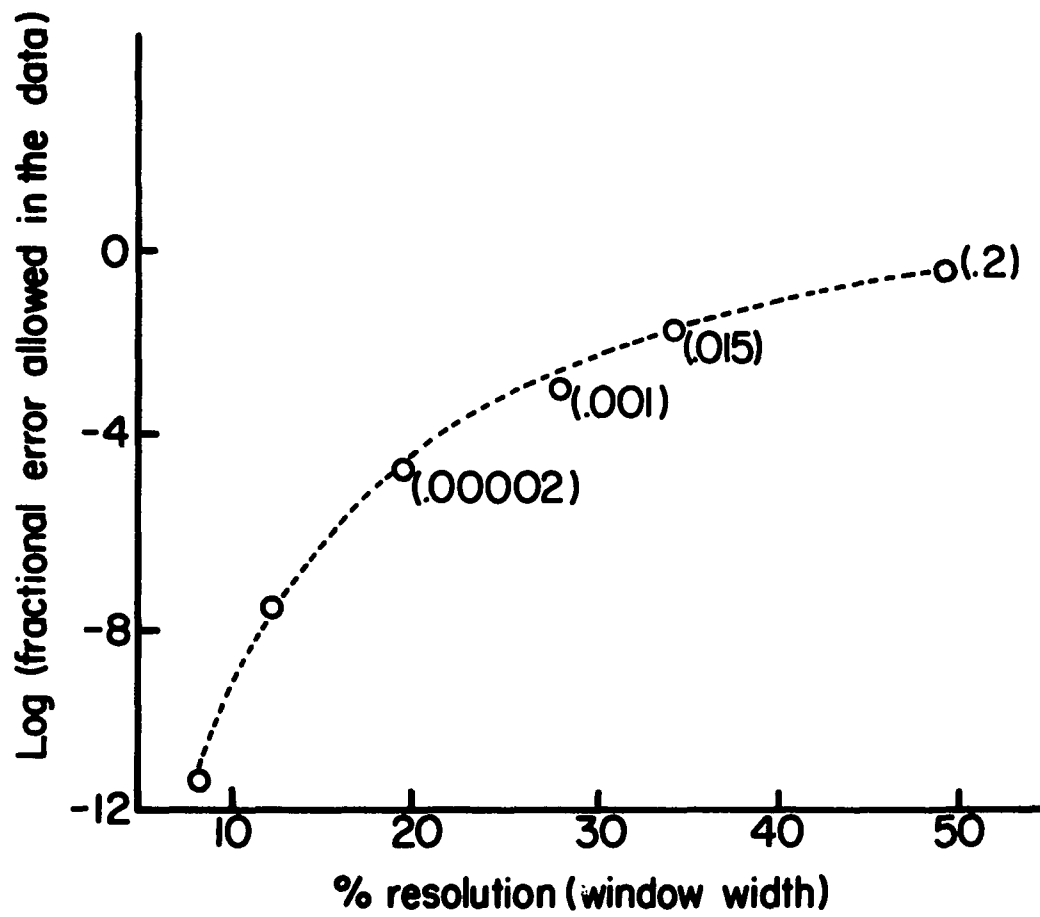


FIG. 7--FRACTIONAL ERROR ALLOWED IN THE DATA FOR A REQUIRED RESOLUTION

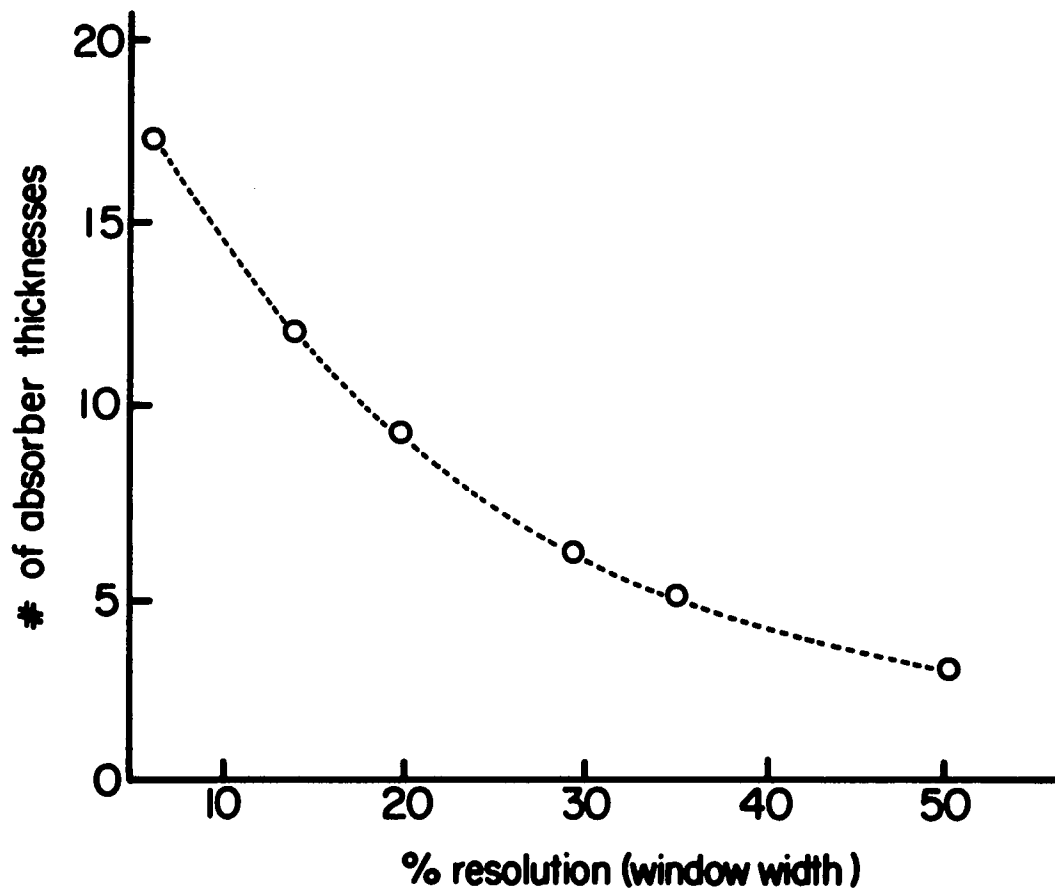


FIG. 8--# OF ABSORBERS Vs % RESOLUTION POSSIBLE

An experimental example of the use of this technique is the decomposition of a two component spectrum. A Co^{57} (14 kev) source and a Fe^{55} (6.7 kev) source were combined in the laboratory to yield 7 kev and 14 kev lines. The high energy line in Co^{57} was eliminated by pulse height discrimination. Sheets of aluminum foil served as the absorber while a scintillation counter served as the x-ray detector. Five thicknesses of aluminum were used in obtaining data. The data obtained is shown in Figure 9. A spectral window which swept continuously through the 7-14 kev x-ray band was synthesized in the following way:

Comment: At this point it will do to remember the static detector response, $\beta(E)$, where

$$D(t) = \int_0^{\infty} e^{-\mu\rho t} \beta(E) \frac{dN}{dE} dE$$

Any synthesized sliding spectral window must be modulated by $\beta(E)$ over the spectral range of interest. If $\beta(E)$ is a smooth function no calculational problems arise. If there are discontinuous points in $\beta(E)$, care must be taken in the computations near such discontinuities. In the case of the Co^{57} - Fe^{55} experiment, $\beta(E)$ is the response of the scintillation counter.

With $p = 30$, the window,

$$\left(\frac{e\mu(E)}{\mu_0} e^{-\frac{\mu(E)}{\mu_0}} \right)^{30} ,$$

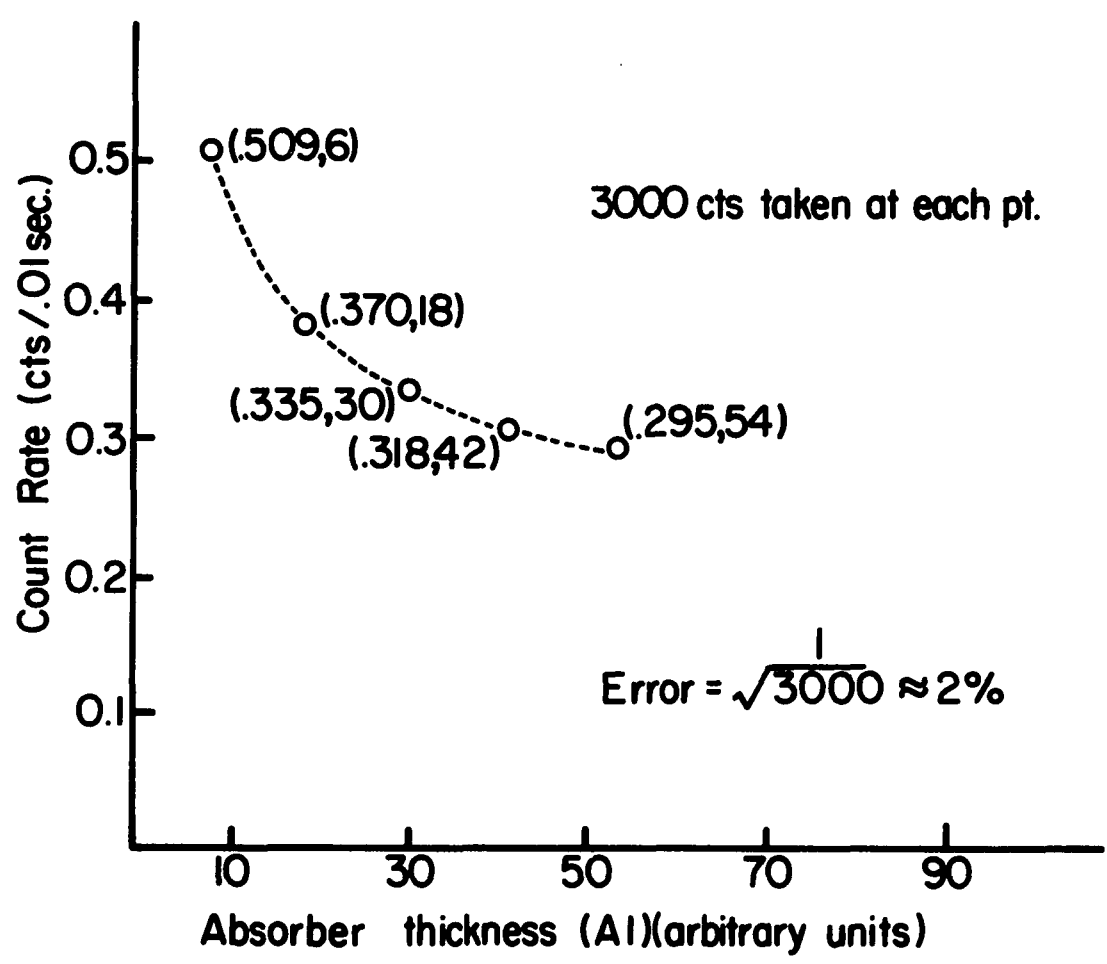


FIG. 9--RAW DATA FROM Fe⁵⁵-Co⁵⁷ SOURCES

was synthesized by determining the coefficients a_ℓ , where the function

$$K_{\text{mod}}^4 = \sum_{\ell=0}^4 a_\ell(\mu_0) \left[e^{-\mu \rho t_0} \right]^{2\ell+1}$$

represents a spectral window centered on μ_0 . The operation on the data $D(t)$ is

$$P D(t) = W_0(\mu_0) = \sum_{\ell=0}^4 a_\ell(\mu_0) D[(2\ell+1)t_0]$$

where $D[(2\ell+1)t_0]$ is the data from the ℓ^{th} thickness of absorber, and $W_0(\mu_0)$ represents the window output centered at μ_0 . ' μ_0 ' was varied in small steps from the μ which corresponds to 5.5 keV to the μ which corresponds to 18 keV. In this region $\mu \propto E^{-2.8}$ (from any absorption coefficient tables such as Henke [34]). It is then possible to calibrate in terms of E (energy) instead of μ . Since only five terms (thicknesses) were used, the spectral window is really only an approximation to the function $\left(\frac{e\mu}{\mu_0} e^{-\mu/\mu_0}\right)^{30}$. The unfolding of this two line source into component spectral parts for this sliding window is shown in Figure 10. The sliding window calculations were done by LEG2, a computer program described in Appendix G.

NOTE: The count rates as shown in Figure 10, obtained through the theoretical analysis, was almost identical to the absolute count rate in the laboratory (each source separately).

The photon detector proposed was to work in the range 5-150 Angstroms (details of the detector are in Chapter IV).

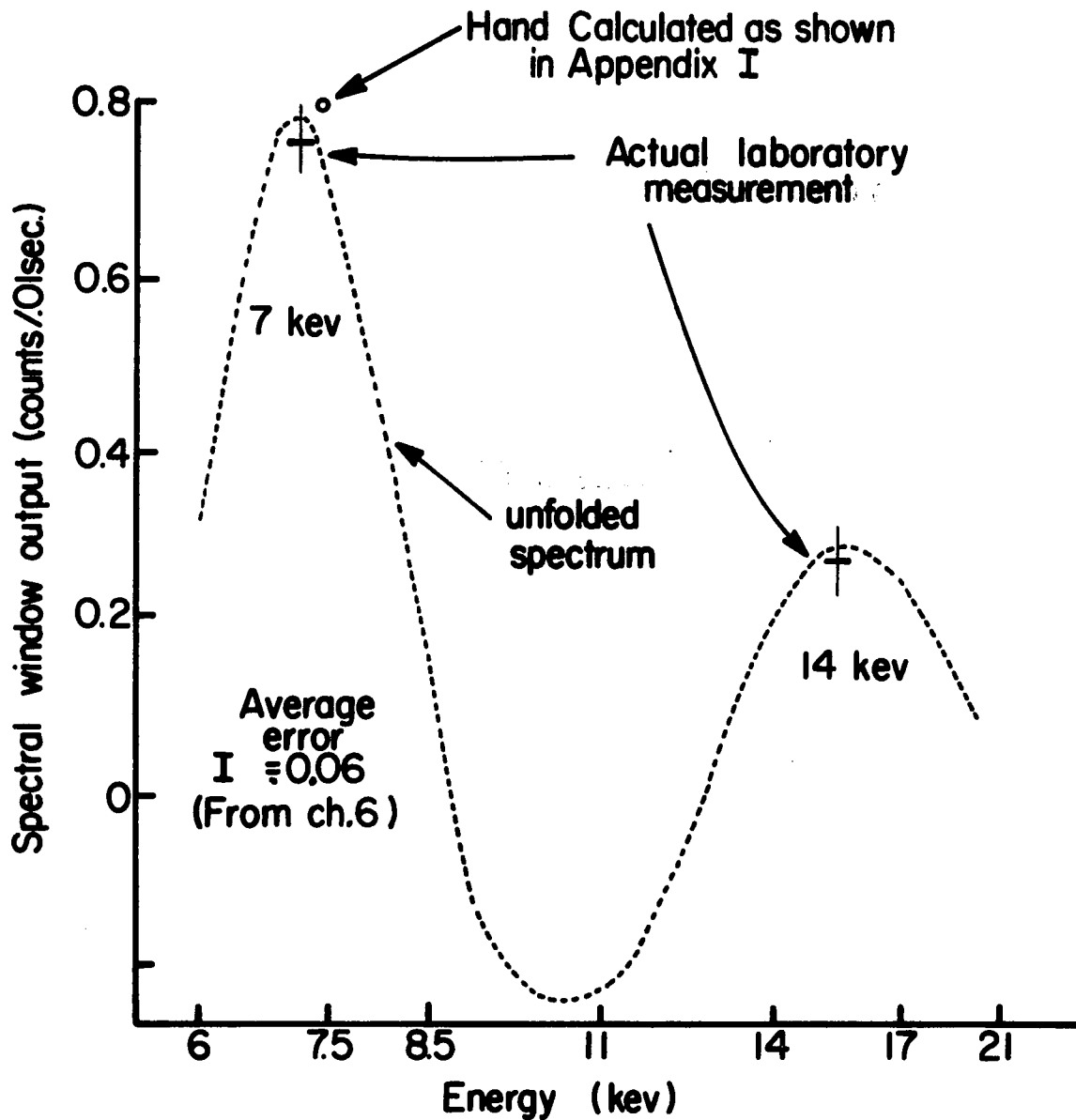


FIG. 10--DECOMPOSITION OF Fe⁵⁵-Co⁵⁷ SOURCE

Aluminum was chosen as the absorbing element in the photon detector, which was to have four different thicknesses of absorber. Given that the four thicknesses of aluminum are 500, 1500, 2500, and 3500 $\overset{\circ}{\text{A}}$, and using the program LEG1, which synthesizes and displays window responses, the following spectral windows were constructed as examples of a sliding spectral window. The coefficients used to weigh the data to form each spectral window

$$K_{\text{mod}}^3 = \sum_{\ell=0}^3 a_{\ell}(\mu_{\overset{\circ}{0}}) \left(e^{-\rho t_{\overset{\circ}{0}} \mu} \right)^{2\ell+1}$$

where $t_{\overset{\circ}{0}} = 500\overset{\circ}{\text{A}}$

are listed in the graphs, (Figures 11 thru 14).

The conversion from the mass absorption coefficient to the wavelength was accomplished using the curve in Figure 15. Note the discontinuity at 104 $\overset{\circ}{\text{A}}$ in the spectral windows. If such discontinuities become large the usefulness of the absorber used in the kernel modification is of questionable value, especially if strong line sources happen to be located at the discontinuity.

$$a_0 = -0.5499$$

$$a_1 = 4.166$$

$$a_2 = -4.267$$

$$a_3 = 3.665$$

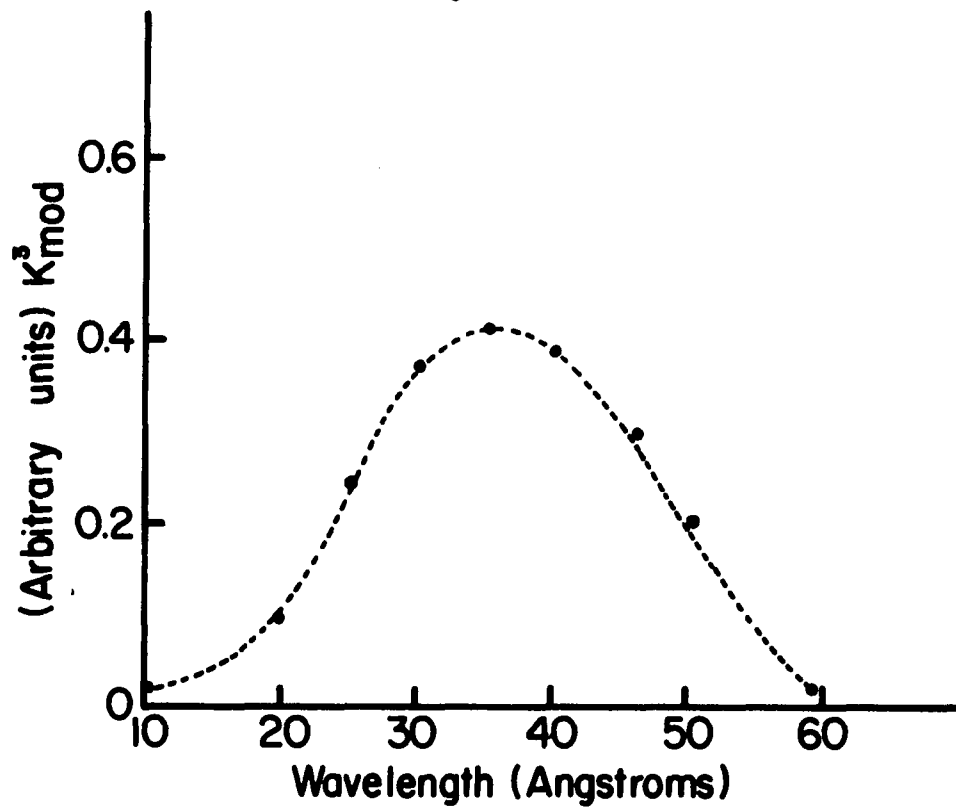


FIG. 11--34A WINDOW

$$\begin{aligned}a_0 &= -1.02 \\a_1 &= 13.45 \\a_2 &= -28.6 \\a_3 &= 16.5\end{aligned}$$

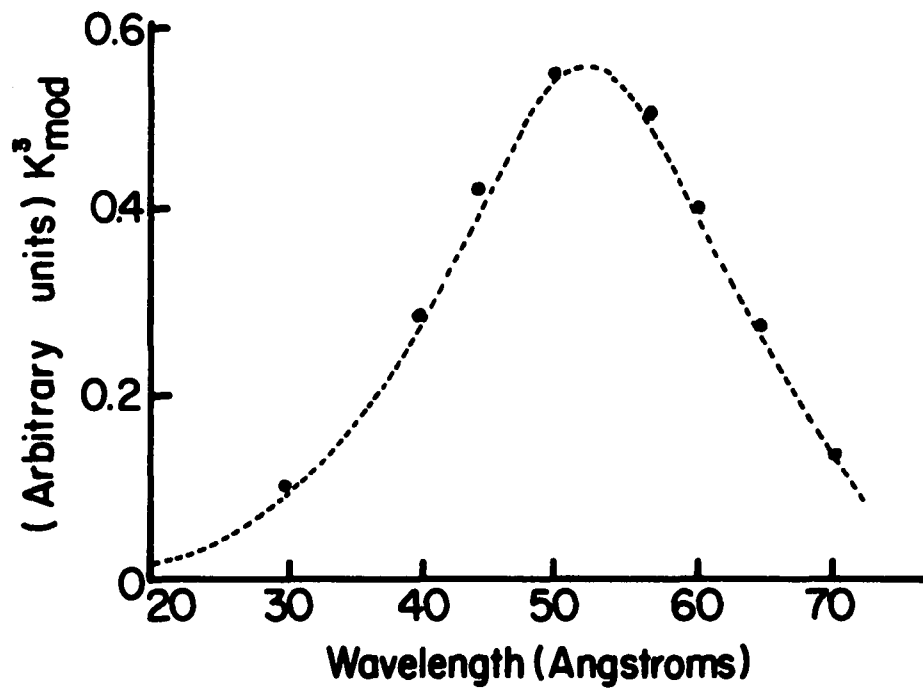


FIG. 12--50A WINDOW

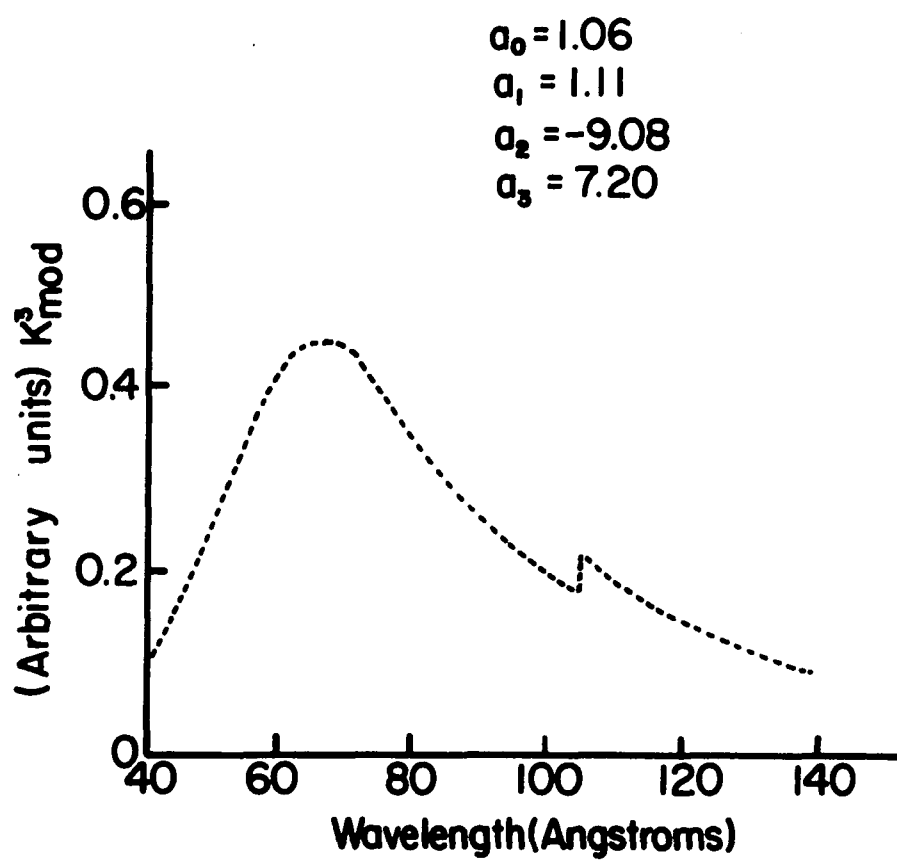


FIG. 13--70^oA WINDOW

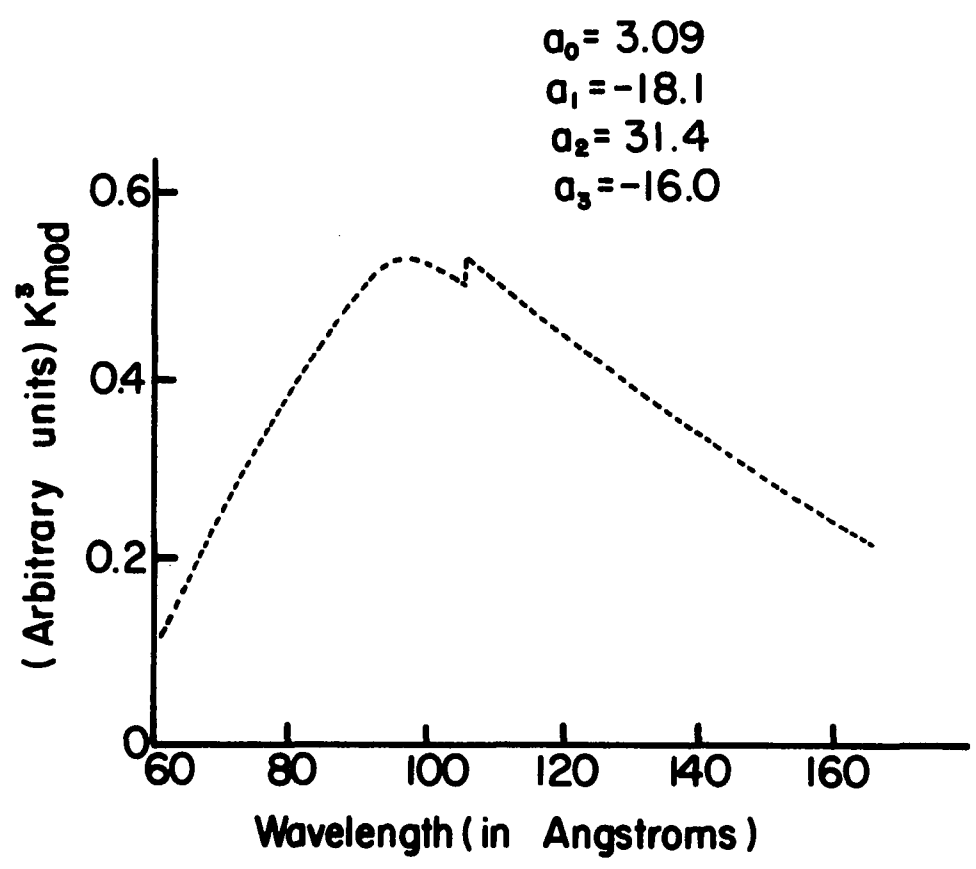


FIG. 14--100^oA WINDOW

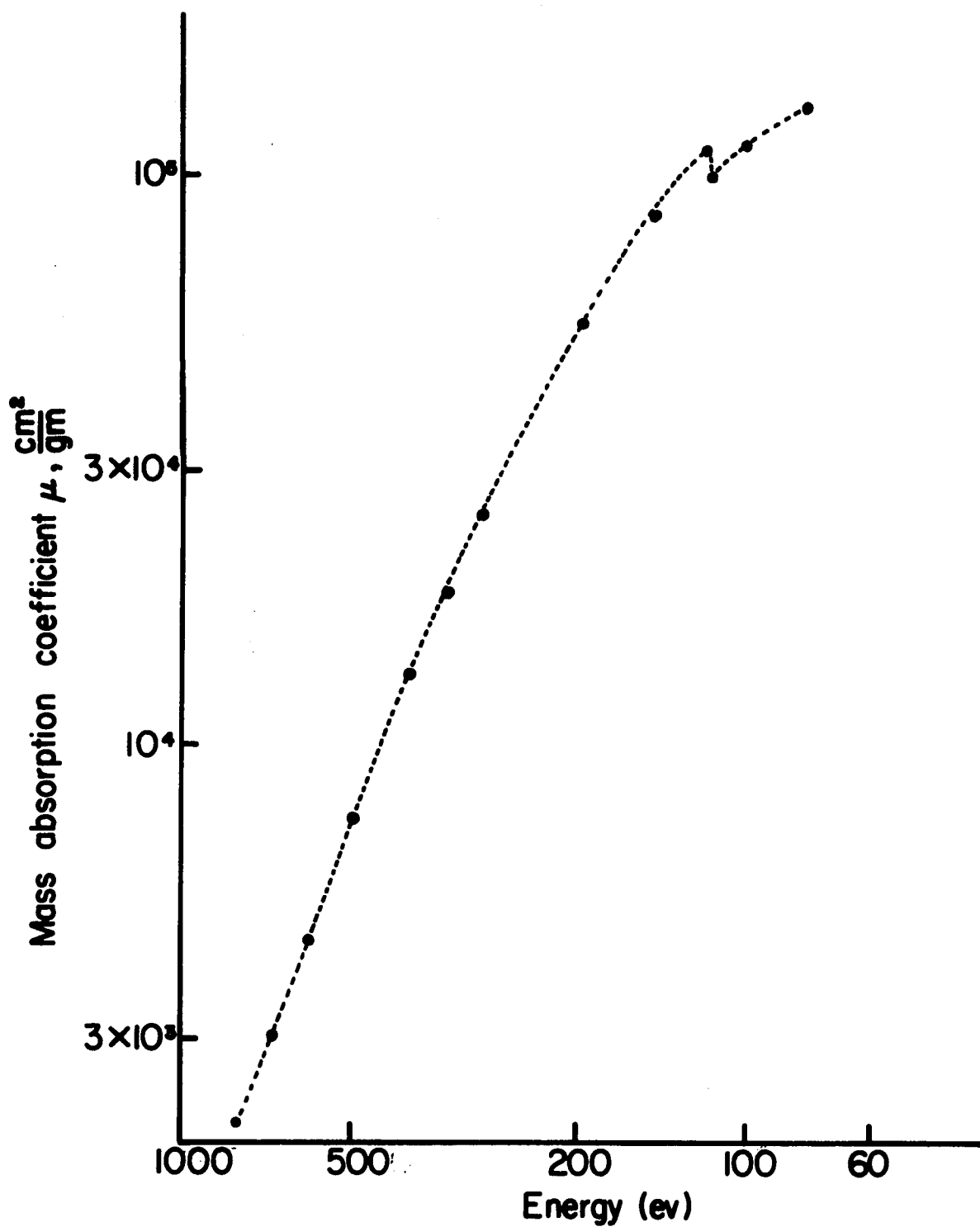


FIG.15--ABSORPTION COEFFICIENT OF ALUMINUM
(FROM HENKE [34])

CHAPTER III

PHOTON DETECTION TECHNIQUES

1. Photoemission

Photoemission in the ultra-soft x-ray (10-400^oA) range is a volume effect rather than the usual surface effect associated with optical photons. The photoelectrons are generated in a region ranging from the surface of the photocathode to some point inside the photocathode, dependent upon the material and the photon energy. The photoelectric yield is usually defined as the number of external electron emission producing photons divided by the number of incident photons. Another frequently used definition of photoelectric yield is the number of electron emission producing photons divided by the number of incident photons absorbed. The latter definition takes reflection of incident photons into account. Optimal design of a detector depends critically upon the geometry for two reasons: (1) necessity of collecting photoelectrons and secondary electrons, and (2) the dependence of the photoelectric yield on the angle of incidence between the radiation and the photocathode surface. A phenomenological theory of photoelectric yield in this spectral region has been developed over the past few years [35-43]. This phenomenological theory assumes that the Fresnel theory for homogeneous media holds for "granular" matter, as exists in the x-ray case. The

photocathode geometry is illustrated by Figure 16. The Fresnel reflection coefficients are expressed as follows:

$$R_{\parallel} = \left| \frac{\frac{1}{\sin\theta} - \frac{1}{N \sin\theta'}}{\frac{1}{\sin\theta} + \frac{1}{N \sin\theta'}} \right|^2$$

$$R_{\perp} = \left| \frac{\sin\theta - \frac{\sin\theta'}{N}}{\sin\theta + \frac{\sin\theta'}{N}} \right|^2$$

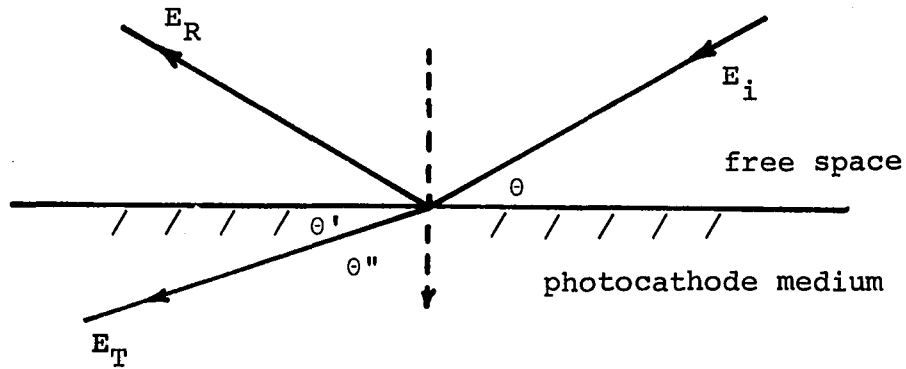
where \parallel and \perp refer to radiation polarized parallel or perpendicular to the plane of incidence, and N is the index of refraction of the photocathode medium. For unpolarized radiation the relationship

$$R = \frac{1}{2} (R_{\parallel} + R_{\perp}) \text{ holds.}$$

A total internal reflection effect has been observed, the implication of which is that the real part of the index of refraction is less than one. It is, therefore, judicious to represent the index of refraction by the following function.

$$N = 1 - \delta - i\beta$$

where β and δ are positive, real numbers. The transmission of energy across a particular surface, parallel to the photocathode surface is the ratio of the Poynting vector normal to that particular surface, and the incident Poynting vector normal to the photocathode surface. The transmission,



E_i, E_R refers to the incident and reflected fields
 E_T refers to the transmitted field

FIGURE 16

PHOTOCATHODE GEOMETRY

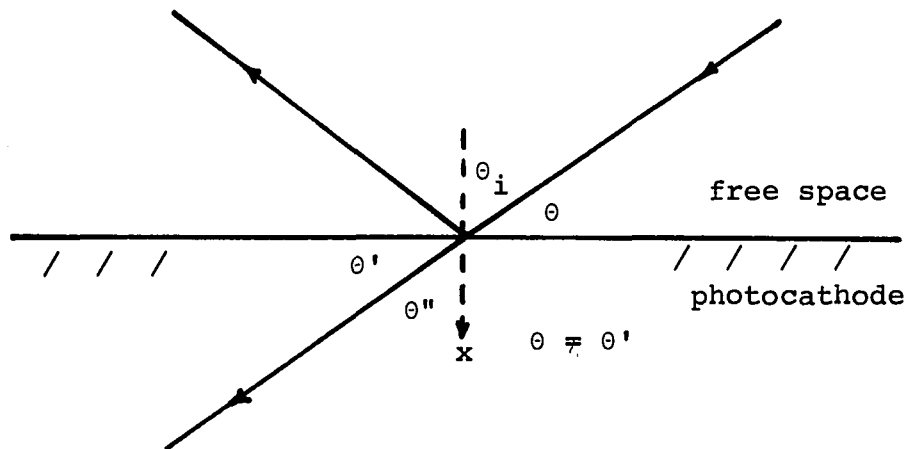


FIGURE 17

PHOTOCATHODE GEOMETRY FOR LARGE GRAZING ANGLES
AND/OR HIGH ENERGIES

$$T = \frac{S_T \text{ (Normal)}}{S_i \text{ (Normal)}} ,$$

and as shown in Appendix A

$$T = (1-R) \left| e^{ik \cdot r} \right|^2$$

$$T = (1-R) e^{-2k_0 x \text{ Im } (N \cos \theta'')} ,$$

where $k_0 = 2\pi/\lambda_0$

The above expression implies an effective thickness exists; that is,

$$t_{\text{eff}} = 2k_0 \text{ Im } (N \cos \theta'')$$

such that $T = (1-R) e^{-x/t_{\text{eff}}}$.

For large grazing angles of incidence and/or high energy x-rays (Figure 17), it is legitimate to set $\theta = \theta'$. For this case, it is shown in Appendix A that the following relation exists;

$$\left| e^{ik \cdot r} \right|^2 = e^{-\frac{2\beta k_0 x}{\sin \theta'}} = e^{-\frac{\mu x}{\sin \theta'}}$$

where μ is the x-ray absorption coefficient for the material.

The effective thickness is given as

$$t_{\text{eff}} = \frac{\sin \theta'}{\mu} .$$

In this special case, the photoelectric yield as a function of angle of incidence is physically intuitive for the following reason (referring to Figure 17). The efficiency (electron emission photons/incident number of photons) should increase as θ decreases since the photons are being absorbed closer to the surface, and the photoelectrons find it easier to be emitted. As the reflectivity approaches one, the transmission and the efficiency approach zero, hence the efficiency must reach a maximum at some angle θ .

Referring to Figure 16; at the critical angle of incidence the following relation must exist as a consequence of Snell's Law;

$$\sin\theta' = 0 = \sqrt{1 - \frac{\cos^2\theta_{cr}}{N^2}}$$

solving for $\cos\theta_{cr}$,

$$\cos\theta_{cr} = \text{Re } N = 1 - \delta$$

For small

$$\theta_{cr}, \cos\theta_{cr} \rightarrow \frac{2 - \theta_{cr}^2}{2},$$

which implies $\theta_{cr} = \sqrt{2\delta}$.

For small θ_{cr}' , according to Parrat [44],

$$\text{Im } (N \cos\theta'') = \frac{1}{\sqrt{2}} \sqrt{(\theta''^2 - \theta_{cr}^2)^2 + 4\beta^2} - \frac{1}{\sqrt{2}} \sqrt{\theta''^2 - \theta_{cr}^2}$$

Perfect reflection beyond the critical angle is impossible because of the absorption in the photocathode (unlike the total internal reflection of dielectrics). Lukirskii [40] has obtained an expression for the efficiency of a photocathode. When the transmission is expressed as

$$T_p = (1-R) e^{-\frac{x}{t_{\text{eff}}}}$$

then

$$dT_p = (1-R) \frac{-1}{t_{\text{eff}}} e^{-\frac{x}{t_{\text{eff}}}} dx$$

where $|dT_p|$ is the probability that the photon is absorbed in a layer dx at depth x . The efficiency (electron emission photons/incident photons) for a thick photocathode is

$$E = \int_0^{\infty} W(x) dT_p$$

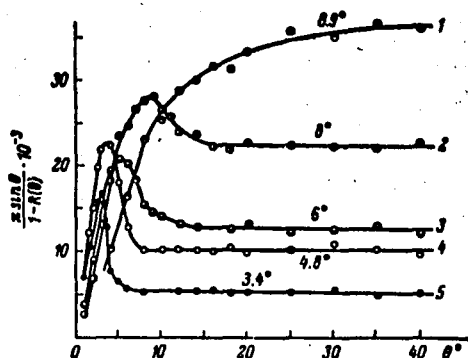
where $W(x)$ is the probability that at least one electron will be emitted when a photon is absorbed in a layer dx at depth x . Substituting for dT_p in the above expression,

$$E = \int_0^{\infty} dx \frac{1-R(\theta)}{t_{\text{eff}}} W(x) e^{-\frac{x}{t_{\text{eff}}}}$$

If $W(x)$ is assumed to be a simple exponential, $e^{-\alpha x}$, then the integration can be carried out with the result [35].

$$E = \frac{1-R(\theta)}{t_{\text{eff}}(\theta)} \frac{1}{(1/t_{\text{eff}} + \alpha)}$$

Experimental curves (Figure 18) for the efficiency of a photocathode have been obtained by Lukirskii [40].



Values of $\frac{\pi \sin \theta}{1-R(\theta)} \cdot 10^{-3}$ as a function of the angle of incidence θ for an aluminum photocathode at different wavelengths. (1) Beryllium line (113 Å); (2) boron line (67 Å); (3) carbon line (44 Å); (4) nitrogen line (31.4 Å); (5) oxygen line (23.6 Å). Written on the curves are the critical angles of incidence for the corresponding wavelength: 3.4° - for $O_{K\alpha}$, 4.8° - for $N_{K\alpha}$, 6° - for $C_{K\alpha}$, 8° - for $B_{K\alpha}$, and 8.9° - for $Bc_{K\alpha}$.

FIGURE 18

AL PHOTOCATHODE EFFICIENCY (Lukirskii [40])

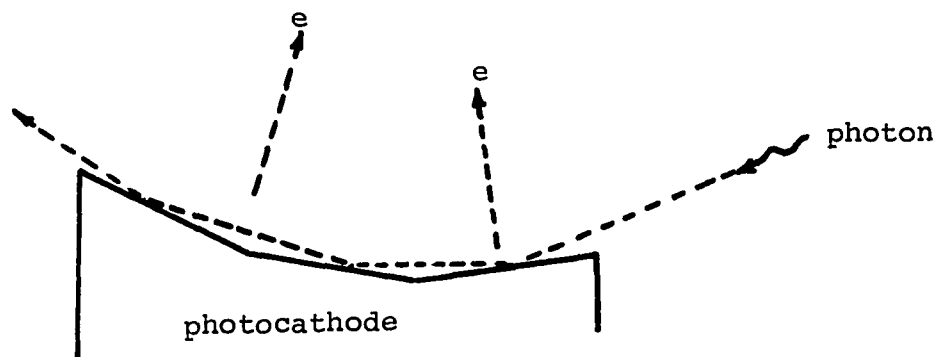


FIGURE 19

MULTIPLE REFLECTION-ABSORPTION PHOTOCATHODE

In the Lukirskii result $R(\theta)$ and $E \sin\theta$ were experimentally determined. Lukirskii [41] has also experimentally determined the reflection coefficients for many materials in this range of the spectrum as a function of grazing angle of incidence. Strong maxima are present in the region of the critical angles. If one examines the modified efficiency, E' (electron emission photons/absorbed photons)

$$\left(E' = \frac{E}{1-R(\theta)} = \frac{1}{1 + \frac{1}{\alpha} t_{eFF}} \right),$$

then it is apparent that since

$$\lim_{\theta \rightarrow 0} t_{eFF} = 0 \quad \text{then} \quad \lim_{\theta \rightarrow 0} E' = 1$$

The implication of the limiting value of 1, is that by using a multiple reflection-absorption photocathode configuration (Figure 19), the efficiency (electron emission photons/incident photons) can approach 100%.

For large grazing angles ($\theta > 20^\circ$) the photocathode efficiency experimentally follows a cosec(θ) law. Using Lukirskii's expression for efficiency,

$$E = \frac{1-R(\theta)}{t_{eFF}} \left(\frac{1}{\frac{1}{t_{eFF}} + \alpha} \right) \quad t_{eFF} = \sin\theta/\mu$$

$$R(\theta) \approx 0$$

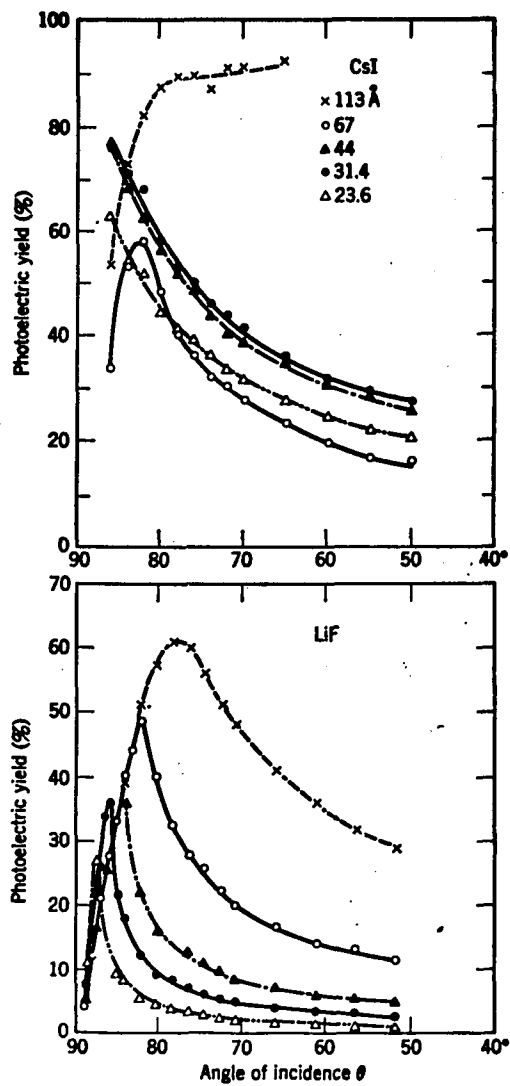
$$E = \frac{1}{1 + \sin\theta \frac{\alpha}{\mu}} \approx \frac{1}{\frac{\alpha}{\mu} \sin\theta} \quad \text{For AL}$$

$$\alpha \sim 10^6, \mu \sim 10^4$$

The cosecant law for large angles and the effect of the reflection coefficient are beautifully illustrated in Lukirskii's [37] experimental graphs, reproduced in Figure 20.

Of all the materials available for photocathodes, the most efficient in the ultra-soft x-ray range are the alkali-halides; CsI, LiF, and MgF_2 in that order. The efficiency of these materials is shown in Figures 20 and 21. The data in Figure 22 was obtained by the author in August 1971 at the Naval Research Laboratory. Photocathodes of MgF_2 (5000Å) were evaporated on a substrate of AL (3000Å) which had been evaporated on five mil optical mica sheets. The data compares favorably with that of Lukirskii [37].

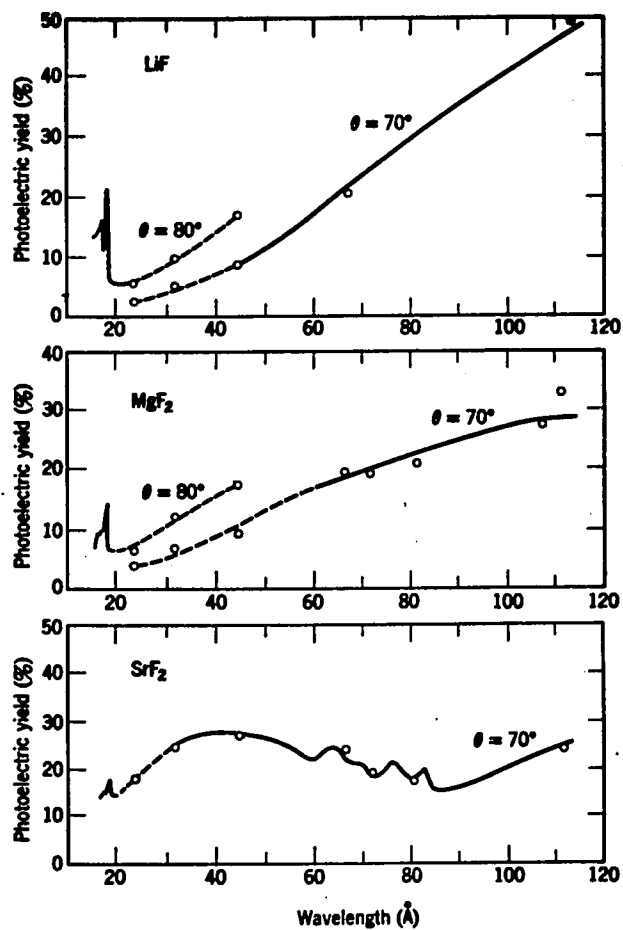
Of the alkali-halides, MgF_2 and LiF are the most practical from a stability point of view. The author's MgF_2 had been allowed to age several months before the calibration at NRL. Figure 23 illustrates the effect of aging (exposure to atmosphere) on MgF_2 and LiF. MgF_2 is clearly superior to the LiF if the photocathode is to be exposed to the atmosphere for any appreciable length of time. CsI is much more unstable than the LiF, lasting up to a few weeks at appreciable efficiency [35]. Conducting photocathodes in addition to their relative inefficiency are also more sensitive to u-v radiation than some of the alkali-halides, of which MgF_2 and LiF seem to be the least sensitive. Blank and Sorokin [45] have investigated the photoelectric emission of various metals with and without coatings of LiF and MgF_2 in the range 150 to 2200Å. The graphs in Figure 24 indicate that coatings of MgF_2 and LiF inhibit the photoelectric emission of nickel, copper, and aluminum.



Photoelectric yield of CsI and LiF as a function of the angle of incidence for selected wavelengths: x, 113 Å; o, 67 Å; ▲, 44 Å; ●, 31.4 Å; △, 23.6 Å

(From Lukirskii [37])

FIGURE 20



Photoelectric yield of LiF, MgF₂, and SrF₂ as a function of wavelength for radiation incident at an angle θ° to the normal. Solid line indicates data taken with a continuum light source; open circles represent data taken at discrete wavelengths

FIGURE 21
 PHOTOEMISSIVE EFFICIENCY OF VARIOUS ALKALI HALIDES
 (From Lukirskii [37])

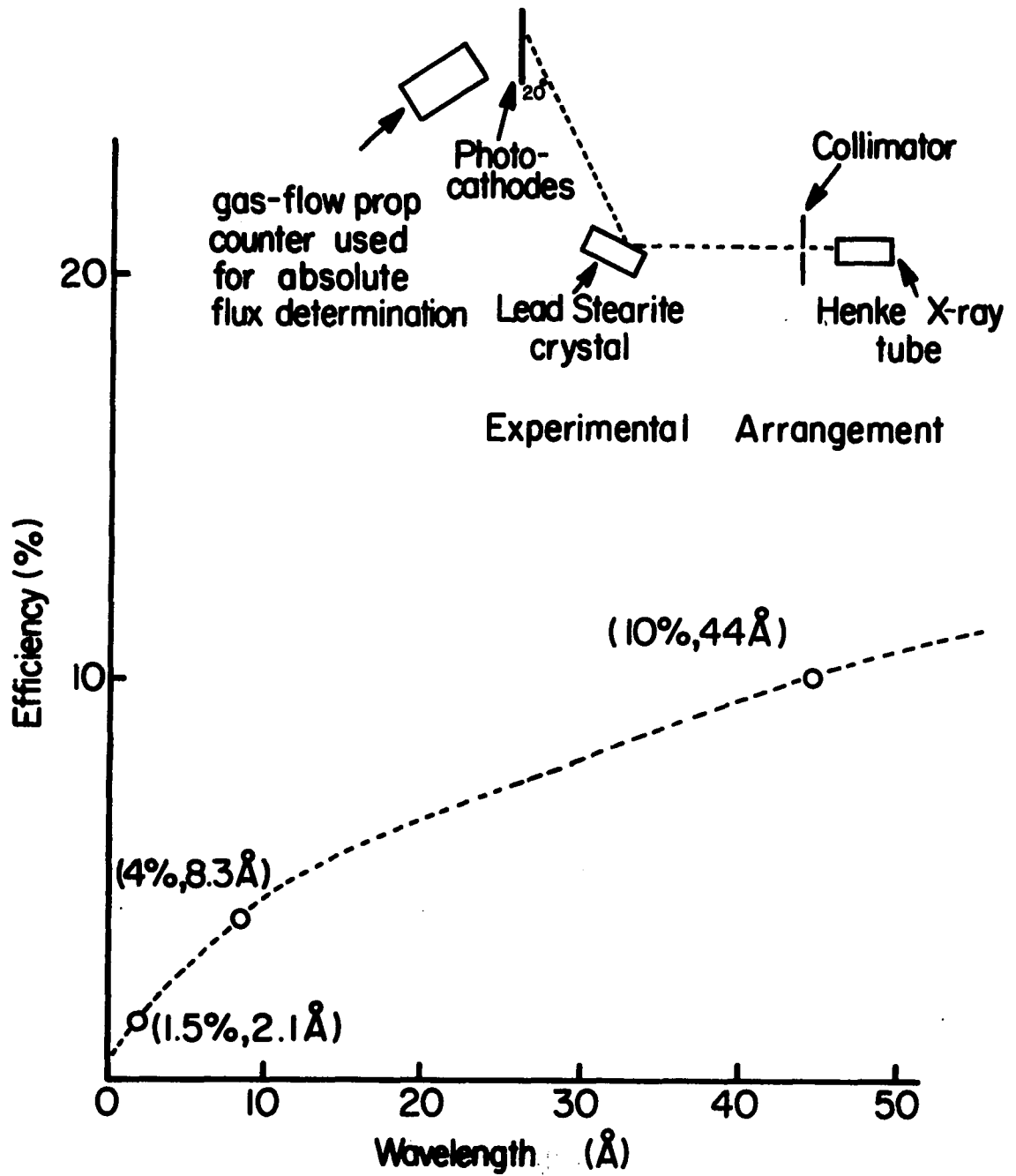
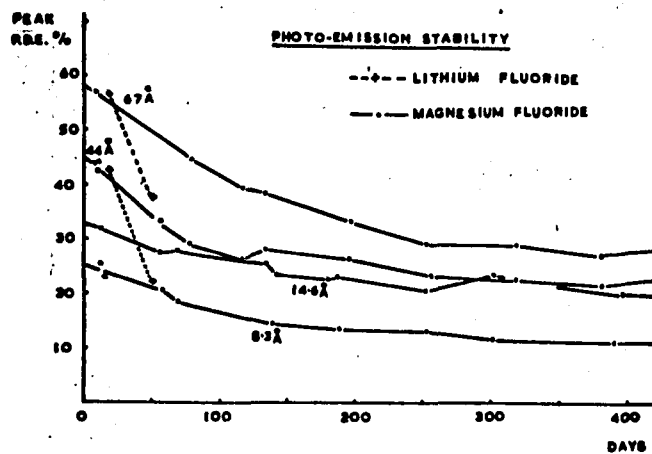
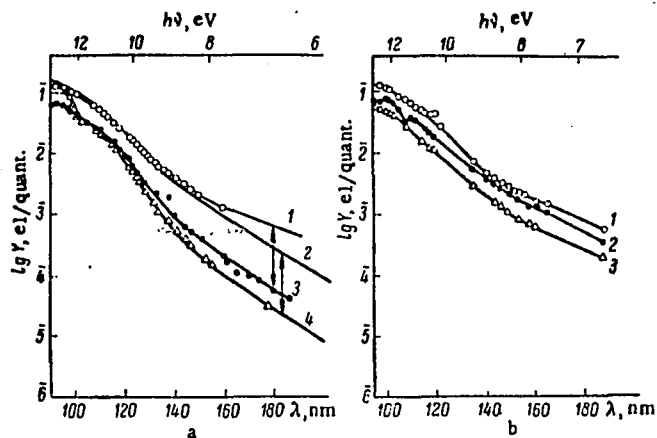


FIG. 22--AVERAGE EFFICIENCY OF MgF_2 SHEETS SET AT A GRAZING ANGLE OF 20° (AUG. 1971, NRL)



Variation of peak photon detection efficiency with storage time, after evaporation.

FIGURE 23
(D. SMITH [46])



Long-wave region in Y . a: 1) bulk nickel; 2) bulk copper; 3) ~500 nm LiF film on nickel; 4) ~500 nm LiF film on copper; b: 1) bulk aluminum; 2) ~500 nm MgF_2 deposited on hot aluminum; 3) ~500 nm MgF_2 deposited on aluminum at room temperature.

FIGURE 24
EFFECT OF ALKALI COATINGS ON AL PHOTOCATHODES
(BLANK AND SOROKIN [45])

2. General Design of Detectors

The desirable characteristics in an x-ray detector are: (1) large, cheap collection areas, (2) high efficiency, (3) discrimination against unwanted particles, and (4) directional characteristics. High efficiency implies that the photocathode surfaces be set at the small grazing angle with respect to the radiation. The obvious manner in which to obtain large areas at high efficiency is to synthesize the multiple photocathode configuration in Figure 25. The problem of photoelectron collection can be solved by an accelerating-focusing electric field and an electron detector. The electron detector may be sensitive to photons, consequently a good place for the electron detector is on the top of the photocathode configuration. Views of this placement are shown in Figure 26.

The type of electron detector which best fits the geometry of Figure 26 is a sheet of plastic scintillator with a photomultiplier mounted above it. The accelerating potential will be in the vicinity of ten kv. Another configuration which comes to mind, is the cylindrically symmetric conic photocathode of Figure 27. The electron detector might be a continuous photomultiplier type (channeltron) with a conic entrance; V would typically be several hundred to one thousand volts. The efficiency of these configurations could approach 100% if the multiple reflection-absorption technique is used, of which Figure 29 illustrates two types of geometry. Collimation and rejection of charges particles is simultaneously accomplished by inclusion of conducting plates in front of the photocathodes (Figure 28).

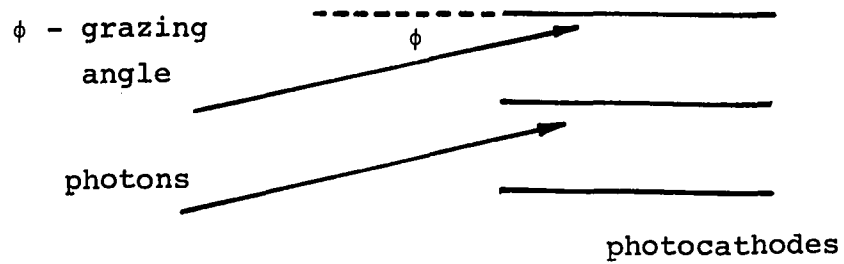


FIGURE 25
MULTIPLE PHOTOCATHODE CONFIGURATION

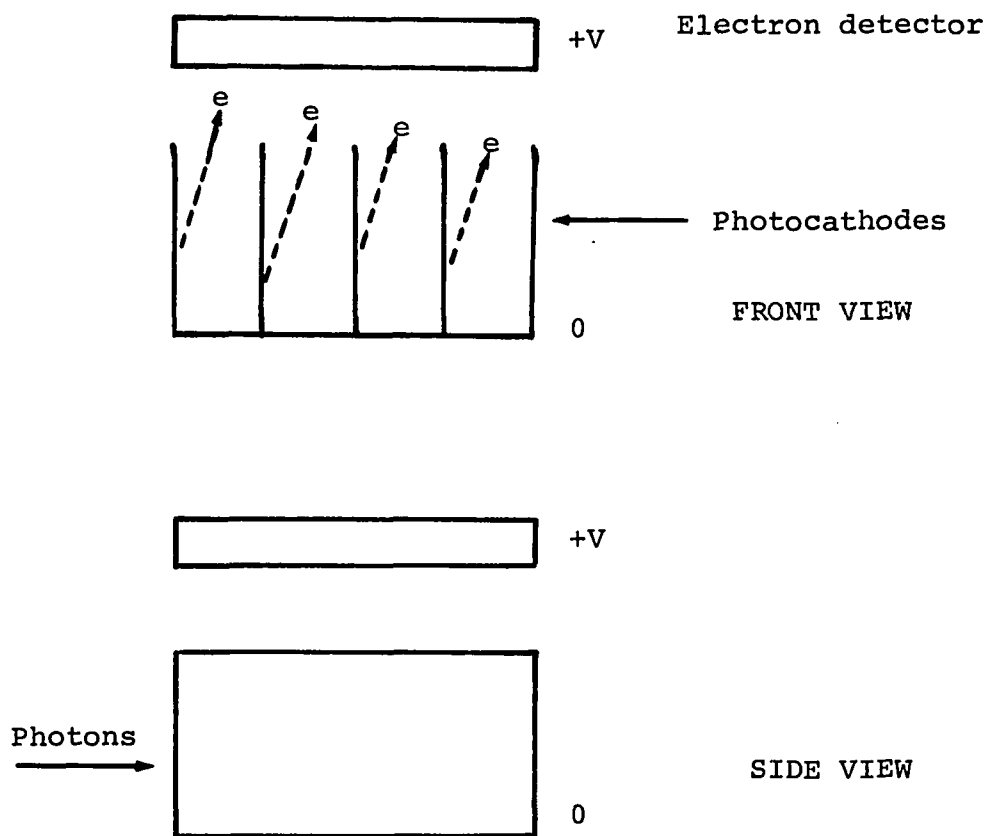


FIGURE 26
ELECTRON COLLECTION SCHEME

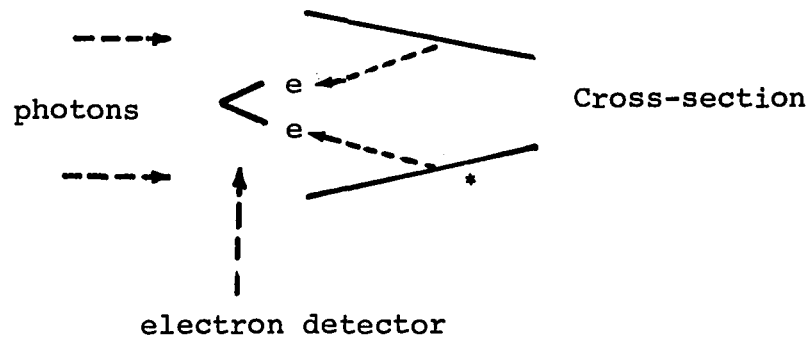


FIGURE 27
CONIC PHOTOCATHODE

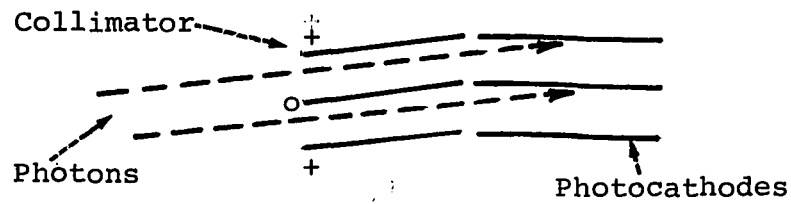


FIGURE 28
COLLIMATOR-DEFLECTION PLATE CONFIGURATION

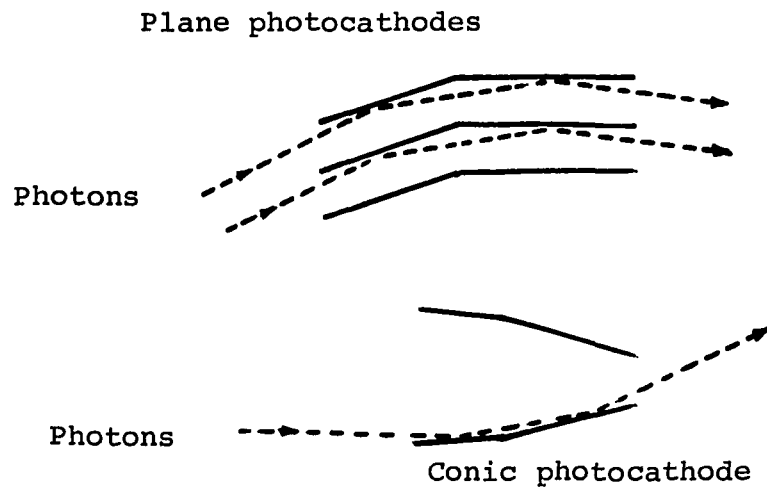


FIGURE 29
MULTIPLE REFLECTION-ABSORPTION PHOTOCATHODES

Low pass characteristics (energy domain) and extreme charged particle discrimination is achieved by placement of another set of reflector plates in front of the deflection plates as in Figure 30. A reflection coefficient of 50% or better should be possible in the ultra-soft x-ray band [41] and absorbers to achieve a high pass characteristic can be placed somewhere along the configuration. Since the absorber will usually be placed on a mesh, the best location for it is in front of the photocathode where the mesh will be an electrostatic shield for the photocathode. A black conductor can be placed after the photocathode to provide electrostatic shielding and an anti-reflection surface for u-v radiation.

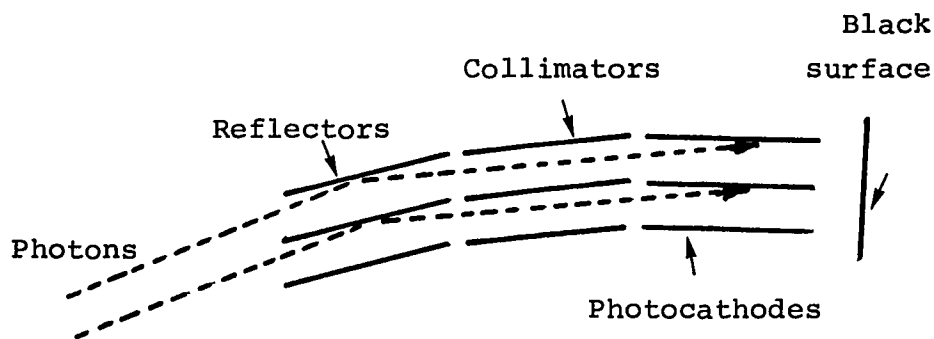


FIGURE 30

LOW PASS REFLECTOR DETECTOR

3. Detectors With Low Energy Resolution Capability

The synthesis of high pass, low pass and band pass filters (energy domain) provides a low resolution spectral analysis. The practical high pass filter is the absorber, for which the exponential law holds ($e^{-\mu t \rho}$). Low pass filtering can be realized in two ways: (1) reflection techniques and (2) photocathode techniques. At the critical angle of reflection, the reflection coefficient becomes appreciable. Figure 31 is from Lukirskii [41] and illustrates the dependence of critical angle on energy for aluminum. If the detector geometry is such that the photons are reflected before striking the photocathode, then low pass transfer functions are obtained (Figure 32). For example, if a low pass cutoff is desired at 250 ev, a Cr reflector set at an angle of eight degrees with respect to the collimator provides the proper cutoff, (Figure 33). The fact that the collimator angular response is not a delta function will introduce deterioration of the "roll-off" characteristic, but usually detectors are rotating through fields of view, and the exact low pass response of the rotated reflector can be calculated by averaging over the collimation angle.

$$\overline{R(\theta, E)} = \frac{\int_{\theta_1}^{\theta_2} R(\theta'; E) \theta(\theta'; E) d\theta'}{\int_{\theta_1}^{\theta_2} \theta(\theta'; E) d\theta'}$$

where $R(\theta'; E)$ is the reflectivity and $\theta(\theta'; E)$ is the angular response of the photocathode collimator.

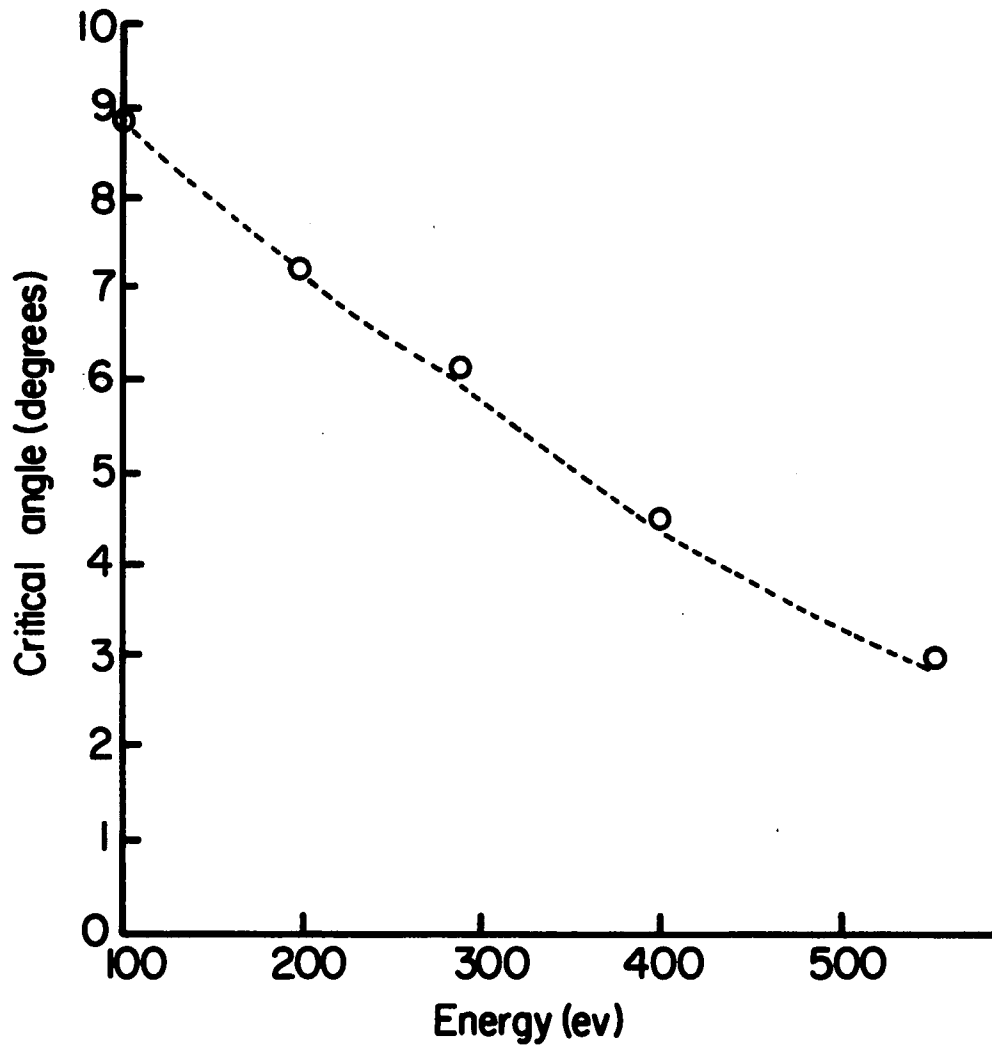


FIG. 31--CRITICAL ANGLE OF REFLECTION vs PHOTON ENERGY FOR ALUMINUM (Lukirskii [41])

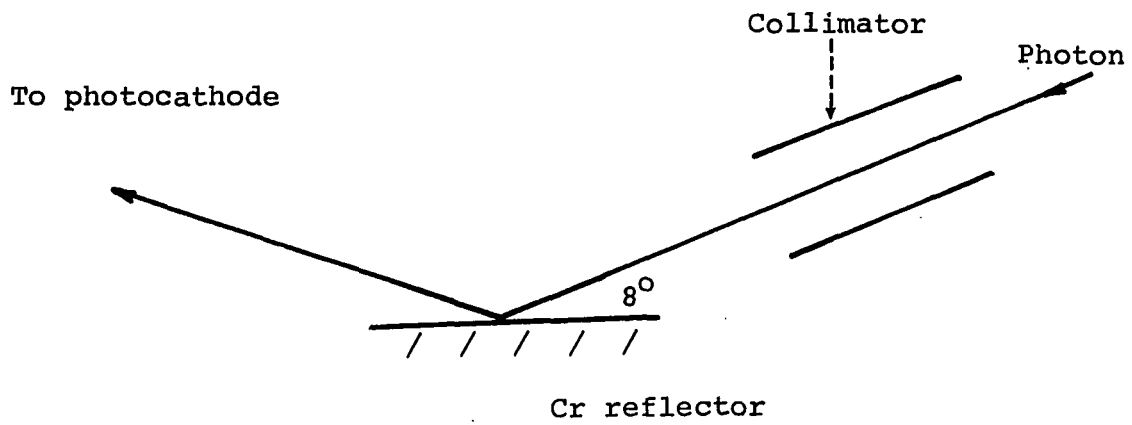


FIGURE 32
LOW PASS DETECTOR CONFIGURATION

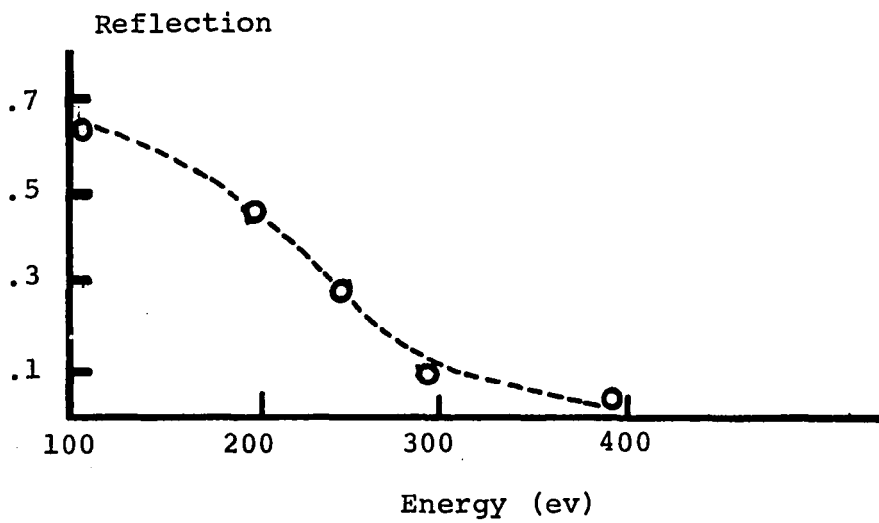


FIGURE 33
LOW PASS Cr REFLECTOR FILTER

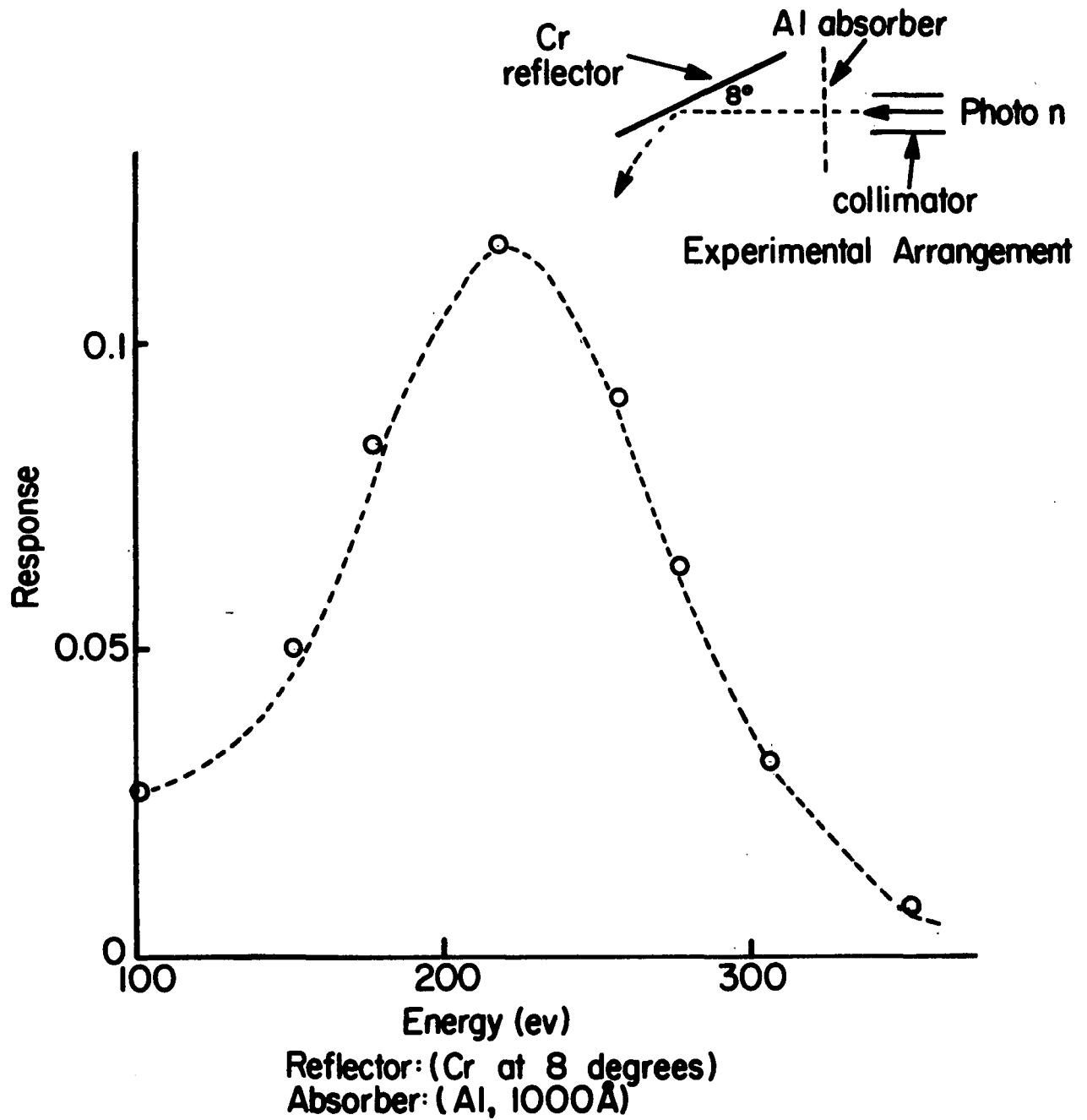


FIG. 34 -- BANDPASS FILTER

CHAPTER IV
ULTRA-SOFT X-RAY DETECTOR

An ultra-soft x-ray detector using the principles of spectrum analysis and detector construction described in Chapters II and III respectively, was designed and built for a sounding rocket flight to investigate the ultra-soft x-ray component in the lower ionosphere (Chapter V) and the ultra-soft x-rays from extra solar objects.

1. Geometry

Because the method of spectral analysis chosen requires different thickness absorbers, it is useful to picture the x-ray detector as four thickness bins (a bin is an absorber-photocathode combination). Each thickness bin consists of the angled, flat, parallel photocathode array described in Chapter III, with the photocathodes placed at an angle of ten degrees with respect to the collimators (Figure 35). Because of telemetry limitations, it was decided to time-share two thickness bins with one electron collector (Figure 36). The secondary electrons produced by the photoelectron in the photocathode are accelerated and focused to an electron detector. Each bin is time-shared by alternately deactivating each portion of photocathode assembly. The collimators are used as deflection plates for rejection of low energy (10 kev) charged particles. The collimator configuration seen in Figure 35 is such that the fluorescent x-rays produced by deceleration of the electron

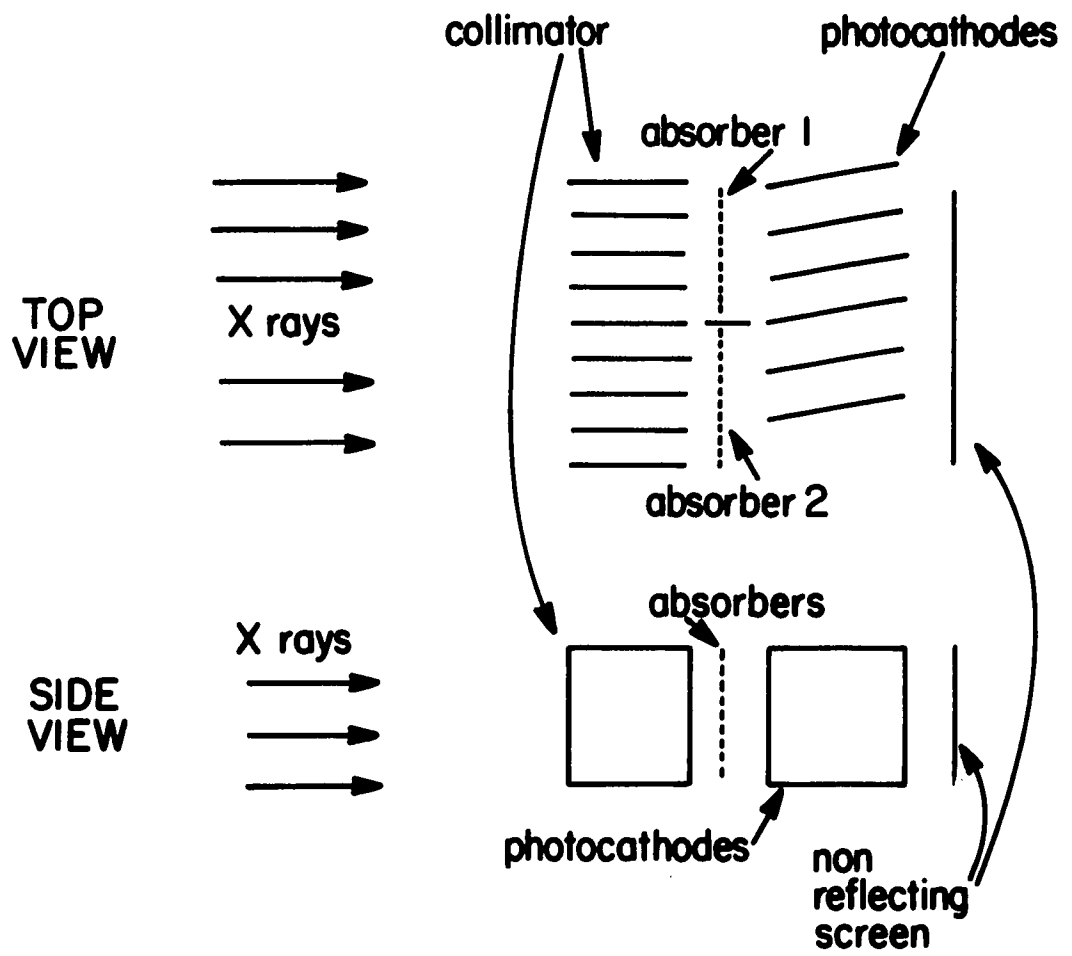


FIG.35--BASIC X-RAY DETECTOR

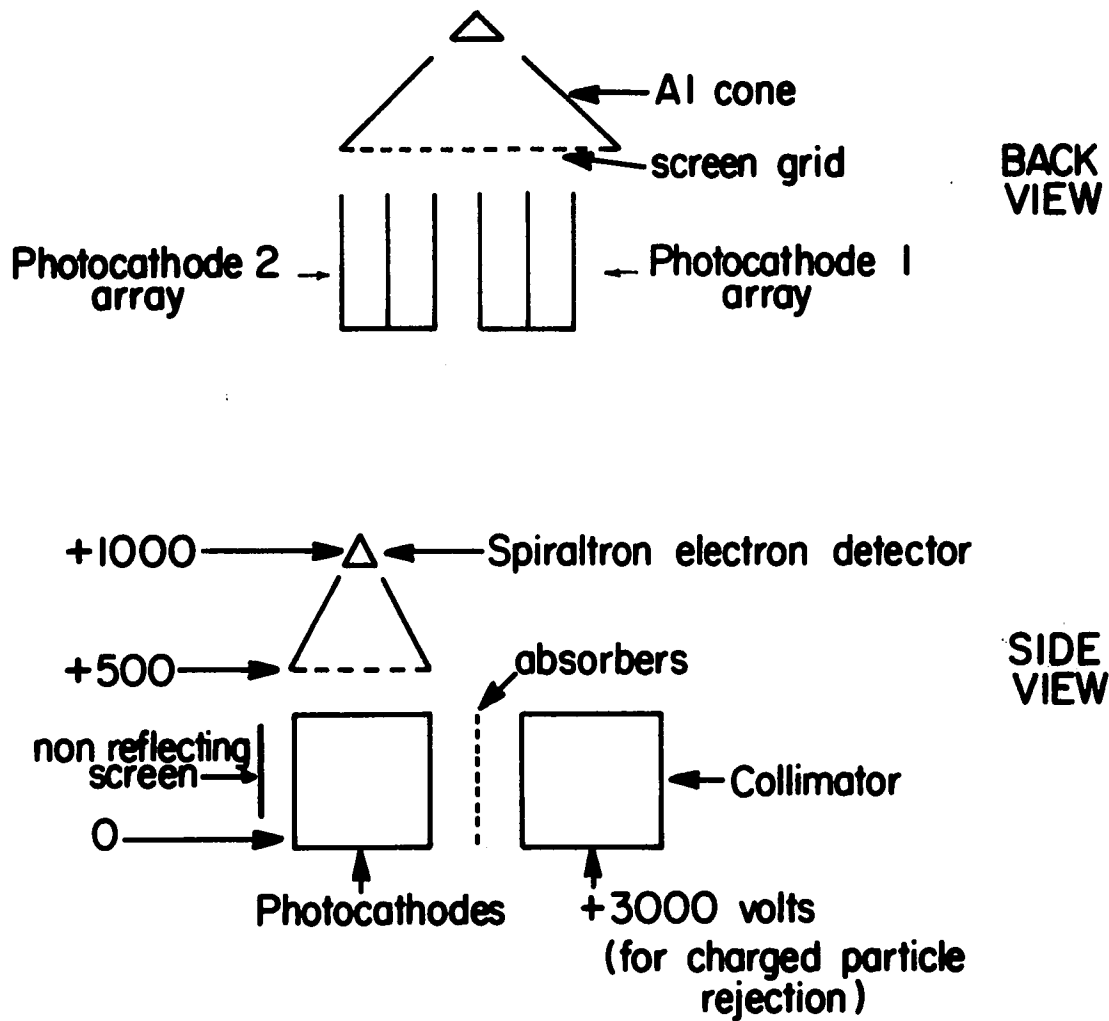


FIG. 36--BASIC X-RAY DETECTOR ELECTRON COLLECTION

upon striking the collimator should be negligible, considering the geometry and the fluorescent x-ray production efficiency of the rough graphite coatings on the collimators [14].

The secondary electron focusing scheme is shown in Figure 36. The photocathode arrays are held at ground potential, and the electrons are accelerated to the grid, which is held at +500 volts. Once into the cone, the electrons are accelerated into the electron detector, which is held at +1000 volts. A photocathode array is deactivated by switching from ground potential to +1000 volts. The electron detector is a continuous multiplier type (Bendix spiraltron) with a conic entrance. An electron striking the entrance of the spiraltron causes an avalanche of 10^8 electrons which is detected by the electronics. Figures 37 and 38 are photographs of the actual instrument. The collimators, visible in both photographs, are below the housing for the pre-amps. The two vertical cylinders are the high voltage power supplies, and the circuit board on the opposite side from the high voltage supplies is the post pre-amp circuitry. The spiraltron electron detectors are in the rectangular solids behind the pre-amp housings. The photographs were taken before final wiring and potting. The whole array of photocathodes and collimators is mounted in a lucite structure to provide high voltage insulation. The signal processing is discussed in the last section of this chapter.

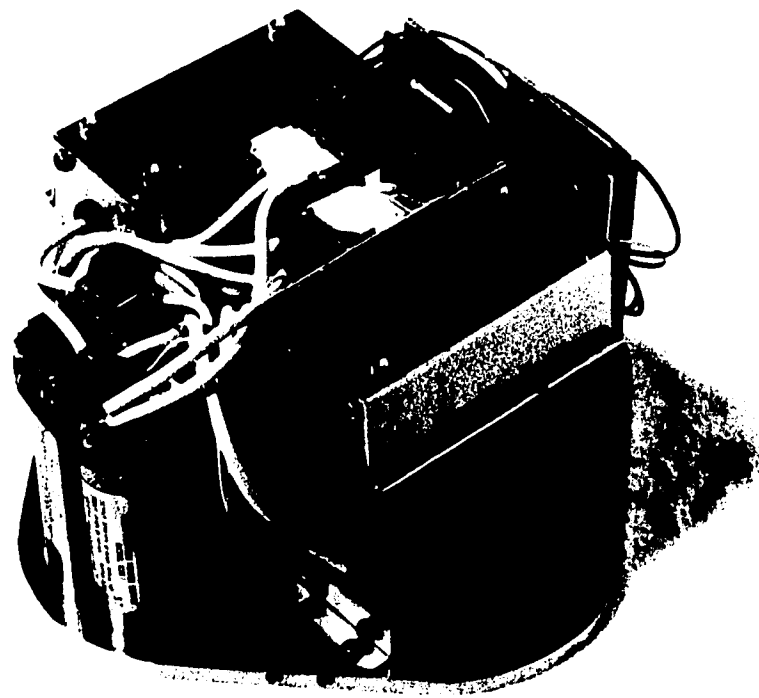


FIG. 37 DETECTOR (H.V. SIDE)



FIG. 38 DETECTOR (ELECTRONICS SIDE)

2. Detector Characteristics

a. Angular Response. The angular response in Figure 39a is an asymmetric response as a result of the photocathode's properties (Chapter III). The sharp rise on the decreasing θ side is due to the sudden exposure of the active side of the photocathode, while the tail on the increasing θ side is due to the collimation. The sharp edge is extremely useful in providing good angular resolution of solar or stellar positions, and in providing an A-C signal for absolute flux measurements.

b. Photocathodes. The structure of the photocathodes is illustrated in Figure 40a. Five thousand Angstroms of MgF_2 was evaporated on 3000\AA of aluminum which had been evaporated on 5 mil optical mica. The aluminum and MgF_2 evaporation rate was first calibrated in a vacuum chamber and then several photocathodes were simultaneously synthesized. Uniform thicknesses which were measured with a Tolansky interferometer were assured by use of multiple MgF_2 and Al sources in the vacuum chamber. The efficiency of the photocathodes from $5\text{-}3000\text{\AA}$ at an angle of incidence of 80 degrees (Figures 41 and 42) were determined by combining the author's data, which is the result of direct calibration of the photocathodes at the Naval Research Lab in 1971 (Chapter III), and the data of Pounds [46], Lukirskii [35], Savinov [36], and Sorokin [37]. The uniformity in spectral response of the different sheets of photocathode was good to less than ten percent. The mica-Al- MgF_2 configuration was glued to thin sheets of aluminum for rigidity in the lucite assembly of the x-ray detector.

Photocathode Angular Response (normalized to 1)

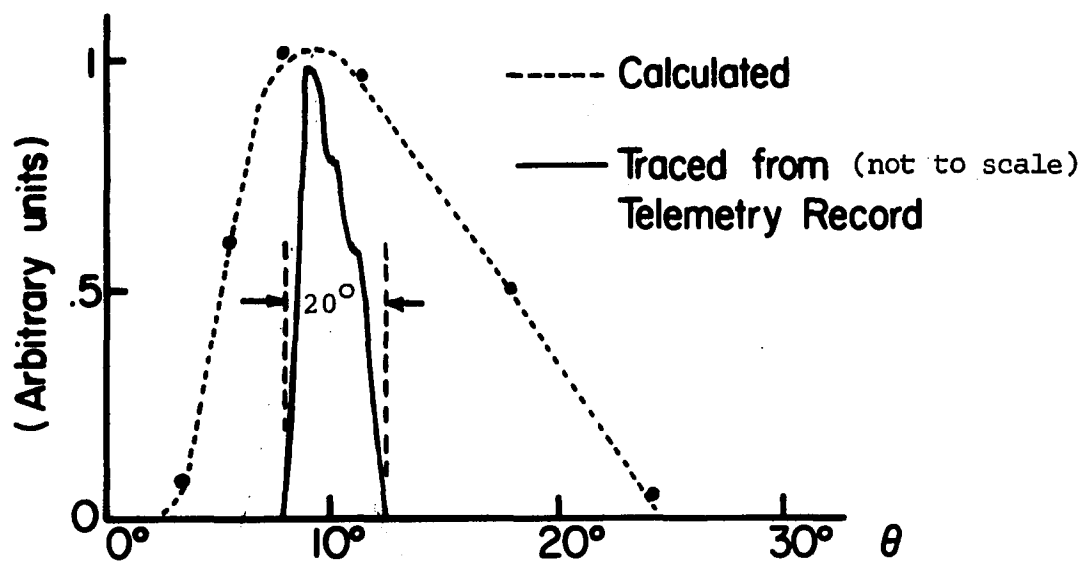


FIG. 39a--DETECTOR CALCULATED ANGULAR RESPONSE(44Å)

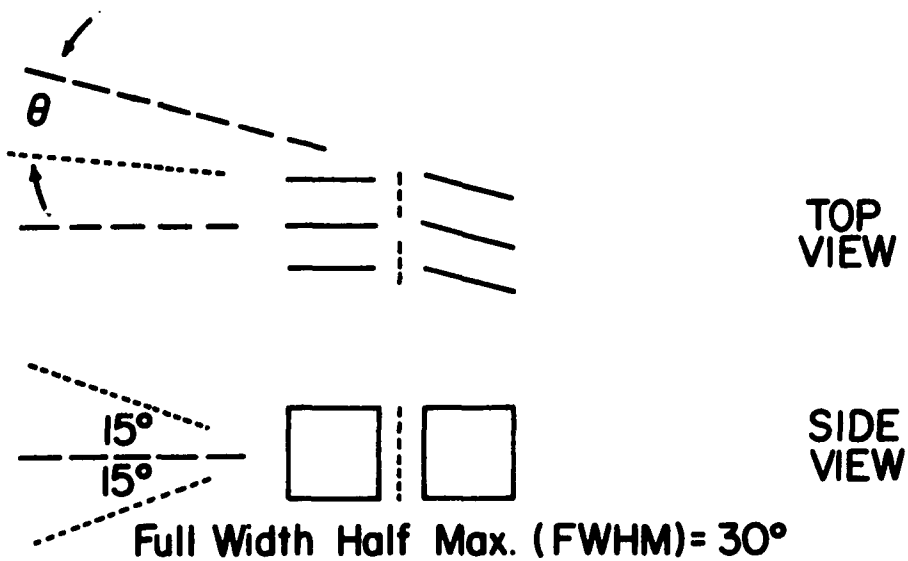


FIG. 39b--DETECTOR GEOMETRY

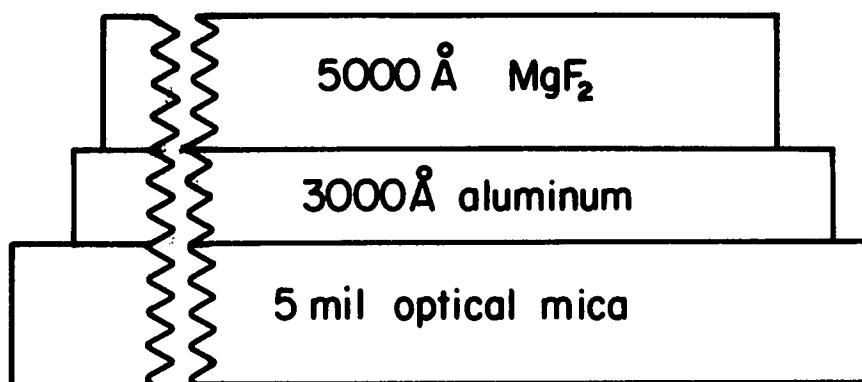


FIG. 40a--PHOTOCATHODE

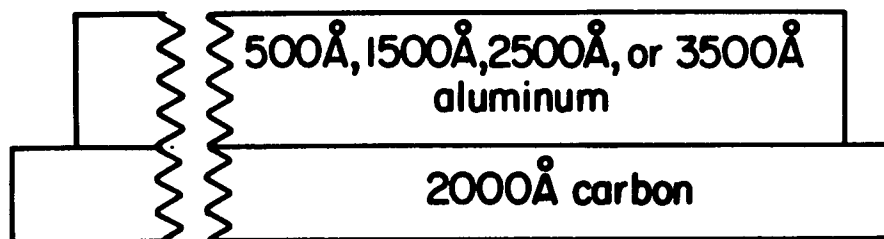


FIG. 40b--ABSORBERS

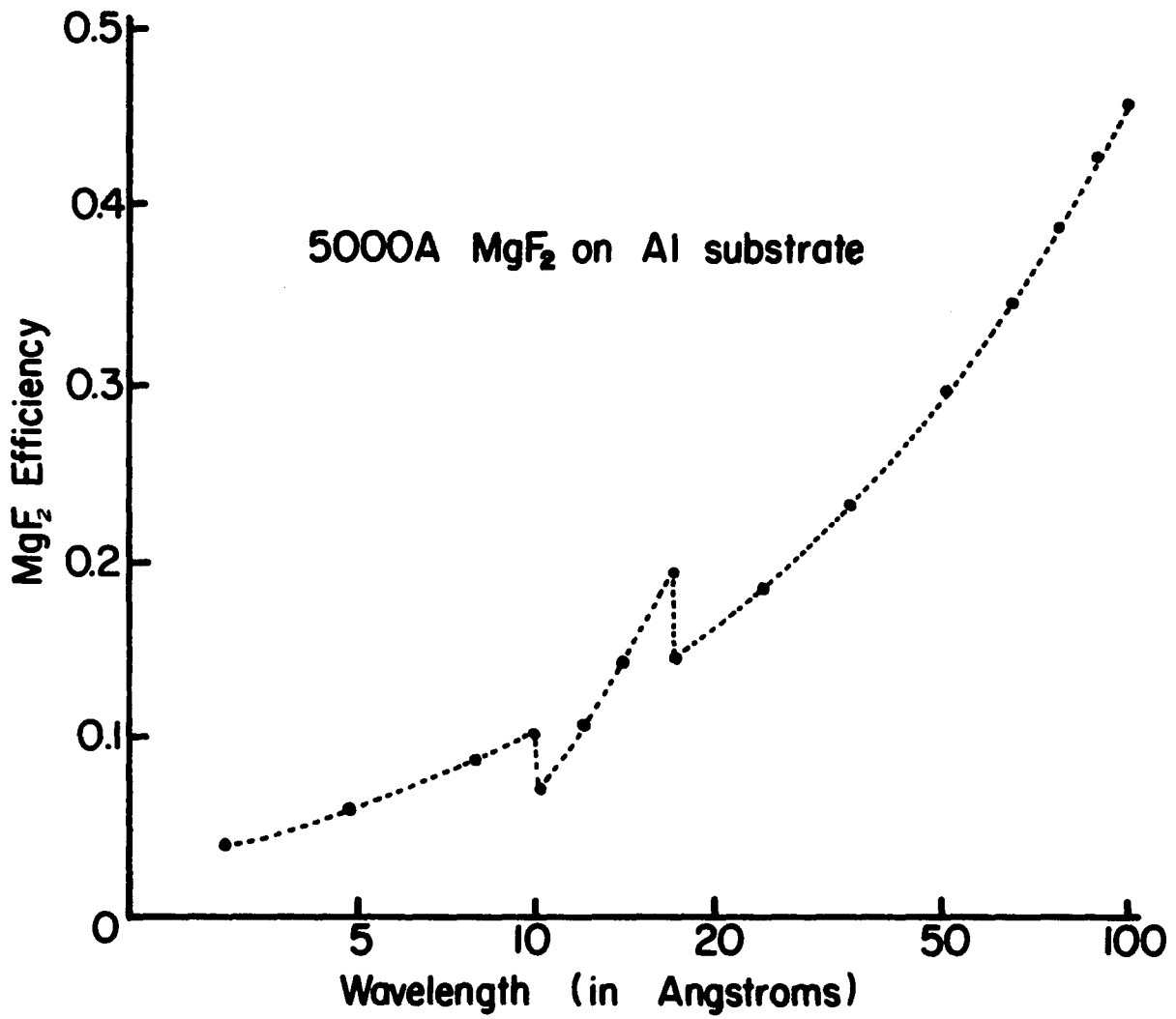


FIG. 41--EFFICIENCY OF MgF₂ (5-100Å)

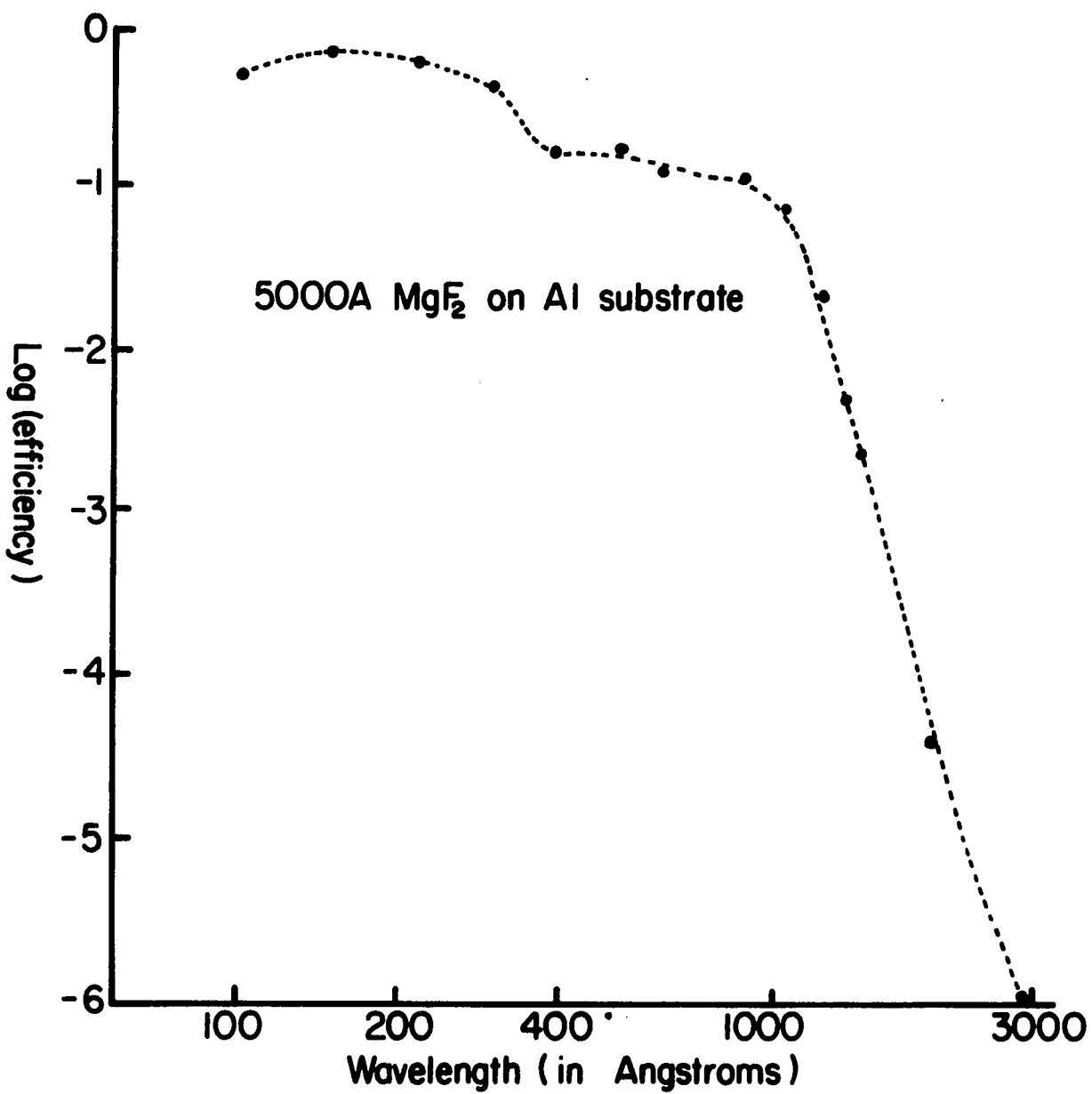
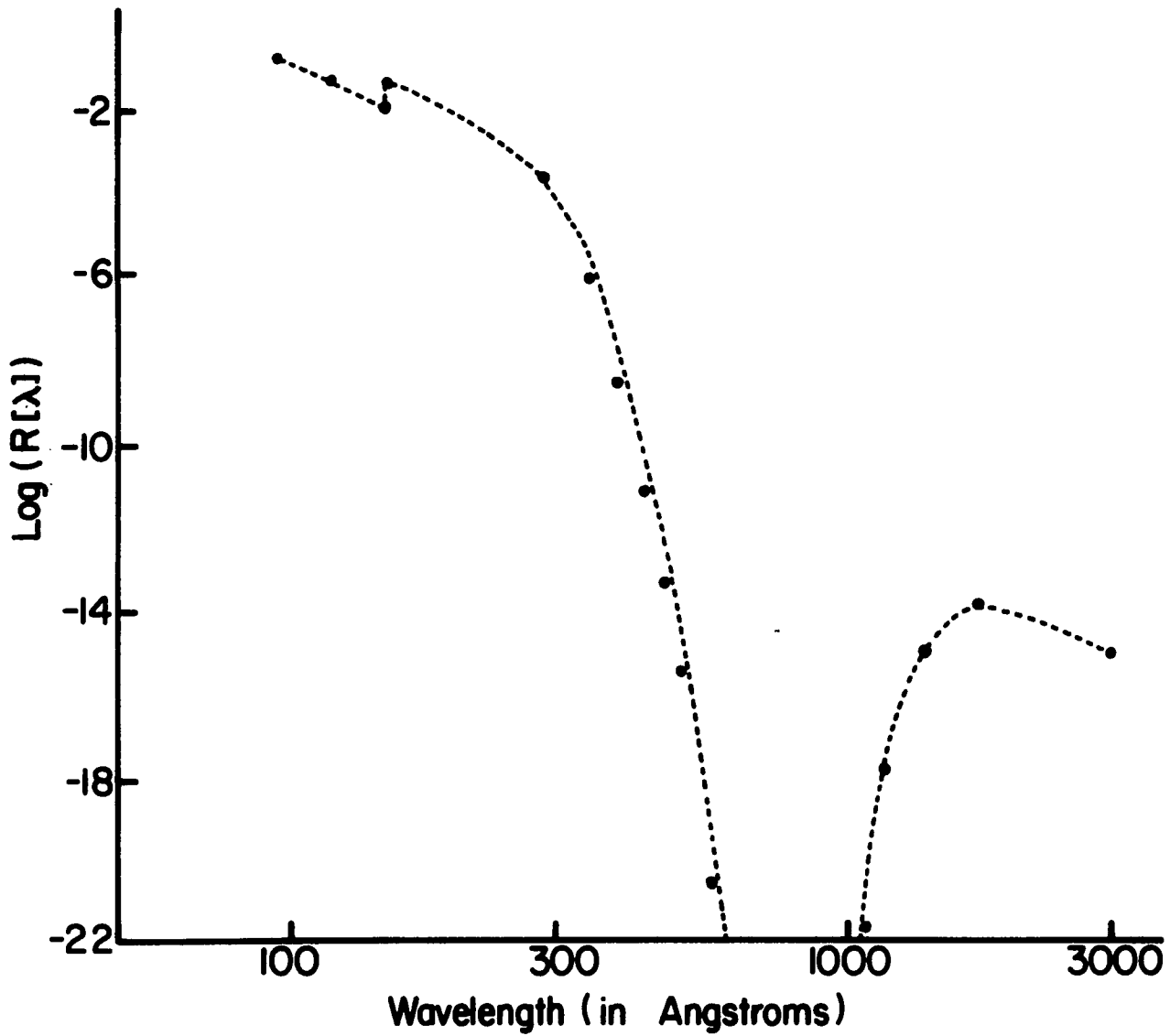


FIG. 42--EFFICIENCY OF MgF₂ (100-3000^oA)

c. Absorbers. The four absorbers are all composite aluminum-carbon films, consisting of 2000^oA of carbon; and 500, 1500, 2500, and 3500 Angstroms of aluminum, depending upon the absorber bin (bin refers to one of the absorber-photocathode array sections). Figure 40b illustrates the absorber structure. The carbon films were purchased on glass slides with a release agent such that the carbon films could be floated off on distilled water. The carbon films were scrutinized for pinholes by holding them up to a bright light. The four layers of aluminum were evaporated onto pinhole free carbon films, which were still on glass slides; thicknesses were measured with a Tolansky interferometer to within five percent. Uniformity in thickness over the whole film was maintained by use of a multiple aluminum evaporation source in the vacuum chamber. Film thickness variations were maintained at somewhat less than ten percent over the whole surface for each thickness of aluminum. The composite films were floated off the glass slides and picked up by framed eighty percent transmission Buckby-Mears nickel mesh. The shock-mounted frames had been made to fit into a space between the collimators and the photocathodes in the lucite assembly. After vibration and u-v rejection tests at NRL, the pinhole free films were selected for use on the flight.

d. Spectral Response. Adequate rejection of u-v is provided by the insensitivity of the MgF₂ photocathode to u-v coupled with the carbon-aluminum absorbers. The most u-v sensitive absorber bin is the 500^oA aluminum bin; the total response of which is graphed in Figure 43,utilizing the spectral

FIG.43--DETECTOR U-V RESPONSE, $R[\lambda]$

response function $R(\lambda)$ (the transmission) defined by Fomichev [47] for aluminum, and the carbon absorption data which was obtained from Samson [48]. The u-v flux from the sun is of the order of 10^{15} photons/second/cm² in the 2500-3000Å range, and the rejection in Figure 43 of u-v in the 3000Å region is about 10^{13} , insuring adequate rejection of u-v. At NRL in 1971, the configuration of absorber-photocathode was exposed to a u-v lamp which NRL uses in testing aluminum windows; no significant flux was observed although the lamp puts out a flux of approximately 10^{14} photons/cm²/sec at a distance of one meter. The response of the detector excluding the aluminum films; that is, the carbon absorber-photocathode response, is given in Figure 44. The carbon absorption coefficients are obtained from Henke [34].

3. Electronics

A major difficulty in processing the output of the 5-150Å detector is the large dynamic range of the photon flux. The continuous photomultiplier electron detector emits an analog current for large flux values and a pulse for single events; thus a combination of analog-digital processing seems to be the solution for this instrument. The continuous multiplier, the mechanism of which has been investigated [49, 50], is a Bendix spiraltron with a conic entrance, five mm in diameter. The electron gain as a function of output pulse rate of the spiraltron is graphed in Figure 45, while a current output vs. output pulse rate graph (derived from the gain graph) is shown in Figure 46. The spiraltron is operated at about 3200 volts,

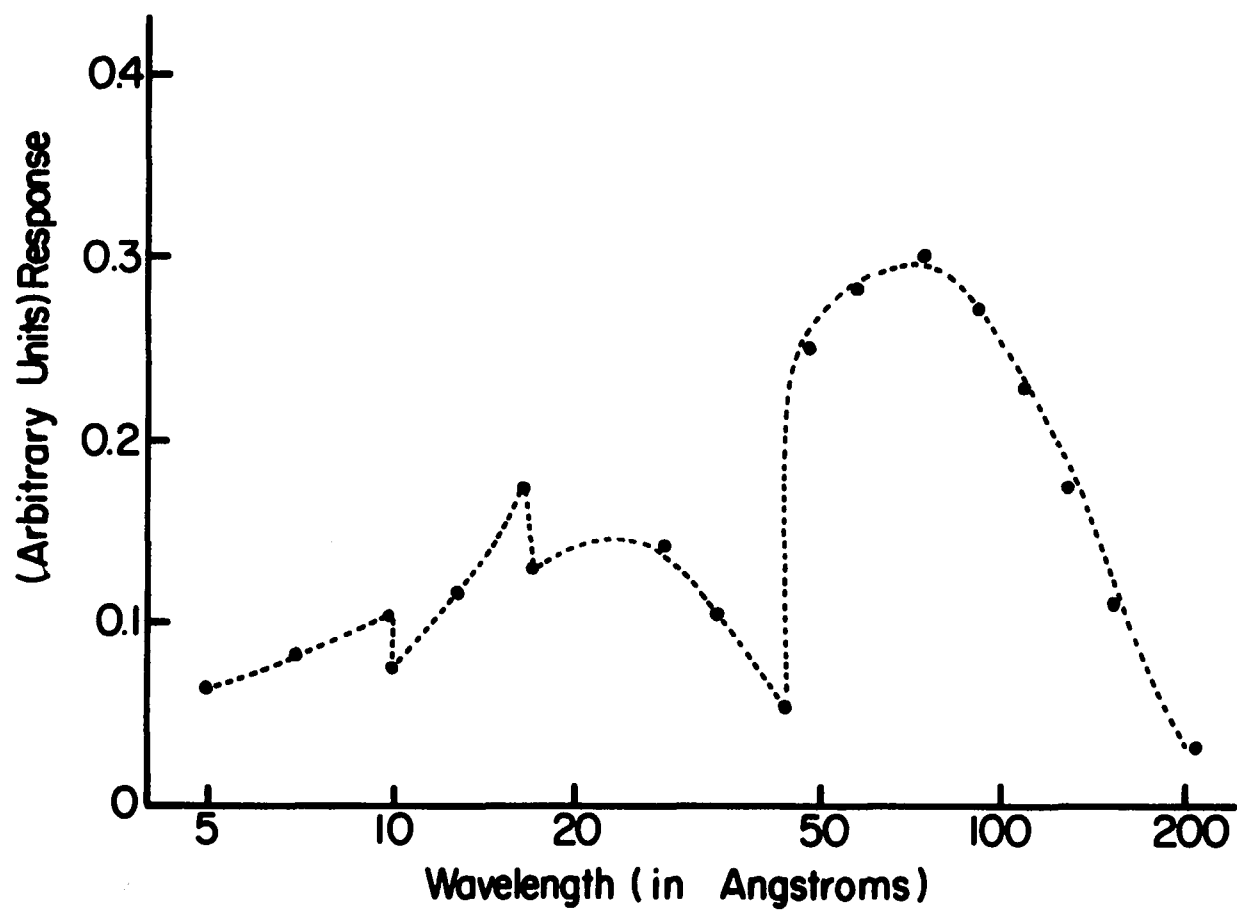


FIG. 44--CARBON ABSORBER-PHOTOCATHODE RESPONSE

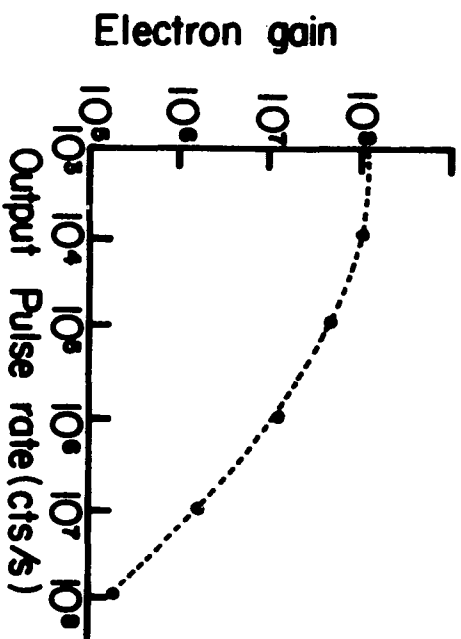


FIG. 45--SPIRALTRON ELECTRON GAIN

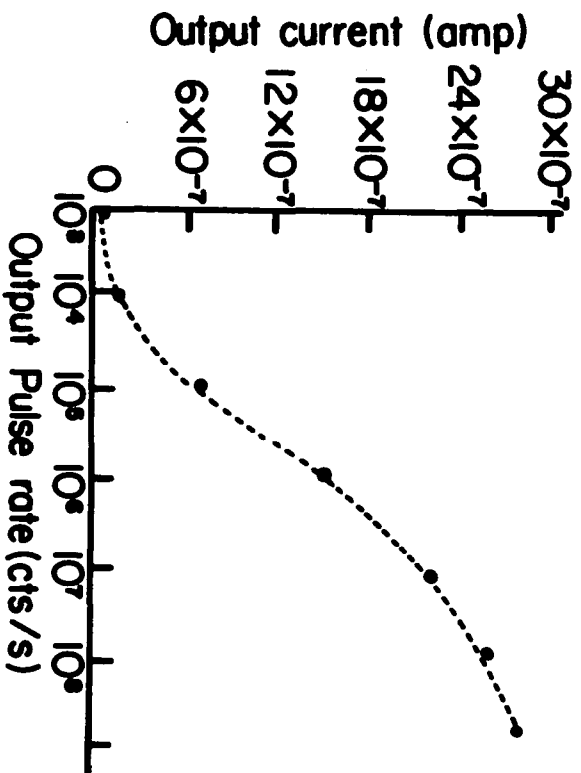


FIG. 46--SPIRALTRON OUTPUT CURRENT

which sets the electron gain at 10^8 for pulse rates of 10^4 c/s [51]. The photon flux from the sun should be about 10^9 Ph/s-cm² ($\lambda < 120\text{\AA}$); in the thin window bin only, (which has an area of 10 cm² at an average efficiency of 20%) the maximum counting rate experienced should be 2×10^9 counts/sec. The usual pulse counting circuit for the spiraltron is shown in Figure 47. In the Figure 47 configuration, with the end of the spiraltron tightly capped by a brass cylinder, a voltage pulse is produced across R when an electron enters the conic front and induces an avalanche.

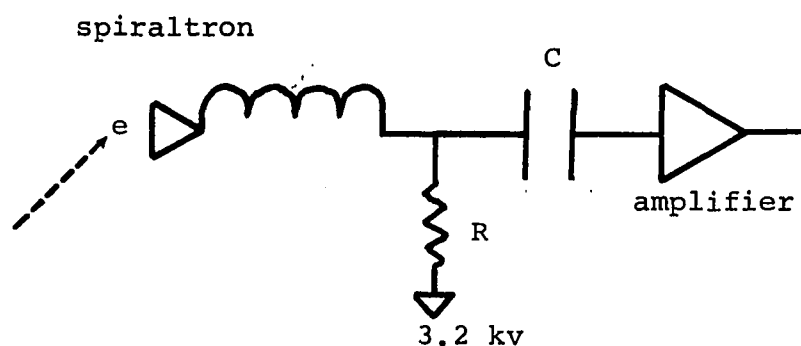


FIGURE 47

PULSE COUNTING CIRCUIT

The current pulse from the spiraltron is essentially a delta function, but the capacity to ground causes the voltage pulse to diminish in amplitude and decay in finite time. The true analog configuration (with a separation between the spiraltron and cap) isolates the 3.2 kv from the amplifier by use of this anode type electron collector. Since the mechanical difficulties in physically mounting the analog configuration are legion, the circuit in Figure 47 is the better choice. Normally, analog (dc)

information cannot be obtained with the circuit, but since point sources of photons will appear as a .01 second wide pulse, it is sufficient (for obtaining information) to make certain that the low frequency cutoff of the circuitry is lower than most of the Fourier components of the pulse. X-rays from the airglow component [13] will be modulated as a function of azimuth. To be able to detect such a modulation, the low frequency cutoff should be around ten hz.

The telemetry is capable of handling rates of 1000 cts/sec and below, so the analog data will range from $.3 \times 10^{-7}$ to 30×10^{-7} amps as seen in Figure 46. Since the current is drawn through a 1 meg resistor, the voltage range is .03 → .3 volts. Figure 48 shows a block diagram of the electronics, with details of the circuitry shown in Figures 49 and 50. Economical use is made of the three telemetry channels by combining two signals on one channel. The pulse information from detector 1 and detector 2 are weighted (3:2) and summed; and inserted into one telemetry channel. The analog information from the detectors goes to separate telemetry channels since there is no way of distinguishing between detector signals. The photocathode arrays (bins) are alternately deactivated by switching +1000 volts. On each analog channel a square wave from the high voltage switching oscillators is superimposed on the analog data to provide information on which bin is active. The period of the switching voltage, which will not interfere with the analog data significantly, is three seconds. All the amplifiers and weighters have to be set properly to insure that the voltages injected into the telemetry channels are constrained

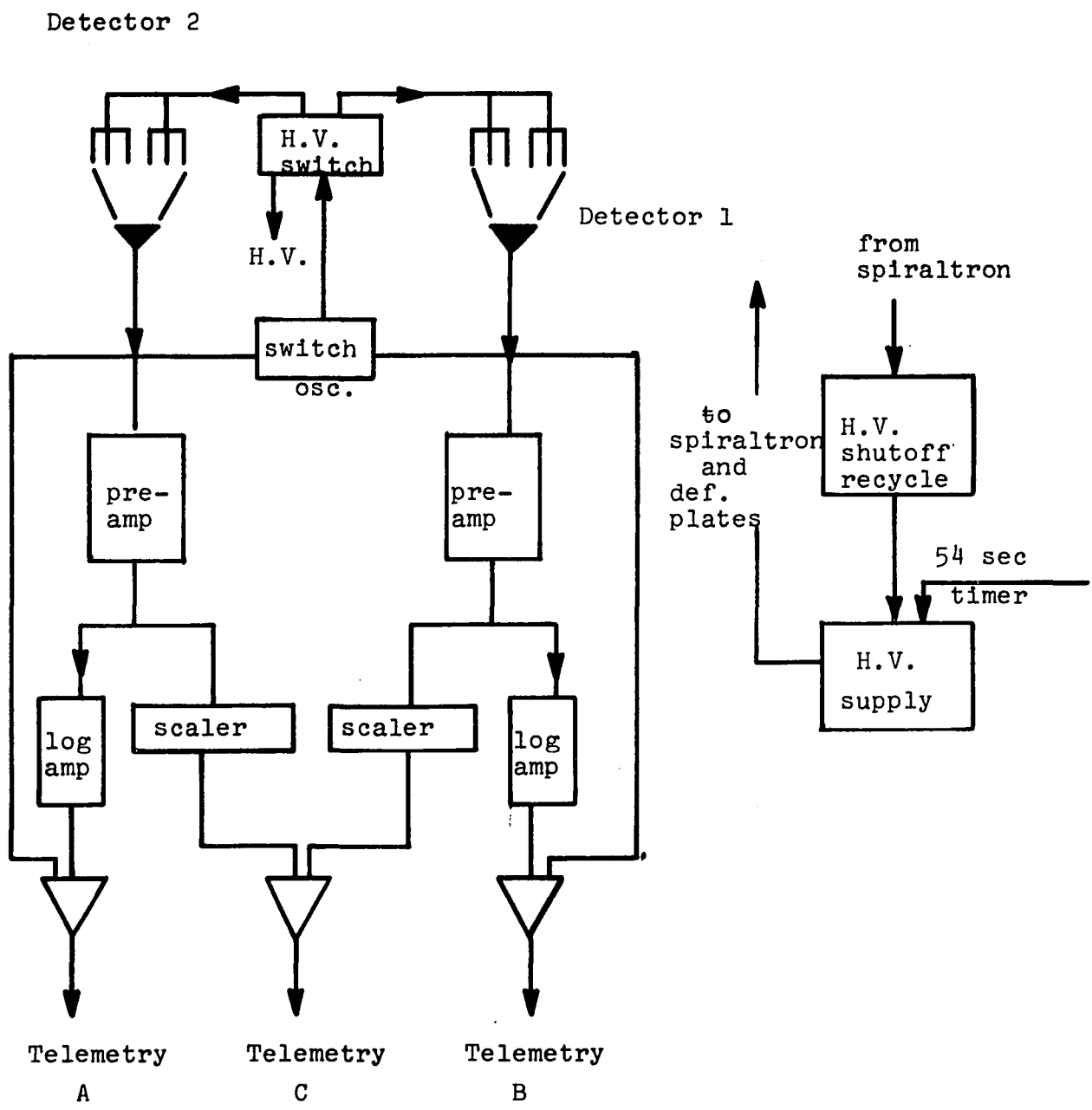


FIG. 48--BLOCK DIAGRAM OF ELECTRONICS

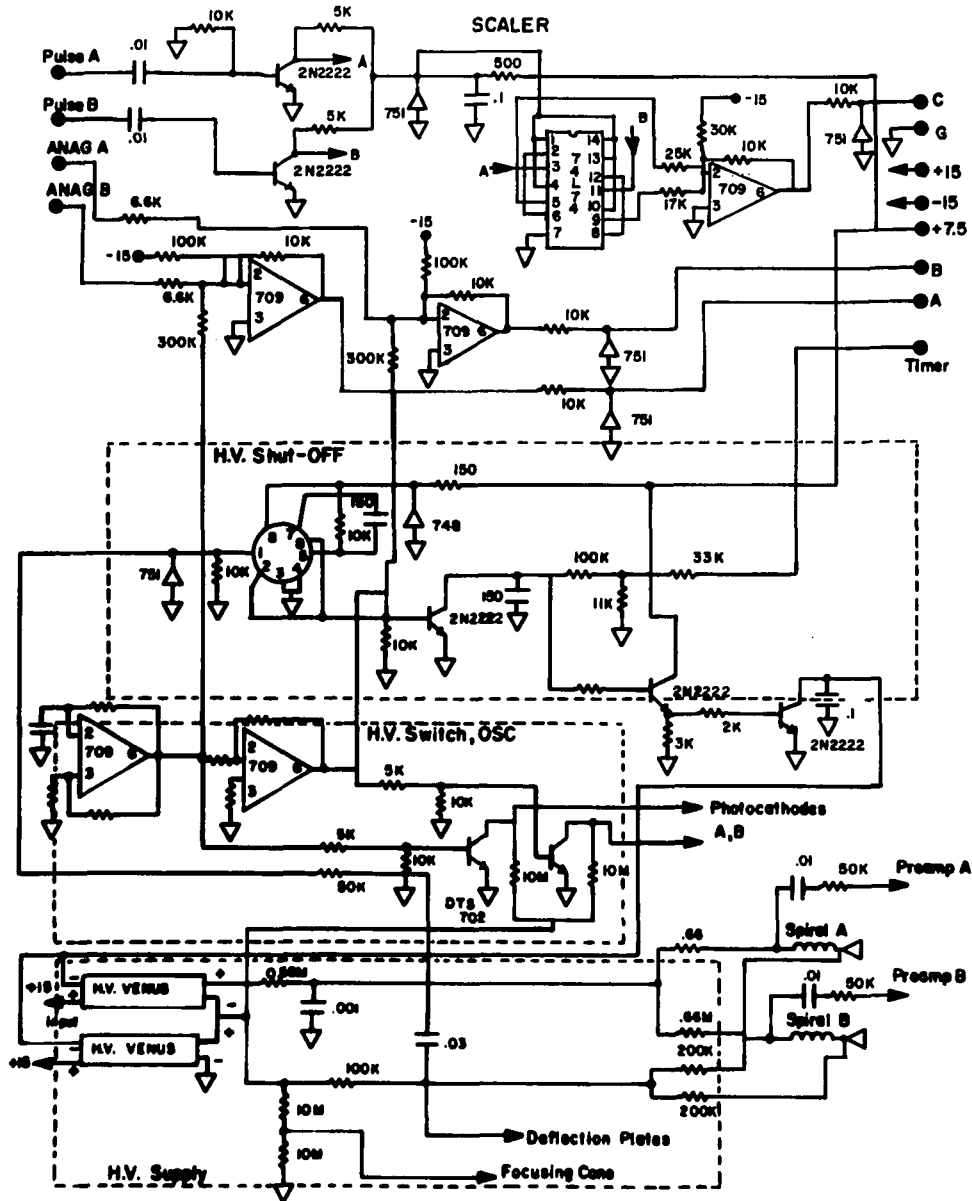


FIG. 49--POST PRE-AMP ELECTRONICS

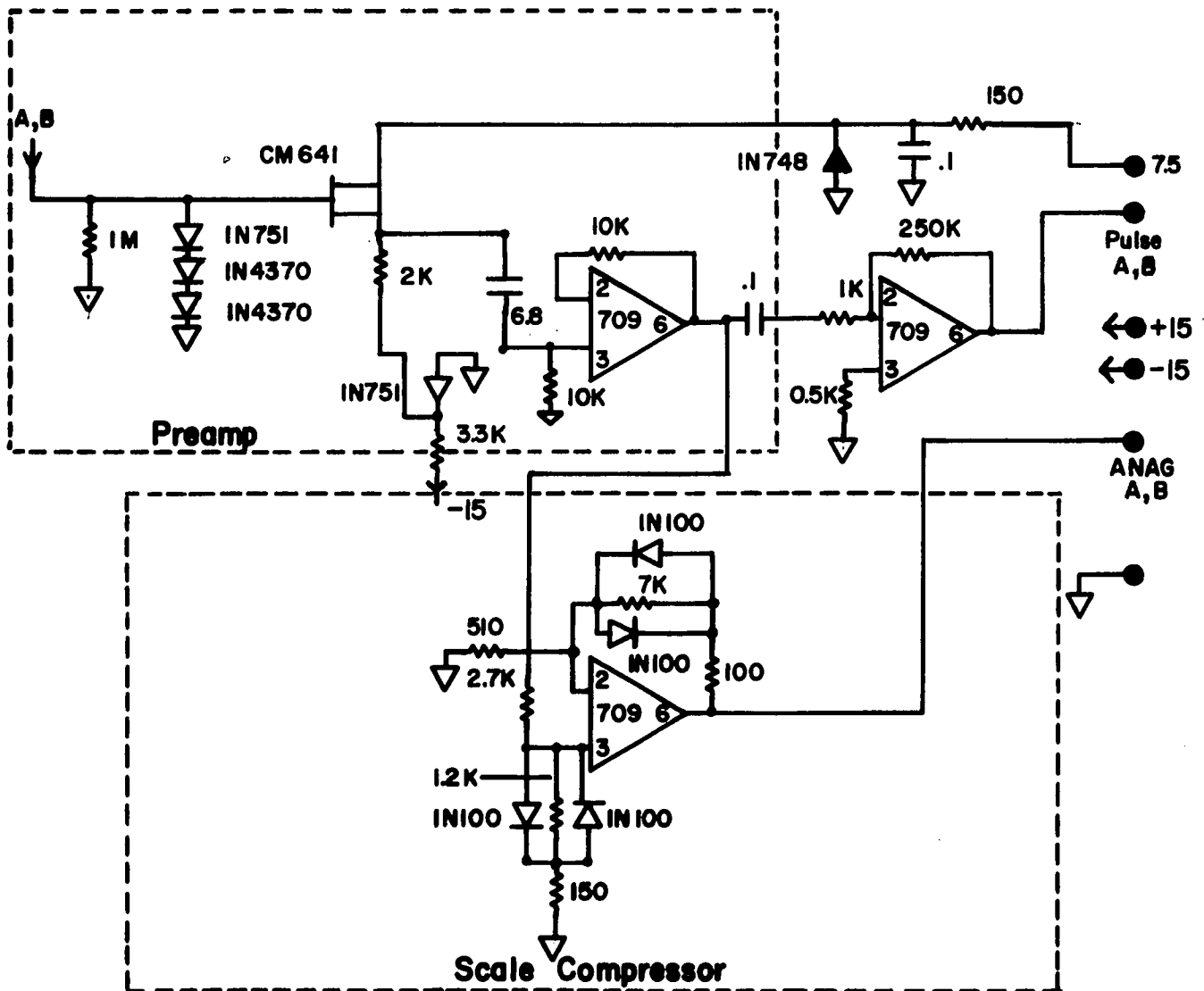


FIG. 50--PREAMP AND SCALE COMPRESSOR

between zero and five volts. Since voltages from 3 to .03 are expected, and only one telemetry channel was available, a simple scale compressor with the characteristics graphed in Figure 51 was necessarily developed. Figure 52 shows the output after conversion from input voltage to pulse rate; from which it is possible to obtain flux data. The high frequency cutoff of the analog circuitry is about 200 hz, which was thought to be adequate to pass the .01 second pulse from any point source.

The spiraltron arcs if the pressure is greater than $.5 \times 10^{-2}$ torr (the pre-amp is protected by diodes), consequently if the system is to be turned on at 75-85 km, some means of protection is necessary because of the ill-defined pressure in the payload. While the doors are ejected at 38 seconds, it is still not clear that the pressure inside the payload is equal to the external pressure. The high voltage protective circuitry is such that if any part of the high voltage circuitry arcs, the high voltage supply is instantly shut off. For four seconds, R-C time constant circuitry controls the power supply such that turning on is a slow process (4 seconds after shut down) providing additional time for the payload pressure to decrease.

The scale compression amplifier of Figure 51 is accurate to 1% with supply voltage variations of $\pm 5v$, a most unlikely occurrence on the rocket. The data of Figure 52 is based upon data obtained by the Bendix Corporation [51]. The curve was checked at count rates of $10^4/\text{sec}$ and $10^5/\text{sec}$. The resulting output voltage was 1.04, compared to 1.06 as read from the curve @ $10^4/\text{sec}$; with 1.60 and 1.61 respectively @ $10^5/\text{sec}$

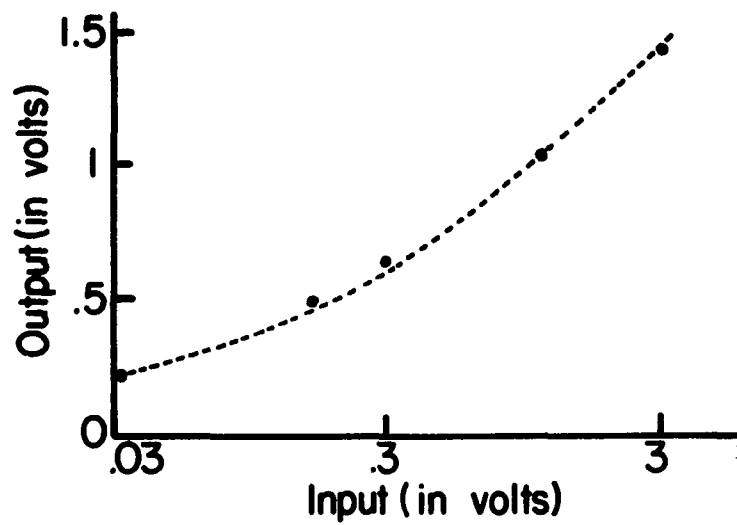


FIG. 51--SCALE COMPRESSION AMPLIFIER

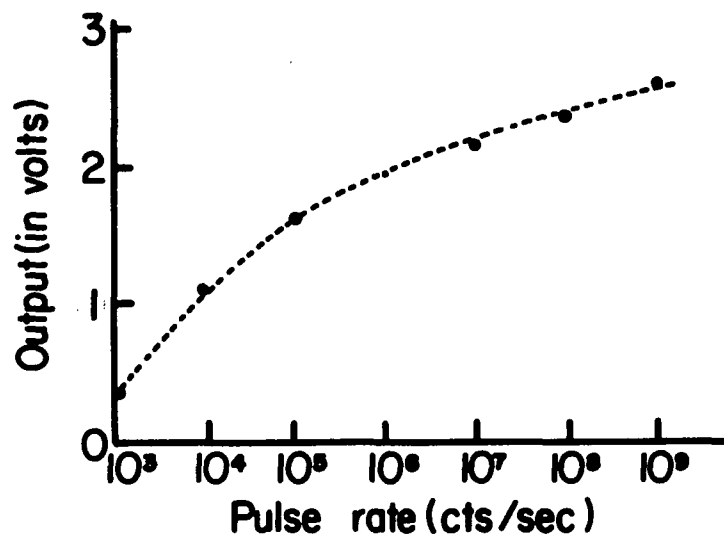


FIG. 52--PULSE RATE VS TELEMETRY AMP OUTPUT

and 0.42 and 0.41 respectively @ 10^3 /sec after the high voltage to the channeltron was adjusted to 3150 volts.

4. Calibration

The calibration required of the detector for full utilization of its energy resolution and absolute flux determination capability is, of course, exposure of each bin to a plane wave monochromatic source of varying strength throughout the ultra-soft x-ray range. Also, an angular response of each bin might be taken since the exact effect of the collimator might be interesting, although the angular properties of photocathodes are well known. It was not possible to secure such a source before the rocket flight, consequently an attempt was made at determining upper limits on the errors in calibration to see if the detector's usefulness would be nullified.

To determine a limit on the accuracy of the calibration of each bin (absorber-photocathode), the following points should be considered.

(a) The average thickness error of the absorbers is known to be less than ten percent at 500Å and five percent at 3500Å.

(b) The different photocathodes' efficiencies were measured at 2Å, 8.3Å, and 44Å. Since the curves agree with the experimental data of Lukirskii [37], extrapolation to 100Å by use of Lukirskii's data does not seem unreasonable. An error of ten percent seems reasonable to take account for the extrapolation.

(c) The efficiency of electron collection with the detector. This error should affect the absolute calibration almost equally over wavelength. When the efficiency measurements were made on the photocathode it appeared that the electron collection efficiency did not vary much with wavelength because the results were the same as Lukirskii's efficiency. This weak wavelength dependence is plausible because of the large potentials used to accelerate and focus the secondary electrons; large potential meaning that the energy gained from the potential by the emitted secondary electron is much greater than its initial energy. The initial secondary electron energy depends weakly upon wavelength of the x-ray in the ultra-soft x-ray range.

An experiment in the lab was undertaken to obtain the electron collection efficiency of each bin. Each bin was placed in a bell jar with an Fe^{55} source (^{55}Fe) 1.5 feet away; and the reading was compared with that of a single piece of calibrated photocathode with its own electron collector. (Viewing the same source at the same distance.) The physical collecting area of the detector was measured as 30 cm^2 ; and the measured efficiency of the bins averaged about 0.7 that of the single piece of photocathode. Being certain that all the ejected electrons were collected from the single photocathode (plateau having been reached), one can assume that 0.7 of the ejected secondary electron splashes were being collected from the bin, (i.e, the effective physical area was about 20 cm^2). The error in the electron collection efficiency was about five percent due to the non-planar source of x-rays, with another five percent accounting for variations over x-ray wavelength.

Cross-talk between two adjacent bins was negligible.

Addition of the above errors indicates a maximum error in bin response (calibration) for any of the four bins of about twenty-five percent. The four bin responses are graphed in Figures 53 thru 56, with error bars.

In addition to the calibration errors, the noise in the data must be considered. The noise in the digital mode is a purely statistical counting error. The analog error is statistical in that the analog signal is a fast rise time A-C signal which is averaged over many spins (10-20) of the rocket. Telemetry noise is the limiting factor for the analog mode. It is estimated that the worst case is at an event (secondary electron splash) rate of 10^9 /sec for which a signal voltage error of 0.05 can cause an error in event rate of 10-15 percent (Figure 52).

The significant point to be made is that a simple subtraction of bins will provide low resolution (100%) in the ultra-soft x-ray range with the bin responses and errors seen in Figures 53 thru 56. With this point in mind, a decision was made to fly the x-ray detector, in the hope that this trial run would lead to other flights.

An approximate idea of the sensitivity of the detector to weak x-ray sources should be considered. Grader et al [10], using a neon-methane gas flow proportional counter (70 cm² AREA, 6° FWHM) with an efficiency of about ten percent from 150 ev to 1400 ev, collected 2000 counts from SCO X-1 in 100 seconds of flying a spin stabilized rocket. The 5-150A detector with 20 cm² of active area and about 12% average efficiency in the 150 ev to 1400 ev range (FWHM = 15°) should

there

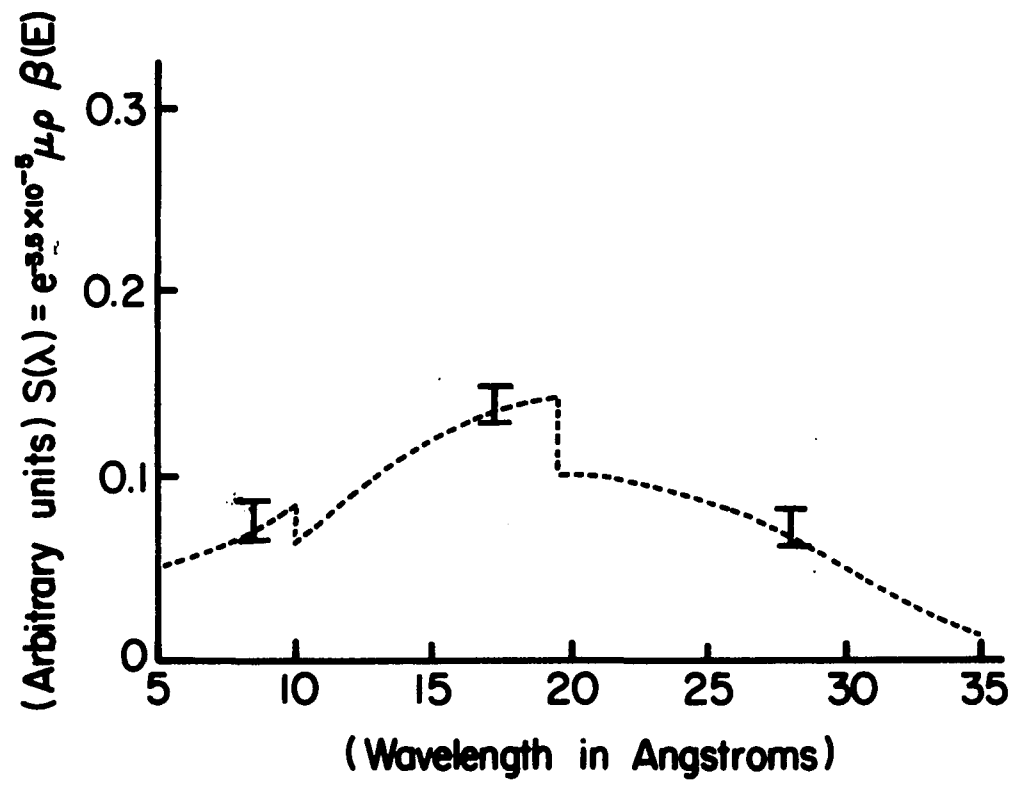


FIG. 53--3500A ALUMINUM BIN

Response (arbitrary units)

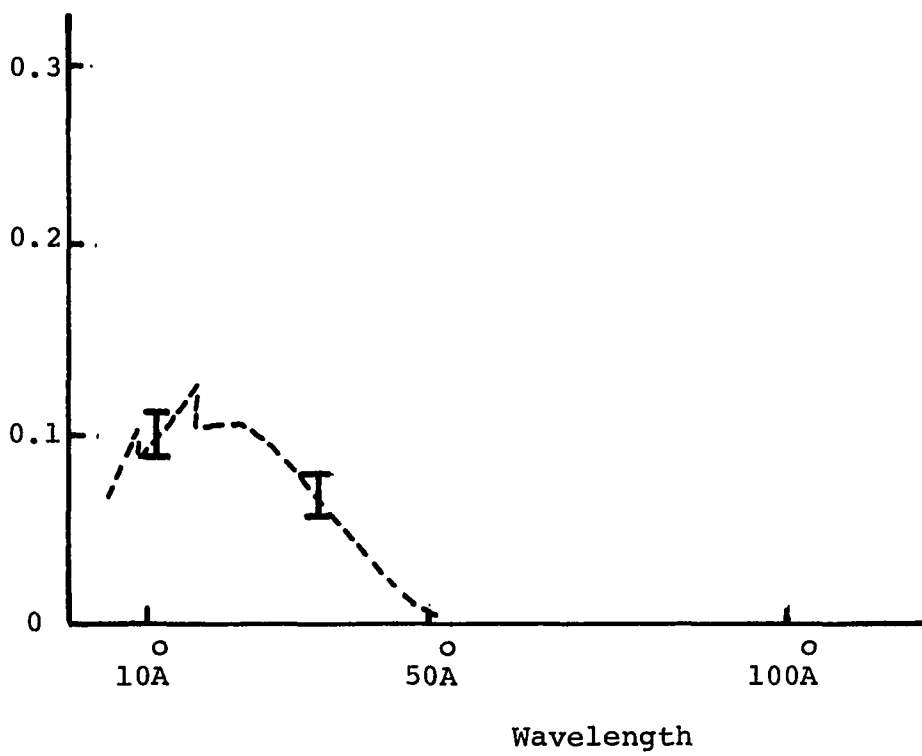


FIGURE 54
2500Å ALUMINUM BIN

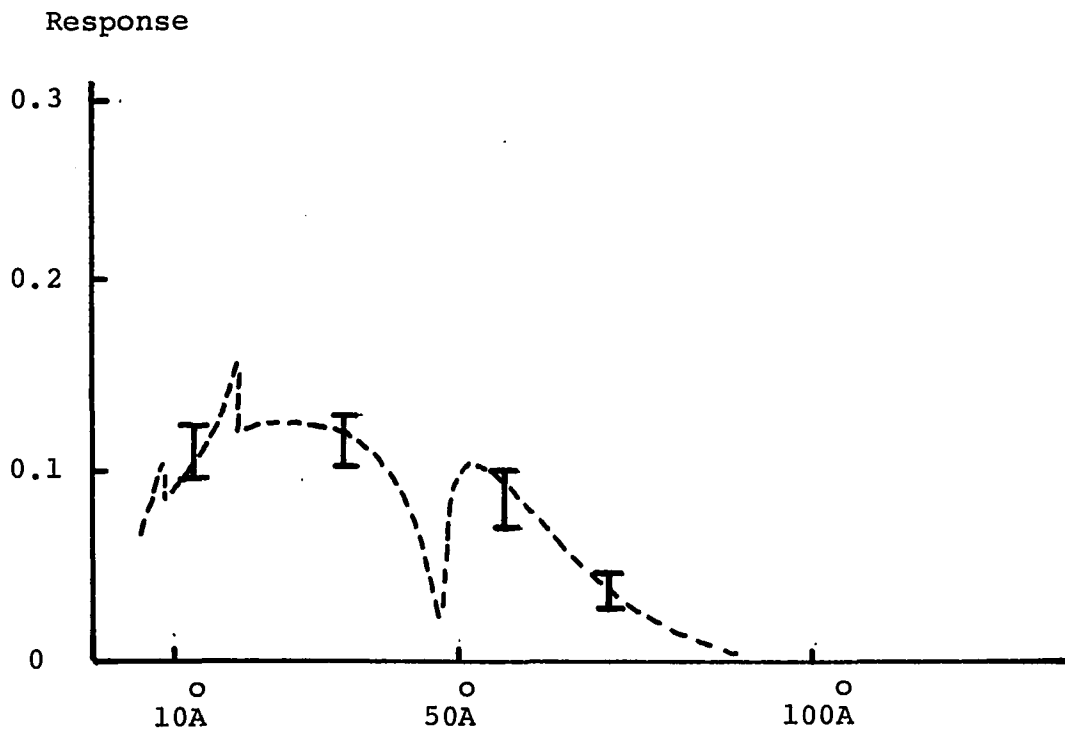


FIGURE 55
1500Å ALUMINUM BIN

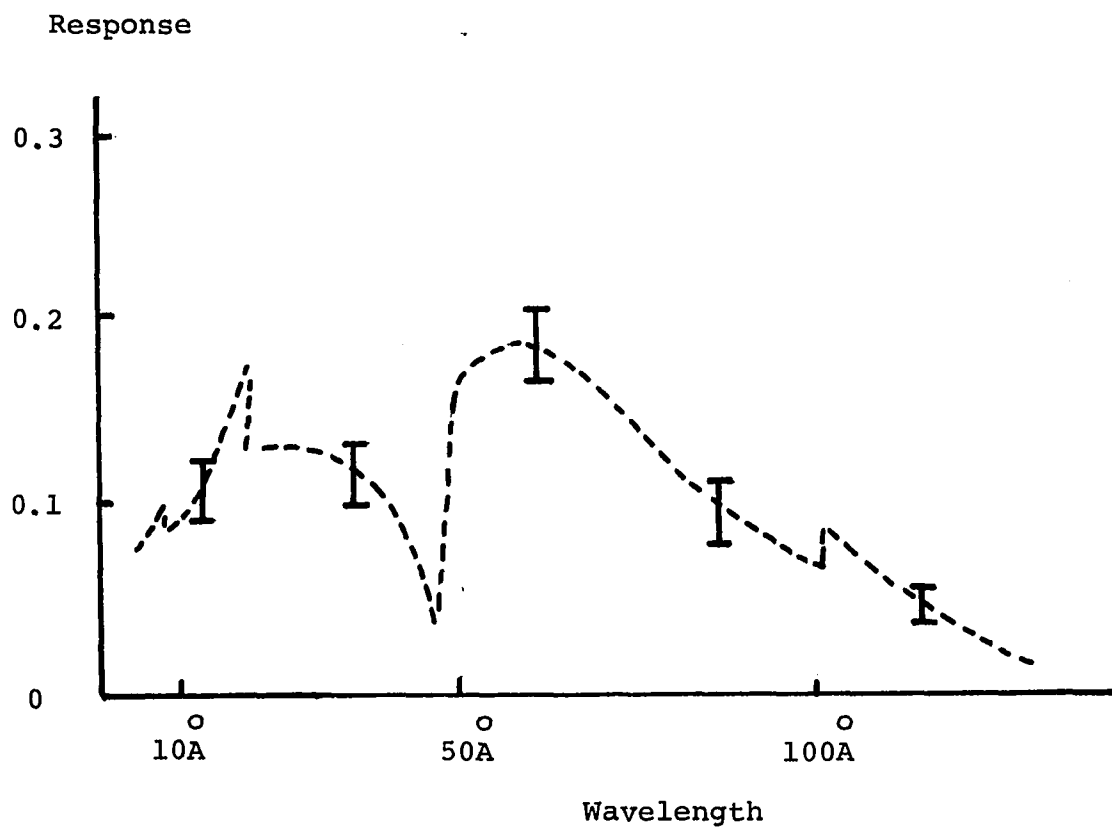


FIGURE 56
500A ALUMINUM BIN

therefore receive about 3400 counts from SCO X-1; that is, the ratio of

$$\begin{array}{ccccccc} \text{(AREA)} & \text{(ANGULAR FWHM)} & \left(\begin{array}{c} \text{Flight} \\ \text{Time} \end{array} \right) & \text{(EFFICIENCY)} & & & \\ = & \frac{20}{70} & \frac{15}{6} & \frac{200}{100} & \frac{12}{10} & = & 1.7 \end{array}$$

Data from the 5-150 $\overset{\circ}{\text{A}}$ detector would be used from the 200 seconds the rocket would spend above 210 km. Background from high energy (10 kev) electrons in the detector was estimated (Arnoldy, private communication) to be less than 30 counts/sec isotropic while cosmic ray background was estimated to be less than 2 counts/sec (Lockwood, private communication). Grader's data indicates that the x-ray background noise should be 300 counts while viewing SCO X-1.

The x-ray airglow [13] in the ionosphere caused by the sun flux less than 30 $\overset{\circ}{\text{A}}$ wavelength was estimated to be 80 cts/sec isotropic for the case of the 5-150 $\overset{\circ}{\text{A}}$ x-ray detector skimming the horizon at 210 km (the beginning of data collection). Data was to be taken for 200 sec with a maximum height of 270 km being achieved. The airglow, composed of nitrogen and oxygen fluorescence x-rays, should decrease as the height increases. A good approximation of the airglow count rate vs. height above 210 km should be possible by using the atmospheric transmission tables of Henke [34]. Although all x-rays less than 31 $\overset{\circ}{\text{A}}$ (nitrogen k edge) contribute to the airglow, using the 31 $\overset{\circ}{\text{A}}$ absorption (1 - transmission) only should give an upper limit to the airglow count rate as a function of height.

The airglow rate as a function of altitude ($h > 210$ km) is

$$\text{AGR} = 80 [1 - T(h)]/[1 - T(210)]$$

where $T(h)$ is the transmission of 31A° x-rays.

The number of spurious counts from the airglow, the electrons, and the cosmic rays while the detector is viewing SCO X-1 (or any point source) is determined by integrating the spurious count rate as a function of time where the altitude is a function of time. The result of this integration is multiplied by an angular factor which is the fraction of the total time (200 sec) in which SCO X-1 is viewed. In the $5-150\text{A}^{\circ}$ detector, the angular factor is $15^{\circ}/360^{\circ}$ since SCO X-1 is viewed 15° out of every revolution of the rocket.

The total number of spurious counts is

$$\text{SC} = \frac{15}{360} \int_0^{200} dt \left(80 \frac{[1 - T(h[t])]}{[1 - T(210)]} + 30 + 2 \right)$$

Using trajectory data for $h(t)$ and the Henke tables for $T(h)$, and integrating numerically

$$\text{SC} = \frac{15}{360} (3200 + 6000 + 400) = 350$$

Thus, a conservative estimate of the signal-to-noise ratio for SCO X-1 is $\frac{3400}{550} = 6.2$.

CHAPTER V

SOUNDING ROCKET FLIGHT

1. Objective

The overall purpose of the rocket flight was (1) the simultaneous measurement of the electron density, the solar u-v flux, and x-ray flux; all as a function of altitude, in the D and lower E regions (80-110 km) of the ionosphere; and (2) the detection of ultra-soft x-ray objects outside the solar system.

As ionizing radiation from the sun penetrates the atmosphere more free electrons are produced until a maximum production is reached, after which the production rate decreases until finally all of the radiation has been absorbed. The rate of change of electron density is

$$(1) \quad \frac{dN}{dt} = q - L$$

where q is the production and L is the rate of loss. Various models [52-54] of the loss mechanisms, production mechanisms, and number densities of constituents can be used in the above equation. The flux of radiation at height H and wavelength λ is

$$S(H, \lambda) = S_{\infty}(\lambda) e^{-t \sec x}$$

where $S_{\infty}(\lambda)$ is the solar spectrum at the top of the atmosphere and x is the zenith angle of the flux propagation vector. t is the optical depth down to altitude H ;

$$\text{that is, } t = \int_{\infty}^H \sum_{\ell} N_{\ell}(h) \sigma_{\ell}(\lambda) dh$$

where $N_{\ell}(h)$ is the number density of molecules of the ℓ^{th} constituent and $\sigma_{\ell}(\lambda)$ is the molecule's total absorption cross-section. The quantity $\frac{1}{\sec x} \frac{ds}{dH}$ is the absorption/unit Vol.-sec-A. The electron production function is $\frac{1}{\sec x} \frac{ds}{dH}$ with appropriate weighting of the constituents with η_{ℓ} , the ionization efficiency. That is;

$$P_e = S(H, \lambda) \sum_{\ell} N_{\ell}(H) \sigma_{\ell}(\lambda) \eta_{\ell}(\lambda)$$

where P_e is the electron production.

The above expression for the electron production along with experimental values of the electron density and radiation fluxes ($S(H, \lambda)$) can be used in expression (1) to test the plausibility of various models of the ionosphere. For example, using the measured values of x-ray flux as a function of height along with estimates of constituent number densities and cross-sections and recombination coefficients, an electron density profile can be derived which can be compared to the experimental electron density profile data. It was also planned that the x-ray detector would sweep through the galactic center, which at the anticipated 7 EST launch time would be directly south.

2. Payload

The rocket apparatus included: (1) the wide range photon detector (5-150A) with spectral decomposition capability to directly determine the relative importance of different parts of the sun's spectrum in electron production, (2) a Faraday rotation experiment that was set to the optimum frequency for observation of a reversal in the rotation, which would absolutely determine the collision frequency as a function of altitude. (The thesis of L. Larson [12] gives a detailed discussion of all the effects and measurements related to this later technique. Basically, the Faraday rotation experiment consists of a ground based transmitter operating at 1.7 MHz and a receiver in the rocket payload. The transmitter was a Gates HFL-1000 and an exciter, while the antenna was a center fed short dipole 100 feet long with loading coils at the center of each leg) and (3) a photonionization chamber used in the Lyman u-v experiment ~~is~~ also described by L. Larson [12].

3. Results

There were two flights in the series, both spin stabilized Nike-Tomahawk rockets. The first rocket in August 1970 at Wallops Is., which broke apart 19 seconds into the flight, was subsequently determined to have a defect in the structure of the payload. The next year was spend modifying the second payload to prevent a repeat performance. The second rocket was flown in March 1972 at Wallops Is. with 80° effective elevation and 105° azimuth. Although the vehicle was success-

fully launched, at 24 seconds into the flight the telemetry signal began to deteriorate, suddenly, and at 90 seconds the signal became completely useless. Unfortunately, the receiver in the Faraday rotation experiment did not receive the ground transmitted signal. It is speculated that the unusually low temperature at launch time (7 EST) caused the local oscillator to drift, moving the passband of the receiver beyond the transmitter frequency. The receiver still seemed to be working as evidenced by the presence of characteristic receiver noise. The u-v detector and one of the x-ray detector bins were working until the telemetry signal completely disappeared.

Data from the u-v detector and the 5-30A x-ray detector were received up until 90 seconds into the flight. The data from these detectors, shown on the graphs (Figures 57,58) were derived by sampling and averaging the signals in sequential time interval points and estimating the noise voltage. The u-v detector has a broad angular response (45°) while the x-ray detector's output was the fast rise time pulse height associated with the angular response curve, (averaged over 4 sec). Unfortunately, the noise had strong frequency components equal to the frequency associated with the rise time of the signal.

It is meaningful to compare the x-ray data to theoretically derived data, based upon solar flux values above the atmosphere. The data, $D(H)$, can be expressed as an integral of the following form:

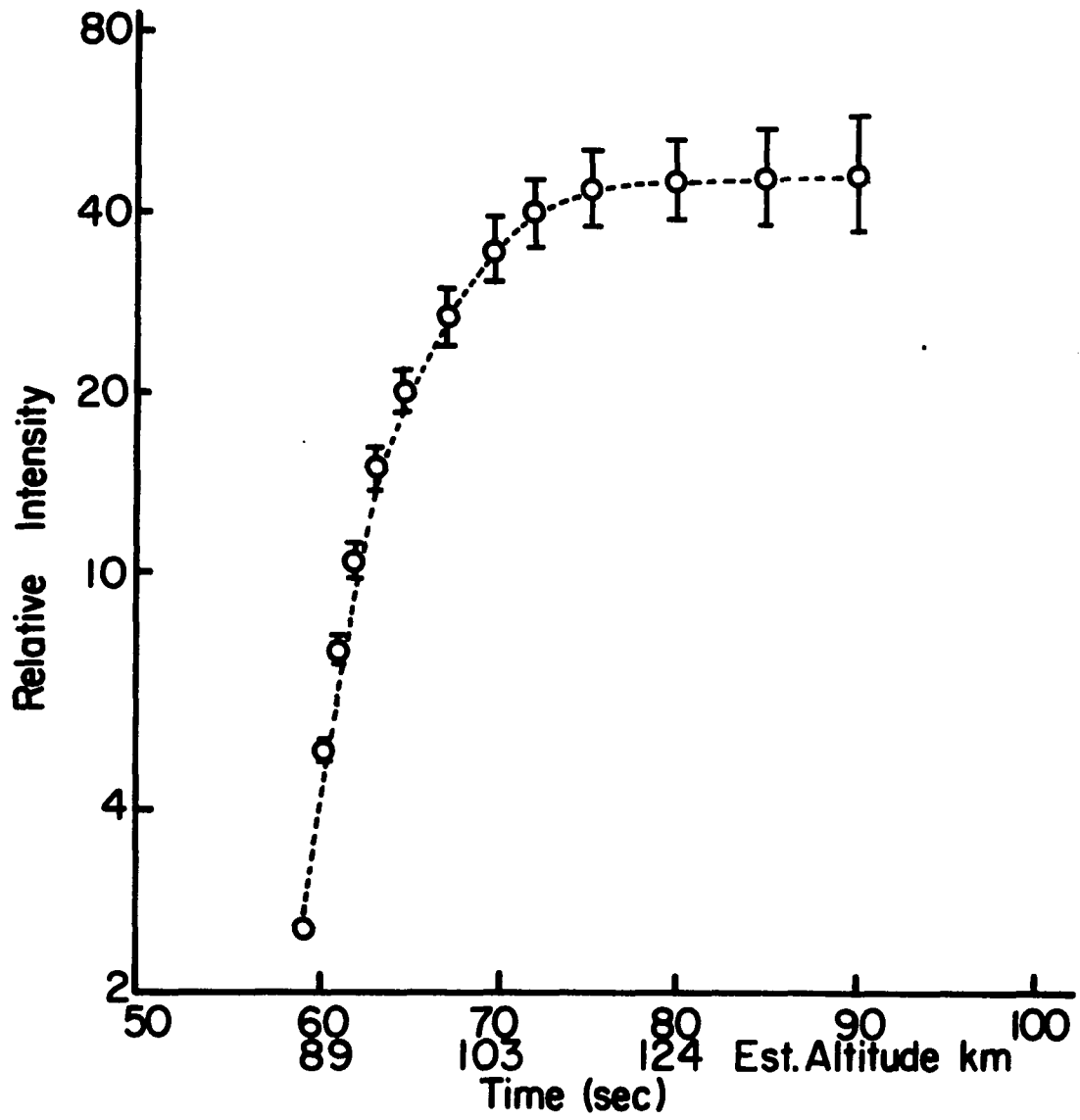


FIG. 57--LYMAN α INTENSITY

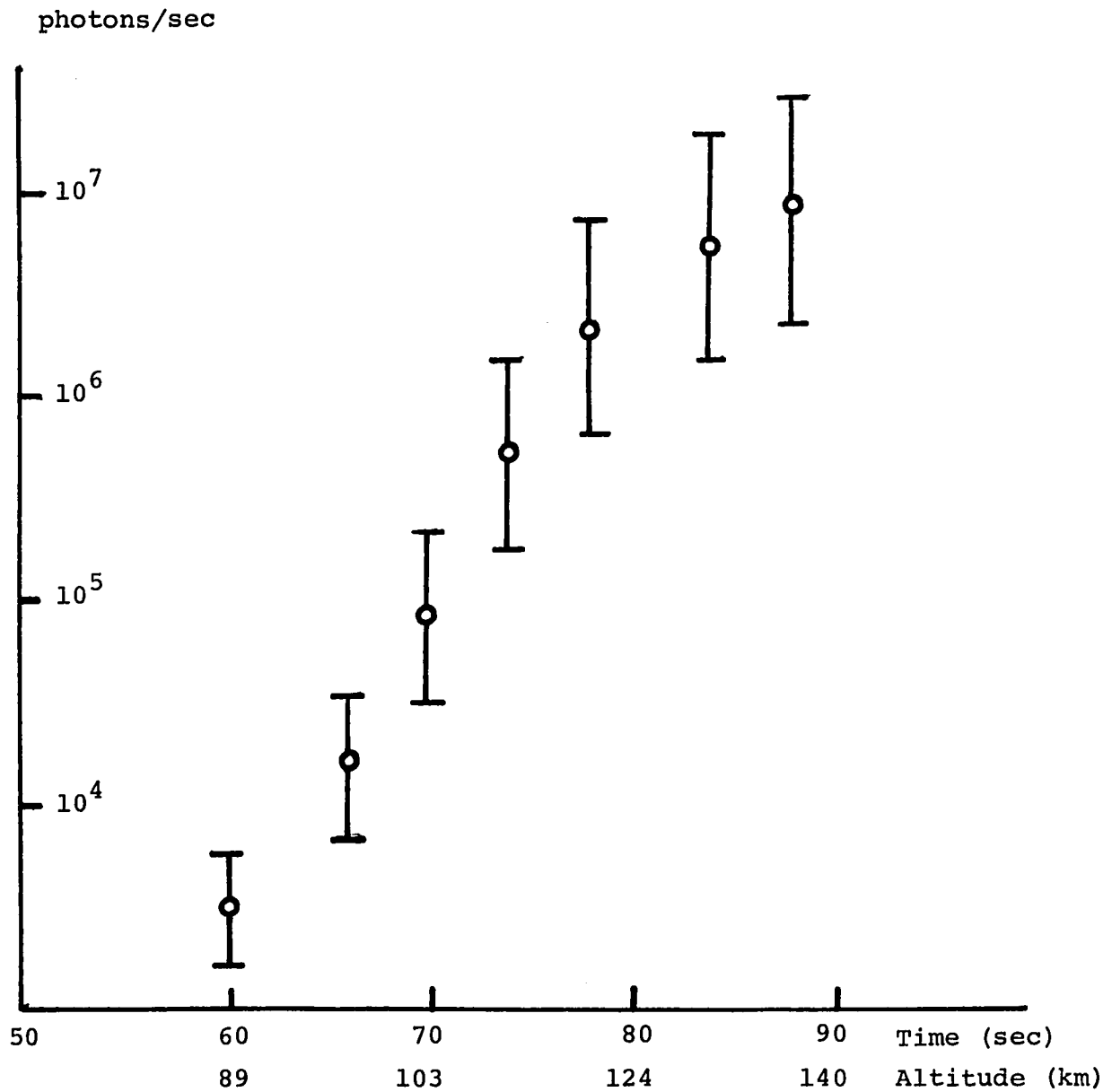


FIGURE 58

5-30 \AA SOLAR X-RAY INTENSITY (Experimental)

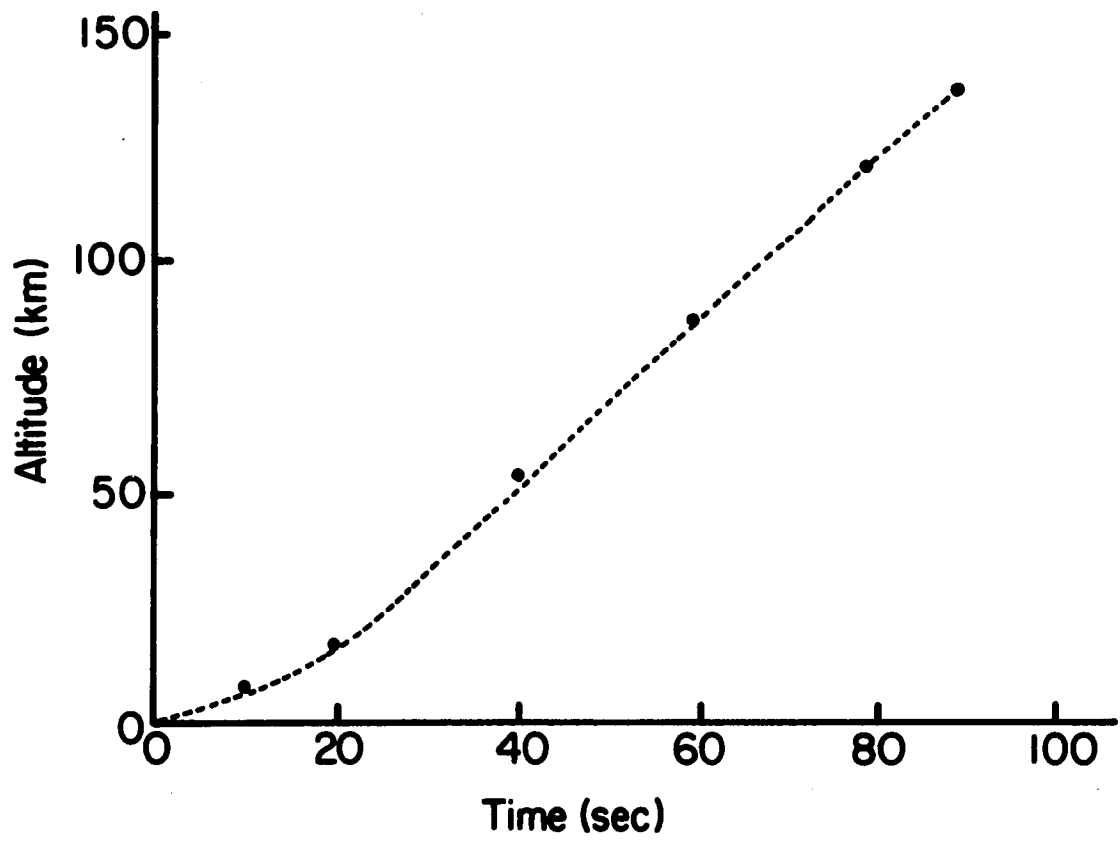


FIG. 59--ROCKET ALTITUDE

$$D(H) = 10 \int_0^{\infty} C(\lambda) S_{\infty}(\lambda) T(\lambda, H) d\lambda$$

where $C(\lambda)$ is the 5-30A.

bin response (Figure 53), $S_{\infty}(\lambda)$ is the solar spectrum at the top of the atmosphere (Figure 60) and $T(\lambda, H)$ is the transmission as a function of height. The theoretical $D(H)$ is shown as a function of height in Figure 61.

The Henke atmospheric transmission tables [34] are valid for normal incidence of the solar flux on the atmosphere.

$$\text{The flux } S(H, \lambda) = S_{\infty} e^{-t \sec x}$$

where t is the optical depth down to altitude H . The above expression is valid for the elevation angle of 15° [12] on the rocket flight.

The Henke transmission tables are valid for $\text{SEC } X = 1$,

$$S = S_{\infty} e^{-t}$$

$$T(\lambda, H) = e^{-t(\lambda) \sec x} = \left(e^{-t(\lambda, H)} \right) \sec x$$

where $e^{-t(\lambda, H)}$ is the Henke transmission table data.

$C(\lambda) S_{\infty}(\lambda) T(\lambda, H)$ for 5 heights was computed and numerically integrated over λ .

$T(25\text{A}, H)$ is plotted in Figure 62. Curves of the absorption function for both the theoretical curve and the experimental curve are pictured in Figure 63. Both curves were obtained by subtraction of flux at the times where the data was averaged about. The curves are the integral over the

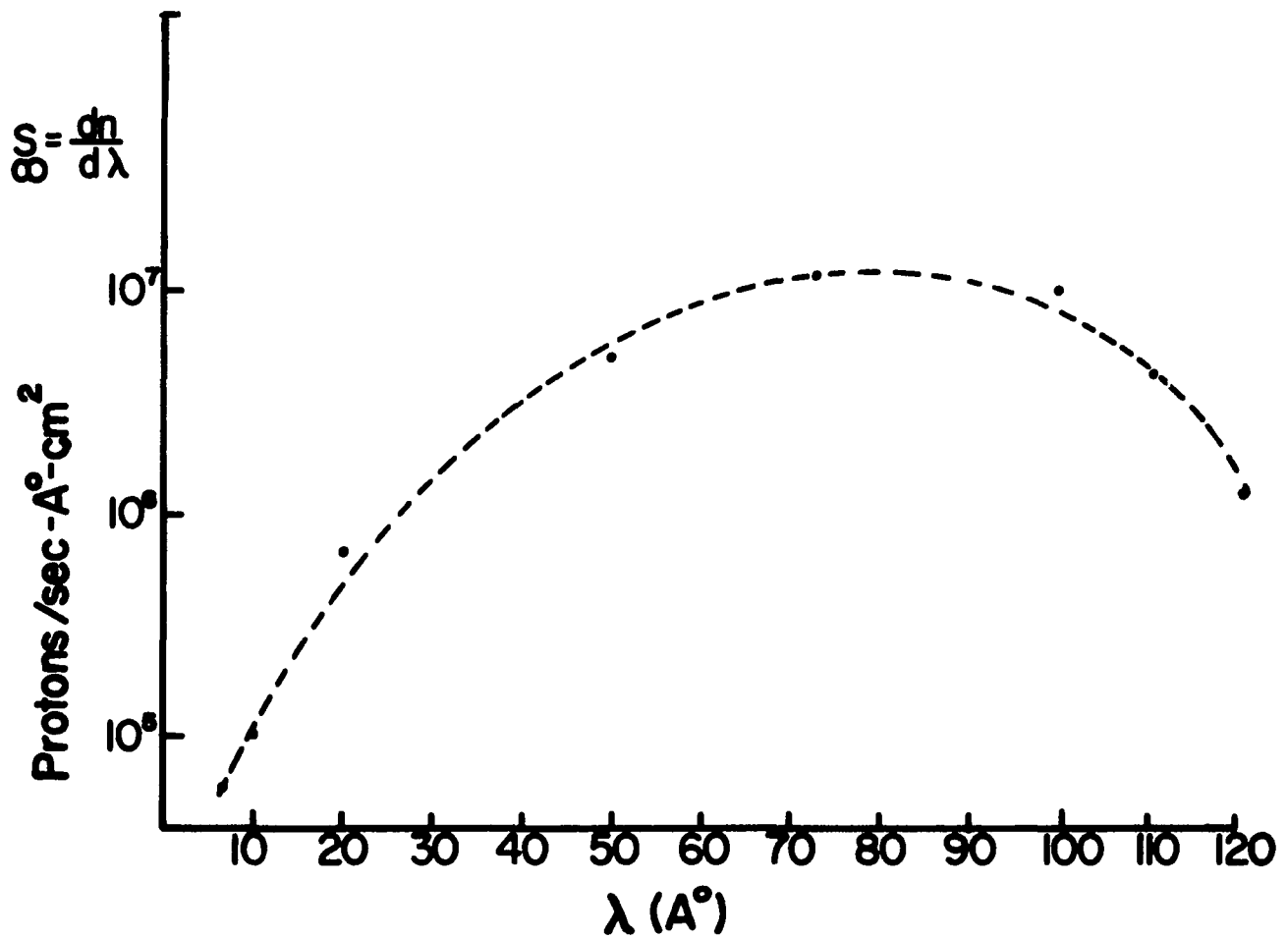
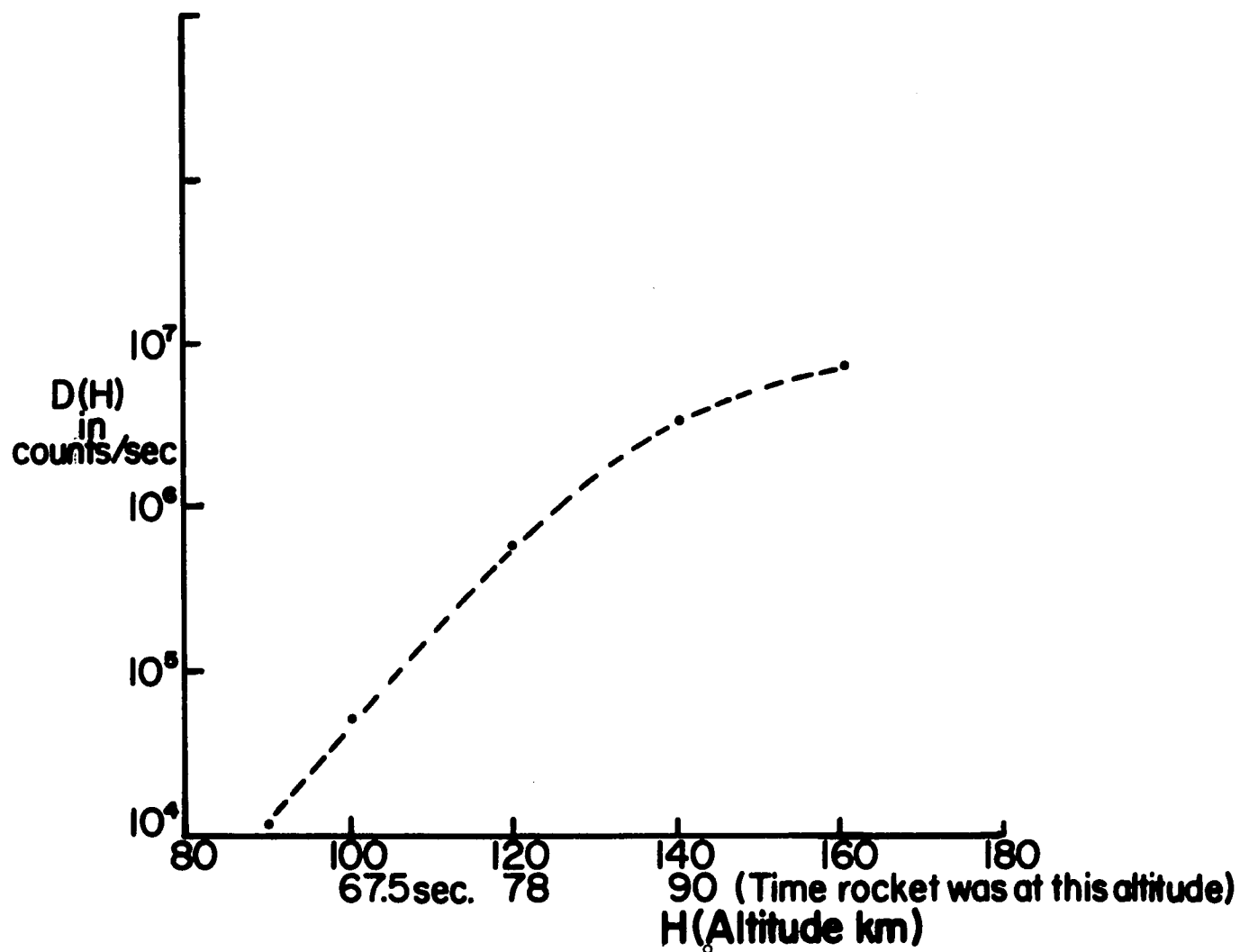


FIG. 60--SOLAR SPECTRUM AT THE TOP OF THE ATMOSPHERE (QUIET SUN)
 from Friedman, "Solar Radiation", 14, 23 Aug., 1962
 (Astronautics)

FIG. 61-- $D(H)$ Vs. ALTITUDE (5 - 30Å)

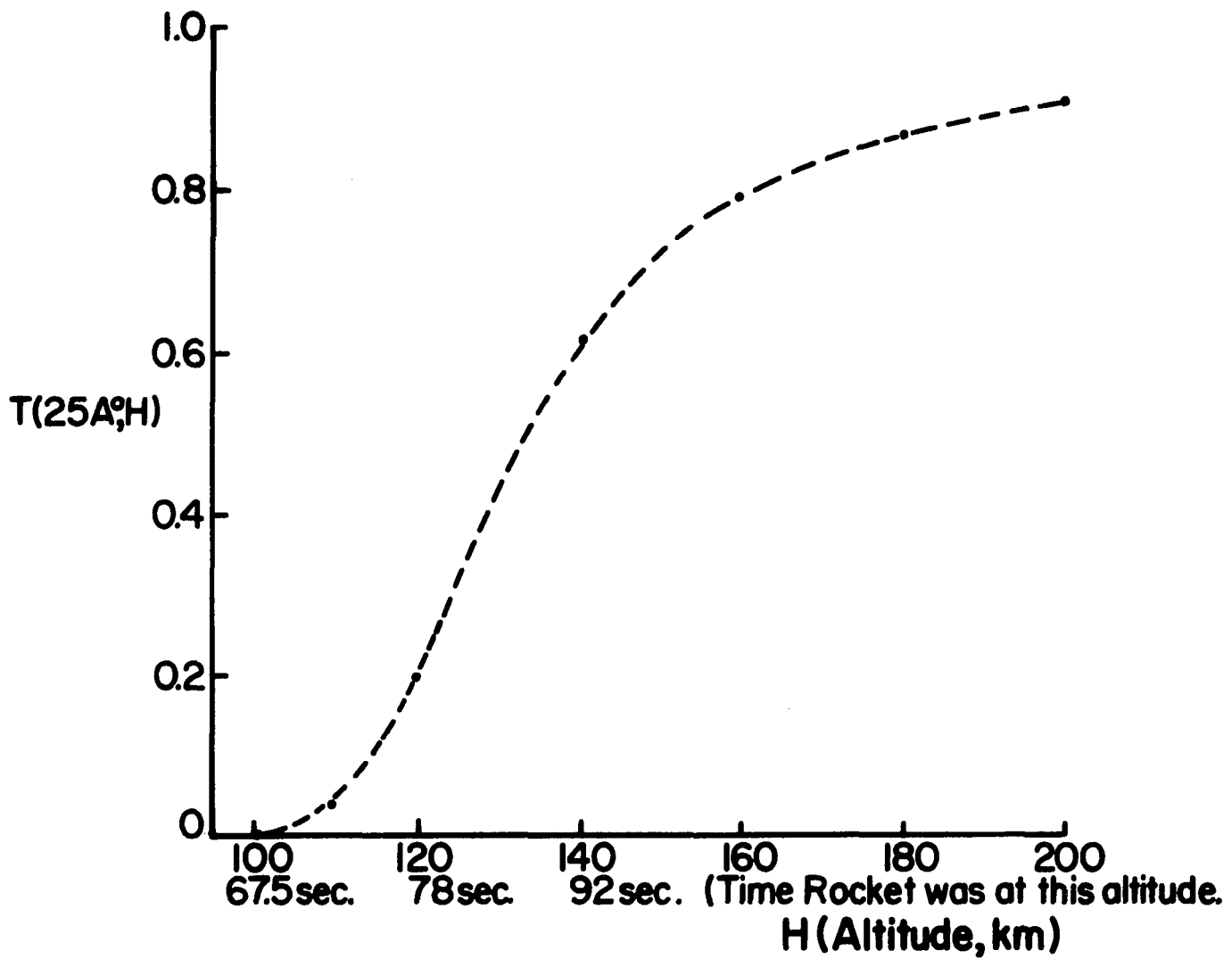


FIG. 62--TRANSMISSION OF 25A X-RAYS AS A FUNCTION OF ALTITUDE

From Experimental Data (Fig. 58) ○

From Theoretical Curve (Fig. 61) ▲

(Absorption) x4
photons/sec-cm³

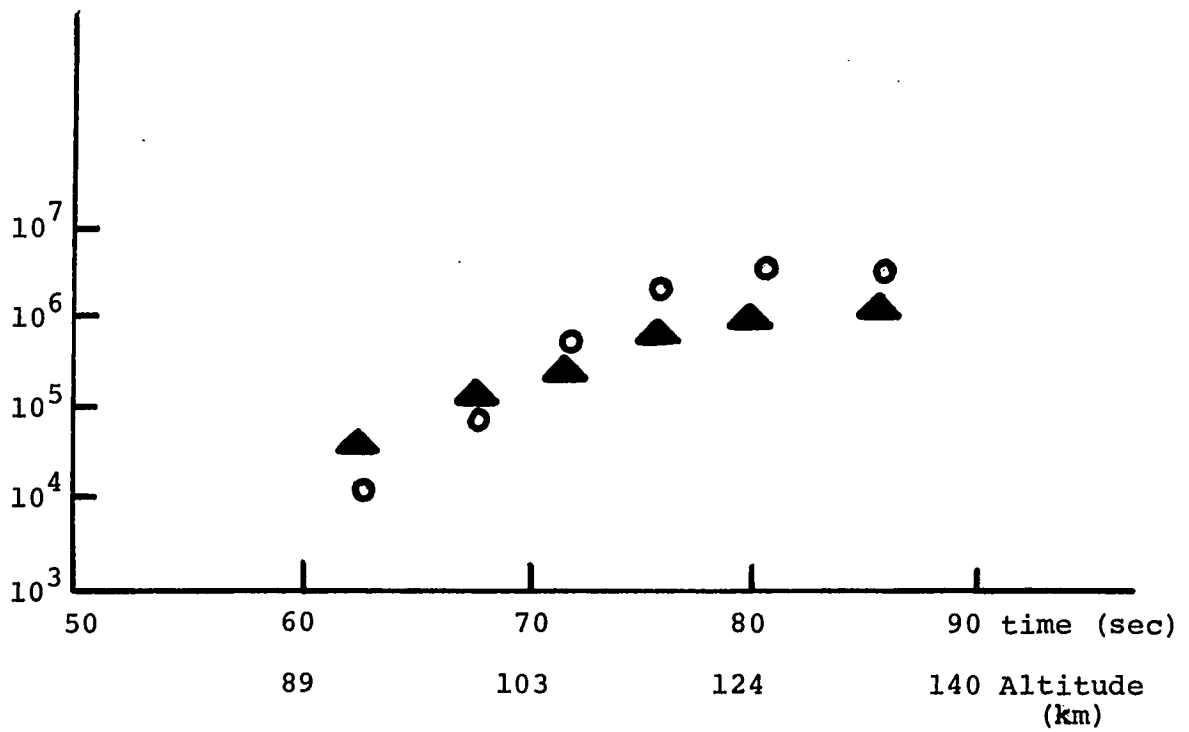


FIGURE 63
THEORETICAL AND EXPERIMENTAL 5-30A X-RAY
ABSORPTION CURVES

wavelength range 5-30Å (weighted by the 5-30Å bin response) of the absorption function. If the absorbing molecules are also the ionized component of the atmosphere, the absorption curve is proportional to the electron production. Inspection of the theoretical and experimental absorption curves indicates poor agreement of the absolute production (cross-over point of the two curves is at 10^5 ph/sec-cm², 69 sec). The experimental curve peaks higher, but begins lower than the theoretical curve. The maximum absorption occurs at the same height for both the theoretical and experimental curves, but the significance of the disagreement is indeterminant since the x-ray data itself is more than mildly open to question as a result of the poor rocket flight.

CHAPTER VI

CONCLUSIONS

The project of designing an x-ray detector for the ionospheric experiment has spawned innovations in photon detection in the ultra-soft x-ray range and a new approach to the spectral decomposition (unfolding) of data. The sounding rocket flight of the x-ray detector, from which data consistent with telemetry performance was received, indicates that the detector design is basically sound and applicable to future sounding rocket and satellite flights where u-v free data and spectral information from radiation in the difficult $10-500\overset{\circ}{\text{A}}$ wavelength range is desired. The detector's method of spectral decomposition was successfully tested on the ground, albeit in a higher energy range due to the lack of adequate ultra-soft x-ray sources.

The scheme of data unfolding, which really means the extraction of all the spectral information possible consistent with the accuracy of the data, should have wide applicability. In unfolding the x-ray detector data, the specific case of an exponential detector response (kernel) was studied, but it should be possible to unfold the data from most detectors by careful consideration of the response of the particular detector and subsequent use of the various techniques of modified kernel synthesis described in Chapter II.

BIBLIOGRAPHY

1. E. T. Byram, T. A. Chubb, and H. Friedman, Jour. Geophys. Res., 61, 251 (1956).
2. H. Friedman, "Reports on Progress in Physics", 25, pp. 163-217 (1962).
3. H. Friedman, "Research in Geophysics", 1, pp. 197-241 (1964).
4. H. E. Hinteregger, K. R. Damon, L. Heroux, and L. A. Hall, "Space Research", Ed. H. Kallmann-Byl (1960).
5. H. E. Hinteregger, Jour. Geophys. Res., 66, 2367 (1961).
6. J. F. Drake, J. Gibson, and J. A. Van Allen, "Iowa Catalogue of Solar X-Ray Flux (2-12A)", University of Iowa Research Report, 69-36 (1969).
7. P. R. Sengupta, "Effect of $1 \text{ } 10^{\circ} \text{ \AA}$ Solar X-Rays on the Ionosphere Between 60 and 100 km.", University of Iowa Research Report 68-17 (1968).
8. P. R. Sengupta, "Solar X-Ray Control of the E-Layer of the Ionosphere", University of Iowa Research Report 69-3 (1969).
9. C. M. Cornell, R. J. Grader, J. G. Harri, R. W. Hill, R. P. Ramble, and D. S. Salmi, Rev. Sci. Inst., 39, 951 (1968).
10. R. J. Grader, R. W. Hill, F. D. Seward, and W. A. Hiltner, Astrophys. Jour., 159, 201 (1970).
11. D. W. Aitken, IEEE Transactions on Nuclear Science NS-15, 10 (1968).
12. L. Larson, Ph.D. Thesis, University of New Hampshire, Durham (1967).
13. R. J. Grader, and R. W. Hill, J. G. R., 73, 7149 (1968).
14. A Compton and S. Allison, X-Rays in Theory and Experiment, Van Nostrand, New York, 1935.

15. P. Morse, and H. Feshbach, Meth. of Theoretical Physics, 925-945, McGraw-Hill, Inc., New York (1953).
16. N. H. Marshall, A.E.C. Report No. IDO-17175, May 1966.
17. C. Eckart, Phys. Rev., 51, 735 (1937).
18. G. Kreisel, Proc. Roy. Soc. (London), 197, 160 (1949).
19. B. Brunfelter, Nucl. Instr. and Meth., 40 (1966), 84.
20. R. Gold, Argonne Nat. Lab. Rept., ANL-6984, 1965.
21. R. G. Nisle, Nucl. Instr. and Meth., 70, 169, 1969.
22. R. Gold, Journal of Computational Physics, 3, pp. 167-175, 1968.
23. I. K. Abu-Shumays, Journal of Computational Physics, 7, pp. 219-238 (1971).
24. M. S. Lynn, W. P. Timlake, Numerische Mathematik, 11, pp. 77-98 (1968).
25. V. A. Morozov, Zh. Vychisl. Mat. Mat. Fiz., 6, 1, 170-175, 1966.
26. D. L. Phillips, J.A.C.M., Vol. 9, #1, pp. 84-96 (1962).
27. I. K. Abu-Shumays, Argonne Nat. Lab. Rept., ANL-7615, pp. 87-95, 1968-1969.
28. A. J. Viterbi, Principles of Coherent Communication, McGraw-Hill, New York (1966).
29. D. Sakrison, Communication Theory, John Wiley & Sons, New York (1968).
30. M. Schwartz, Information Transmission, Modulation, and Noise, McGraw-Hill, New York (1959).
31. L. Enochson, Programming and Analysis for Digital Time Series Data, Shock and Vibration Information Center, N.R.L. (1968).

32. S. I. Gass, Linear Programming, McGraw-Hill, New York (1969).
33. R. Fletcher and M. Powell, British Computer Journal, Vol. 6, pp. 163-8, 1963.
34. B. L. Henke, Norelco Reporter, XIV, 117 (1967).
35. A. P. Lukirskii, USSR Acad. Sci. Bul., 28, 774 (1964).
36. A. P. Lukirskii, and E. P. Savinov, Optics and Spectroscopy, 23, 163 (1967).
37. A. P. Lukirskii, O. A. Ershov, T. M. Zimkina, and E. P. Savinov, Soviet Physics - Solid State, 8, 6, 1422-4 (1966).
38. A. P. Lukirskii, and M. A. Rumsh, Optics and Spectroscopy, 9, 265-7 (1960).
39. A. P. Lukirskii, and O. A. Ershov, Soviet Physics - Doklady, 135, 1, 1231-3 (1960).
40. E. P. Savinov, and A. P. Lukirskii, Soviet Physics - Solid State, 6, 11, 2624-30 (1965).
41. A. P. Lukirskii, and E. P. Savinov, Optics and Spectroscopy, 16, 168 (1964).
42. L. Heroux, and J. E. Mansun, J. Opt. Soc. Amer., 55, 1, 103-4 (1965).
43. T. Somer, and P. Graves, IEEE Trans., 376, June (1968).
44. L. G. Parratt, Phys. Rev., 95, 359 (1954).
45. V. A. Blank, and O. M. Sorokin, Soviet Physics - Solid State, 12, 7, 1536 (1971).
46. D. G. Smith, and K. A. Pounds, IEEE Trans., 541, June (1968).
47. V. A. Fomichev, Optics and Spectroscopy, 22, 432 (1967).
48. J. Samson, Applied Optics, 4, 915 (1965).
49. M. V. Reinhardt, Applied Optics, 8, 617 (1969)

50. J. Adams, and B. W. Manley, IEEE Trans., 88, June (1968).
51. A. C. Schmidt, Bendix Tech. Appl. 9803, April (1969).
52. Van Zandt and Knecht, "The Structure and Physics of the Upper Atmosphere", Space Physics, John Wiley & Sons, 1964.
53. Nawrocki, Atmospheric Processes, G.C.A., Bedford, Mass., AFCRL-595, G.C.A. #61-37-A (1961).
54. J. A. Ratcliffe, The Ionosphere, CH9, Academic Press (1960).
55. M. Abramowitz, and I. A. Stegun, (Editors), Handbook of Mathematical Functions with Formulas, Graphs, and Mathematical Tables, U. S. Govt. Print. Off., Washington (1964).

APPENDIX A

CALCULATION OF THE TRANSMISSION COEFFICIENT

$$T = (1-R) |e^{i\mathbf{k}\cdot\mathbf{r}}|^2$$

$$|e^{i\mathbf{k}\cdot\mathbf{r}}| = e^{i(-[\mathbf{k}\cdot\mathbf{r}]^* + \mathbf{k}\cdot\mathbf{r})}$$

$$|e^{i\mathbf{k}\cdot\mathbf{r}}| = e^{-2\text{Im}(\mathbf{k}\cdot\mathbf{r})}$$

$$\mathbf{k}\cdot\mathbf{r} = k_0 (N_T \cos\theta'' x + N_T \sin\theta'' y)$$

$$\mathbf{k}\cdot\mathbf{r} = k_0 (N_T \sqrt{1 - \sin^2\theta''} x + \sin\theta'' y)$$

$$\text{Im}(\mathbf{k}\cdot\mathbf{r}) = k_0 \text{Im} \sqrt{N_T^2 - \sin^2\theta''} x$$

For $\theta = \theta'$ (large angles of grazing incidence)

$$N \cong 1 + i\beta$$

$$\text{Im}(\mathbf{k}\cdot\mathbf{r}) = k_0 \text{Im} \sqrt{1 + 2i\beta - \sin^2\theta''} x$$

$$\sqrt{1 + 2i\beta - \sin^2\theta''} = \sqrt{\cos^2\theta'' + 2i\beta} = \cos^2\theta'' \sqrt{1 + 2i\beta/\cos^2\theta''}$$

But

$$\cos \theta_i \sqrt{1 + 2i\beta / \cos^2 \theta_i} \cong \cos \theta_i \left(1 + \frac{i\beta}{\cos^2 \theta_i} \right)$$

$$\text{Im}(\underline{k} \cdot \underline{r}) = k_0 \text{Im} \cos \theta_i \left(1 + \frac{i\beta}{\cos^2 \theta_i} \right) x$$

$$\text{Im}(\underline{k} \cdot \underline{r}) = k_0 x \beta / \cos \theta_i$$

$$T = (1-R) e^{-2\beta x / \cos \theta_i} = (1-R) e^{-\mu x / \sin \theta_i}$$

APPENDIX B

FREDHOLM DIRECT SOLUTION

1) General Method. If the kernel can be transformed into a displacement kernel, then one can use Fourier transform methods to arrive at a solution. If the kernel is of the form $B(T, E)$, then a suitable transformation is $T = e^{T'}$, $E = e^{-E'}$

so that $B(T, E) = B(e^{T'-E'}) = K(T'-E')$

and the limits change to $(-\infty, +\infty)$

Also,

$$I(E) = I(e^{-E'}) \quad , \quad dE = -dE' e^{-E'}$$

One can define a new spectral density and static response

$$F(E') = \beta(e^{-E'})$$

$$C(E') = I(e^{-E'}) e^{-E'}$$

or

$$I(E) = \frac{C(1/E)}{E} \quad , \quad D(e^{T'}) \equiv d(T') = \int_{-\infty}^{\infty} K(T'-E') C(E') F(E') dE'$$

Taking the Fourier transform of both sides

$$\mathcal{F}d = \mathcal{F}K \mathcal{F}C \quad \mathcal{F}$$

and

$$C = \frac{1}{\mathcal{F}} \mathcal{F}^{-1} \frac{\mathcal{F}d}{\mathcal{F}K}$$

2) Detailed Solution. The integral equation is

$$D(T) = \int_0^{\infty} e^{-\mu \rho T} I(\mu) \beta(\mu) d\mu$$

It is expedient to use the variable μ rather than the energy, and define a new spectral intensity $I(\mu)$ which can be transformed into the spectral intensity as a function of energy or wavelength. $\beta(\mu)$ is the static detector response.

$$\mu = \mu(E) \quad d\mu = \mu'(E) dE$$

$$D(T) = \int_0^{\infty} e^{-\mu(E) T \rho} I(\mu) \mu' \beta(\mu) dE$$

Making the transformation

$$T = e^{T'}, \quad \rho \mu = e^{-\mu'}$$

$$D(e^{T'}) = d(T') = \int_{-\infty}^{\infty} e^{-e^{-\mu'}} I(e^{-\mu'}) e^{-\mu'} \beta(e^{-\mu'}) d\mu'$$

$$d(T') = \int_{-\infty}^{\infty} e^{-e^{-\mu'}} F(\mu') C(\mu') d\mu'$$

where

$$F(\mu') = \beta(e^{-\mu'}) \text{ AND } C(\mu') = I(e^{-\mu'}) e^{-\mu'}$$

$$C(t) = \frac{1}{F} \mathcal{F}^{-1} \frac{\mathcal{F} d(t)}{\mathcal{F} e^{-e^t}}$$

where $C(t)$ represents the solution to the unfolded spectrum.
The Fourier transform of e^{-e^t} can be obtained.

$$\mathcal{F} e^{-e^t} = \int_{-\infty}^{\infty} e^{-e^t} e^{-2\pi i \omega t} dt$$

$$\begin{aligned} \text{Let } y &= e^t \\ dy &= e^t dt \\ dt &= dy/y \end{aligned}$$

and

$$\mathcal{F} e^{-e^t} = \int_0^{\infty} e^{-y} y^{-2\pi i \omega - 1} dy$$

$$\mathcal{F} e^{-e^t} = \Gamma(-2\pi i \omega)$$

$$\text{Let } Z = -2\pi i \omega$$

It appears that if $1/\Gamma(z)$ can be expanded in a Taylor series, a workable solution to the integral equation exists.

$$\frac{1}{r(z)} = \sum_1^{\infty} b_l z^l$$

then

$$c(t) = \frac{1}{F} \mathcal{F}^{-1}(\mathcal{F}d(t)) \sum_{l=1}^{\infty} b_l z^l$$

$$c(t) = \sum_{l=1}^{\infty} \frac{b_l}{F} \mathcal{F}^{-1}(z^l \mathcal{F}d(t))$$

But

$$\frac{d^N}{dt^N} \mathcal{F}^{-1} \rho(\omega) = \mathcal{F}^{-1} (2\pi i \omega)^N \rho(\omega)$$

Let

$$\mathcal{F}d(t) = \rho(\omega)$$

then

$$c(t) = \frac{1}{F} \sum_1^{\infty} b_l \mathcal{F}^{-1} (-2\pi i \omega)^l \rho(\omega)$$

1)

$$c(t) = \frac{1}{F} \sum_{l=1}^{\infty} b_l (-1)^l \frac{d^l}{dt^l} \mathcal{F}^{-1} \rho(\omega)$$

But

$$\mathcal{F}^{-1} \rho(\omega) = \mathcal{F}^{-1} \mathcal{F}d(t) = d(t)$$

$$c(t) = \frac{1}{F} \sum_{l=1}^{\infty} b_l (-1)^l \frac{d^l}{dt^l} d(t)$$

Actually, phase information is lost in the step in equation 1). As a result there is a phase factor present in the final result.

$$C(t+\alpha) = \frac{1}{F} \sum_{l=1}^{\infty} b_l (-1)^l \frac{d^l}{dt^l} d(t)$$

It is informative to insert a line source $\delta(\mu'-\mu_0')$ into the integral equation and observe the formation of the solution.

$$d(\tau') = \int_{-\infty}^{\infty} e^{-e^{(\tau'-\mu')}} \delta(\mu'-\mu_0') d\mu'$$

$$d(\tau') = e^{-e^{(\tau'-\mu_0')}}$$

$$C(\tau'+\alpha) = \frac{1}{F} \sum_{l=1}^{\infty} b_l (-1)^l \frac{d^l}{d\tau'^l} e^{-e^{(\tau'-\mu_0')}}$$

In computing the solution it is convenient to work with the variable

$$x = \tau' - \mu_0'$$

$$C(x+\alpha) = \frac{1}{F} \sum_{l=1}^{\infty} b_l (-1)^l \frac{d^l}{dx^l} e^{-e^x}$$

The function $C(\pi+\alpha)$ has been computed for all orders of approximation up to twenty. A recursion relation for the derivatives of e^{-e^x} has been deduced (Appendix I). The derivatives of e^{-e^x} are of the form

$$\frac{d^N}{dx^N} e^{-e^x} = F \sum_{p=1}^N a_p^N y^p$$

where $y = e^x$ and $F = e^{-e^x}$

The coefficients b_l are the coefficients of the expansion of

$$\frac{1}{\Gamma(z)} = \sum_{l=1}^{\infty} b_l z^l$$

The b_l 's are listed in Appendix E. $C(\pi+\alpha)$ for orders 1, 3, and 20 is shown in Figure 1 with $F=1$. Although a narrowing of the response takes place as the order is increased, the side lobes become intolerable. The tendency for the center of the delta function to gravitate toward larger values of x (phase factor) is apparent. Beyond the fourth or fifth order the side lobes are intolerable, and this direct solution of the spectrum must therefore be discarded.

It is of interest that the solution can be interpreted as an operator on the data.

$$\frac{1}{F} P(T, F) D(T) = C(T+\alpha)$$

where

$$P = \sum_{l=1}^{\infty} b_l (-1)^l \frac{d^l}{dT^l}$$

This operator interpretation fits in nicely with the modified kernel theory. It appears that a linearly independent set of functions has been found, and that only alternative weighting is required to reduce or eliminate the side lobes.

$$d(t) = \int_{-\infty}^{\infty} e^{-e^{(T-E)}} c(E) dE$$

$$Pd(t) = \int_{-\infty}^{\infty} \left(\sum_{l=1}^{\infty} b_l (-1)^l \frac{d^l}{dT^l} e^{-e^{(T-E)}} \right) c(E) dE$$

$$K_{\text{MOD}}^{\infty}(T-E) = \sum_{l=1}^{\infty} b_l (-1)^l \frac{d^l}{dT^l} e^{-e^{(T-E)}}$$

is the modified kernel.

APPENDIX C

LAGUERRE SOLUTION

In appendix B it was found that the modified kernel

$$K_{\text{mod}}^N = \sum_{l=1}^N b_l \frac{d^l}{dt^l} e^{-e^{(t-\mu)}}$$

formed a combination of linearly independent functions,

$$\frac{d^l}{dt^l} e^{-e^{(t-\mu)}}$$

The problem is to generate a set of orthogonal functions from these linearly independent functions.

The original equation is

$$D(T) = \int_0^{\infty} e^{-\mu T \rho} I(\mu) \beta(\mu) d\mu$$

T and $\mu\rho$ are then transformed to $e^{T'}$, $e^{\mu'}$ respectively, and the operator

$$\sum_{l=1}^N b_l \frac{d^l}{dT'^l}$$

operates on

$$D(e^{T'})$$

$$D(e^{T'}) \equiv d(T')$$

2)

$$\frac{d^N}{d\chi^N} e^{-e^\chi} = e^{-e^\chi} \sum_{l=1}^N a_l^N (e^\chi)^l$$

$$\rho^N d(T') = \sum_{l=1}^N b_l \frac{d^l}{dT'^l} d(T') = \int_{-\infty}^{\infty} \sum_{l=1}^N b_l \frac{d^l}{dT'^l} e^{-e^{(T'-\mu')}} c(\mu') d\mu'$$

inserting 2)

$$\rho^N d(T') = \int_{-\infty}^{\infty} \left[\sum_{l=1}^N b_l e^{-e^{(T'-\mu')}} \sum_{p=1}^{\infty} a_p^l (e^{T'-\mu'})^p \right] c(\mu') d\mu'$$

transforming back ($T' = \ln T$, $\mu' = -\ln \mu \rho$)

$$\rho^N d(T') \Big|_{T' = \ln T} = \int_0^{\infty} \left[\sum_{l=1}^N b_l e^{-\mu \rho T} \sum_{p=1}^{\infty} a_p^l (\mu T \rho)^p \right] I(\mu) \beta(\mu) d\mu$$

If the function
$$F_l = e^{-x} \sum_{p=1}^{\infty} a_p^l x^p$$

is defined, then the modified kernel

$$K_{mod}^N = \sum_{l=1}^N b_l F_l(x) \quad \text{where} \quad x = \mu T \rho$$

The F_l are clearly linearly independent and related to polynomials with weighting function $x^2 e^{-2x}$ and interval $(0, \infty)$.

The appropriate orthogonal polynomials to transform to are the Laguerre polynomials of order 2. These polynomials have the weighting function $x^2 e^{-x}$ and are defined in the interval $(0, \infty)$. The recursion relation for the Laguerre polynomials is

$$(N+1) L_{N+1}^{(2)}(x) = (2N+3-x) L_N^{(2)}(x) - (N+2) L_{N-1}^{(2)}(x)$$

A set of complete, orthonormal functions can be generated from the Laguerre polynomials for use in synthesizing a delta function. Let $g_N(x)$ be the orthonormal functions.

Since
$$\int_0^{\infty} x^2 e^{-x} [L_N^{(2)}(x)]^2 dx = (N+1)(N+2)$$

define
$$g_N(x) = \frac{x e^{-x/2}}{\sqrt{(N+1)(N+2)}} L_N^{(2)}(x)$$

The task is to convert between the F_L functions and the g_L functions.

$$L_N^{(2)}(x) = \sum_{m=0}^N C_m^N x^m$$

where
$$C_m^N = \frac{(-1)^m}{m!} \binom{N+2}{N-m}$$

then
$$g_N(x) = \frac{x e^{-x/2}}{\sqrt{(N+1)(N+2)}} \sum_{m=0}^N C_m^N x^m$$

Assume $u(x)$ is the desired modified kernel (spectral window). Let $f(x)$ be an arbitrary function;

then
$$f(x) \approx \sum_{l=0}^N a_l g_l(x) = \sum_{l=0}^N a_l \sum_{p=0}^l \frac{x e^{-x/2}}{\sqrt{(l+1)(l+2)}} C_p^l x^p$$

$$f(x) \approx e^{-x/2} \sum_{p=0}^N \left(\sum_{l=p}^N \frac{C_p^l a_l}{\sqrt{(l+1)(l+2)}} \right) x^{p+1}$$

Let

$$f(x) \approx e^{-x/2} \sum_{q=1}^m \left(\sum_{l=q-1}^{m-1} \frac{C_{q-1}^l a_l}{\sqrt{(l+1)(l+2)}} \right) x^q$$

Let

$$f(x) \approx e^{-x/2} \sum_{q=1}^m S_q x^q$$

Let $g(x)$ be an arbitrary function

then
$$g(x) \approx \sum_{l=1}^m b_l F_l(x)$$

but
$$g(x) \approx \sum_{l=1}^m b_l e^{-x} \sum_{q=1}^l a_q^l x^q$$

$$g(x) \approx e^{-x} \sum_{q=1}^m \left(\sum_{l=q}^m b_l a_q^l \right) x^q$$

$$g(x) \approx e^{-x} \sum_{q=1}^m V_q x^q$$

Let $f(2x) = g(x) = u(2x)$

$$f(2x) \approx e^{-x} \sum_{q=1}^m \int_0^1 2^q x^q = e^{-x} \sum_{q=1}^m V_q x^q$$

$$V_q = \int_0^1 2^q$$

$$\sum_{l=q-1}^{m-1} \frac{c_{q-1}^l a_l 2^q}{\sqrt{(l+1)(l+2)}} = \sum_{l=q}^m b_l a_l^l$$

$$a_l = \int_0^{\infty} g_l(x) u(2x) dx$$

and the a_q^l are known

(Appendix I), therefore the b'_l 's can be determined with ease; and

$$K_{mod}^m = \sum_{l=1}^m b'_l F'_l(x)$$

which is an approximation of $u(2x)$. The F'_l 's represent l^{th} derivatives operating on the transformed data.

$$\text{i.e. } \rho^m d(T') = \sum_{l=1}^m b'_l \frac{d^l}{dT'^l} d(T')$$

The next step in the process is to pick an approximation u to expand, remembering that if one wants to center the function about some point "x", one should plug in $2x$ when finding the a'_l 's. The function, $\left(\frac{ex}{a} e^{-x/a}\right)^p$, satisfies all the requirements of a sliding spectral window. By adjustment of "p" the function is capable of being made as narrow as desired, and the point about which the function is centered, a, is easily changed. The derivation of the a'_l 's is taken up on Appendix F. The graph in Figure 64 on the next page is the modified kernel centered about $x=8$ involving ten terms (derivatives) with $p = 40$. The calculations were done using the computer program LAGI. The actual energy resolution depends upon the relation between μ and E . In the soft x-ray band, for example, the relation between μ and E is $\mu = \frac{\rho}{C} E^{-2.8}$ where ρ, C depend

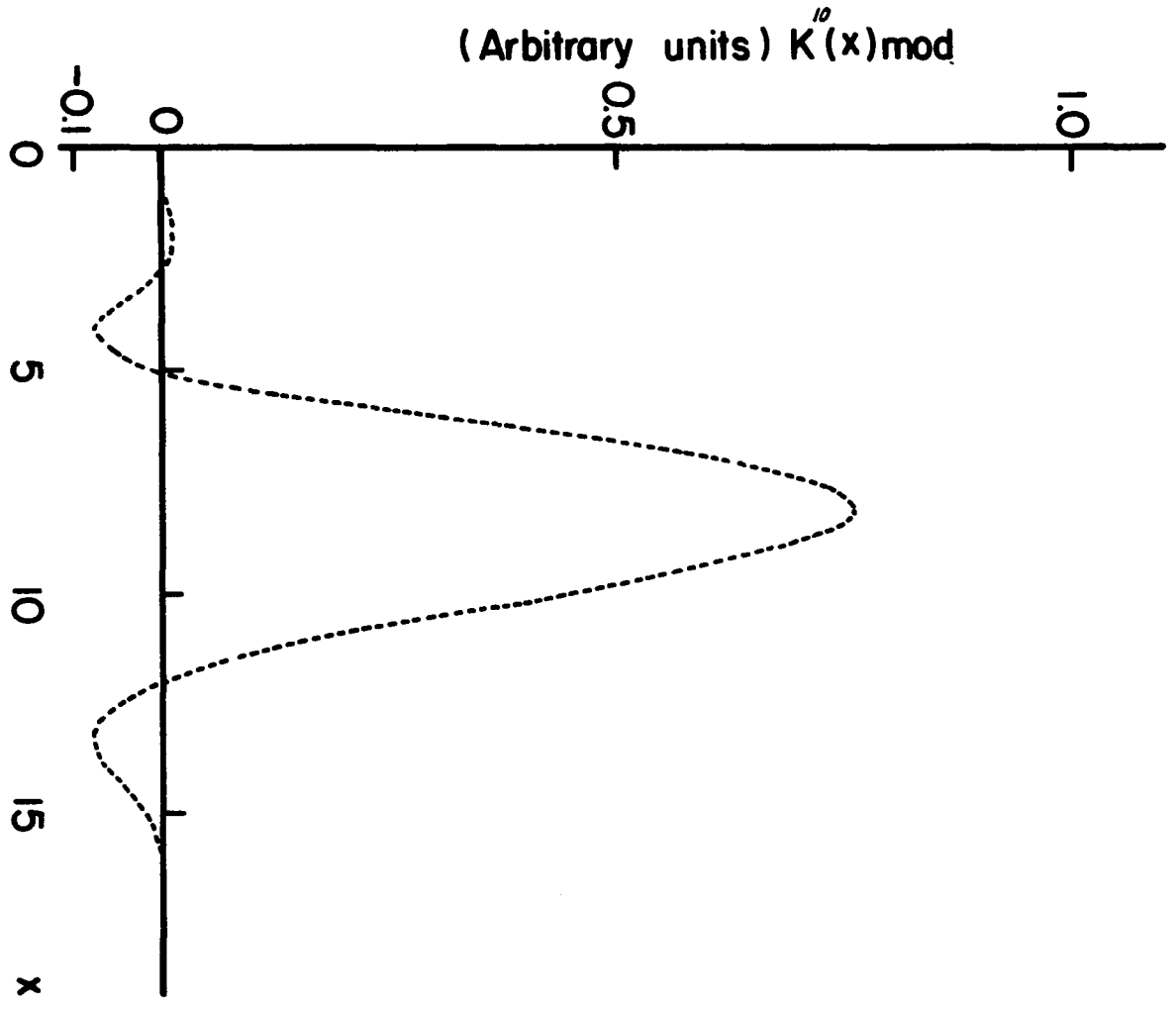


FIG. 64--GRAPH OF KERNEL $K_{\text{mod}}^{10} = \sum_{k=1}^{10} b_k F(x)$

upon the absorbing material.

From the graph the full-width-half-max points are in the ratio $\pi_2/\pi_1 = 10.2/6.2$. To obtain the energy ratio recall that

$$x = \mu \rho t$$

then

$$\pi_2/\pi_1 = \mu_2/\mu_1 = \left(E_2/E_1\right)^{-2.8}$$

$$E_2/E_1 = \left(\mu_1/\mu_2\right)^{0.36} = \left(\frac{6.2}{10.2}\right)^{.36} = 1.15$$

The percent resolution is

$$100 \frac{0.15}{\sqrt{1.15}} = 14\%$$

The main problem with the Laguerre method is the estimation of the derivatives. Newton's forward difference formula and its application in estimating the derivatives are covered in Appendix J.

APPENDIX D

LEGENDRE COEFFICIENTS FOR $\left(\frac{ey}{z_0} e^{-y/z_0}\right)^p$

$$A_N = (4N+3) \left(\frac{e}{z_0}\right)^p \sum_{l=0}^N C_{lN} e^{-b(2l+2)} I \quad y=z-b$$

$$I = \left(\frac{p}{z_0} + 2l + 2\right)^{-(p+1)} p!$$

Using Stirling's formula

$$p! = \sqrt{2\pi p} \left(\frac{p}{e}\right)^p$$

$$A_N = \sum_{l=0}^N \frac{(4N+3)}{\frac{p}{z_0} + 2l + 2} e^{-b(2l+2)} \sqrt{2\pi p} \left(\frac{p/z_0}{\frac{p}{z_0} + 2l + 2}\right)^p$$

APPENDIX E

COEFFICIENTS OF THE EXPANSION OF $\frac{1}{\Gamma(z)}$

$$\frac{1}{\Gamma(z)} = \sum_{l=1}^{\infty} b_l z^l$$

b_1	1
b_2	.57722
b_3	-.6558
b_4	-.042
b_5	.1665
b_6	.0422
b_7	-.00962
b_8	.00722
b_9	-.00117
b_{10}	-.000223

From Abramowitz[13]

APPENDIX F

LAGUERRE COEFFICIENTS FOR $\left(\frac{ez}{a} e^{-z/a}\right)^p$

$$a_m = \int_0^{\infty} \left(\frac{ez}{a} e^{-z/a}\right)^p g_m(z) dz$$

$$g_m = \frac{z e^{-z/2}}{\sqrt{(m+1)(m+2)}} \sum_{l=0}^m C_l^m z^l$$

$$a_m = \frac{\left(\frac{e}{a}\right)^p}{\sqrt{(m+1)(m+2)}} \sum_{l=0}^m C_l^m \int_0^{\infty} z^{(p+l+1)-z\left(\frac{p}{a}+\frac{1}{2}\right)} e^{-z/a} dz$$

$$I = \left(\frac{p}{a} + \frac{1}{2}\right)^{-(p+l+2)} \Gamma(p+l+2)$$

$$a_m = \frac{\left(\frac{e}{a}\right)^p}{\sqrt{(m+1)(m+2)}} \sum_{l=0}^m C_l^m \left(\frac{p}{a} + \frac{1}{2}\right)^{-(p+l+2)} (p+l+1)!$$

Using Stirling's approximation

$$\left(\frac{p}{a} + \frac{1}{2}\right)^{-(p+l+2)} (p+l+1)! =$$

$$\frac{\sqrt{2\pi(p+l+1)} \left[\frac{(p+l+1)}{e}\right]^{(p+l+1)}}{\left[\frac{p}{a} + \frac{1}{2}\right]^{(p+l+2)}}$$

APPENDIX G

LAGUERRE AND LEGENDRE UNFOLDING PROGRAMS

For each unfolding scheme there are two programs: Legendre (LEG1, LEG2), and Laguerre (LAG1, LAG2). LEG1 and LAG2 are used primarily to spectrally analyze data. LAG1 and LEG1 are used primarily to synthesize kernels in μ space. LEG1 was used to synthesize the windows for the rocket borne detector described in the text. The programs are listed in Appendix H.

APPENDIX H

LAG1

```

5 DIM H(40),A(40),B(40)
7 LET Q = 0
10 LET P9 = 3.14159
15 LET U = 5
20 LET E2 = 2.7182
25 LET V = 12
30 LET A = 8
33 LET K = 16
35 LET P1 = 90
38 LET S3 = 9
40 LET E1 = A/E2
45 LET R = .5
50 LET H(1) = 1
60 FOR M = 1 TO K+Q+3
70 LET H(M+1) = H(M)*M
80 NEXT M
90 FOR M1 = 1 TO K+1
100 LET C9 = 0
110 FOR L1 = 1 TO M1
120 LET K1 = P1+L1-1+Q/2
130 LET D1 = (-1) (L1-1)*H(M1+Q)/(H(L1+Q)*H(M1-L1+1))
140 LET C1 = D1*(K1/(P1/E1+E2/2)) K1*SQR(2*P9*K1)/((P1/
(E1*E2)+1/2))
150 LET C9 = C9+C1/H(L1)
160 NEXT L1
170 LET A(M1) = C9/SQR(H(Q+M1)/H(M1))*E1 (-P1)
175 PRINT A(M1)
180 NEXT M1
185 PRINT
190 FOR S = 1 TO K + 1
200 LET C5 = 0
210 FOR L1 = S TO K+1
220 LET C1 = A(L1)*(-1) (S-1)/H(S)
225 LET C1 = C1/SQR(H(Q+L1)/H(L1))
230 LET C5 = C1*H(L1+Q)/(H(S+Q)*H(L1-S+1))+C5
240 NEXT L1
250 LET B(S)=C5
255 NEXT S
257 PRINT
260 FOR X = U TO V STEPR
270 LET L7 = 0
280 FOR S = 1 TO K+1
290 LET L7 = B(S)*X (S-1)+L7
300 NEXT S
305 LET L7 = L7*X (Q/2)*EXP(-X/2)
310 PRINT X,L7
320 NEXT X
330 END

```

LAG2

```

5 DIM H(40),A(40),B(40),G(40)
7 LET Q = 0
10 LET P9 = 3.14159
15 LET U = 5
20 LET E2 = 2.7182
25 LET V = 12
30 FOR L3 = 1 TO K+1
31 READ G(L3)
32 NEXT L3
33 LET K = 16
35 LET P1 = 90
38 LET S3 = 9
40 LET E1 = A/E2
45 LET R = .5
47 FOR A = U TO V STEP R
50 LET H(1) = 1
60 FOR M = 1 TO K+Q+3
70 LET H(M+1) = H(M)*M
80 NEXT M
90 FOR M1 = 1 TO K+1
100 LET C9 = 0
110 FOR L1 = 1 TO M1
120 LET K1 = P1+L1-1+Q/2
130 LET D1 = (-1) (L1-1)*H(M1+Q)/(H(L1+Q)*H(M1-L1+1))
140 LET C1 = D1*(L1/(P1/E1+E2/2)) K1*SQR(2*P9*K1)/((P1/
(E1*E2)+1/2))
150 LET C9 = C9+C1/H(L1)
160 NEXT L1
170 LET A(M1) = C9/SQR(H(Q+M1)/H(M1))*E1 (-P1)
175 PRINT A(M1)
180 NEXT M1
185 PRINT
190 FOR S = 1 TO K+1
200 LET C5 = 0
210 FOR L1 = S TO K+1
220 LET C1 = A(L1)*(-1) (S-1)/H(S)
225 LET C1 = C1/SQR(H(Q+L1)/H(L1))
230 LET C5 = C1*H(L1+Q)/(H(S+Q)*H(L1-S+1))+C5
240 NEXT L1
250 LET B(S) = C5
255 NEXT S
257 PRINT
270 LET L7 = 0
280 FOR S = 1 TO K+1
290 LET L7 = B(S)*G(S)+L7
300 NEXT S
310 PRINT A,L7
320 NEXT A
325 DATA
330 END

```

LEGL

```

2 LET A2 = 2
3 LET A1 = 0
4 DIM A(50),C(30,30)
5 LET K = 120
7 DIM G(30)
8 DIM D(34)
10 LET A = .5
13 LET H = 1
15 LET M = 17
17 LET B = 1
20 LET U = .1
25 LET V = 1
30 LET R = .1
40 LET P1 = 3.14159265
45 LET E = 2.7182818
50 FOR N1 = 1 TO M+1
60 FOR L1 = 1 TO N1
65 LET N2 = N1-1
70 LET F2 = 1
75 LET L2 = L1-1
80 FOR K1 = 1 TO 2*N2+1
85 LET K2 = K1-1
90 LET F2 = F2*(2*L2+2*N2+2-K2)/(2*N2+1-K2)
100 NEXT K1
110 LET F1 = 1
115 IF N1-L1 = 0 THEN 137
120 FOR K1 = 1 TO N1-L1
125 LET K2 = K1-1
130 LET F1 = F1*(2*N2+1-K2)/(N2-L2-K2)
133 NEXT K1
137 LET C(L1,N1)=F2*F1*(-1) (N1-L1)/2 (2*N2+1)
140 NEXT L1
150 NEXT N1
160 FOR N1 = 1 TO M+1
170 LET F3 = 0
180 FOR L1 = 1 TO N1
185 IF A2 = 1 THEN 205
190 LET F4 = K/A+(2*(L1-1)+2)
200 LET F3 = F3+C(L1,N1)*SQR(2*P1*K)/F4*(K/A/F4) K*EXP(-A1*
(2*(L1-1)+2))
203 GO TO 210
205 LET F3 = F3+C(L1,N1)*EXP(-(A+A1)*(2*(L1-1)+2))
210 NEXT L1
220 LET A(N1) = (4*(N1-1)+3)*F3
230 NEXT N1
234 FOR L1 = 1 TO M+1
240 LET L7 = 0
245 FOR N1 = L1 TO M+1
250 LET L7 = A(N1)*C(L1,N1)+L7
255 NEXT N1
260 LET D(L1) = L7*EXP(-A1*(2*(L1-1)+1))

```

```
263 PRINT D(I1)
265 NEXT I1
267 FOR X = U TO V STEP R
270 LET L6 = 0
275 FOR I1 = 1 TO M+1
280 LET L6 = D(I1)*EXP(-X*(2*(I1-1)+1))+L6
290 NEXT I1
340 PRINT X,L6
350 NEXT X
508 END
```

LEG2

```

2 LET A2 = 1
3 LET A1 = 0
4 DIM A(50),C(30,30)
5 LET K = 100
7 DIM G(30)
8 DIM D(34)
13 LET H = 1
15 LET M = 7
17 LET B = 1
20 LET U = .1
25 LET V = 1
30 LET R = .1
31 FOR L3 = 1 TO M+1
32 READ G(L3)
33 NEXT L3
35 FOR A = U TO V STEP R
40 LET P1 = 3.14159265
45 LET E = 2.7182818
47 LET Z1 = .3
48 LET Z2 = .7
50 FOR N1 = 1 TO M+1
60 FOR L1 = 1 TO N1
65 LET N2 = N1-1
70 LET F2 = 1
75 LET L2 = L1-1
80 FOR K1 = 1 TO 2*N2+1
85 LET K2 = K1-1
90 LET F2 = F2*(2*L2+2*N2+2-K2)/(2*N2+1-K2)
100 NEXT K1
110 LET F1 = 1
115 IF N1-L1 = 0 THEN 137
120 FOR K1 = 1 TO N1-L1
125 LET K2 = K1-1
130 LET F1 = F1*(2*N2+1-K2)/(N2-L2-K2)
133 NEXT K1
137 LET C(L1,N1)=F2*F1*(-1) (N1-L1)/2 (2*N2+1)
140 NEXT L1
150 NEXT N1
160 FOR N1 = 1 TO M+1
170 LET F3 = 0
180 FOR L1 = 1 TO N1
185 IF A2 = 1 THEN 205
190 LET F4 = K/A+(2+(L1-1)+2)
200 LET F3=F3+C(L1,N1)*SQR(2*P1*K)/F4*(K/A/F4) K*EXP(-A1*
      (2*(L1-1)+2))
203 GO TO 210
205 LET F3 = F3+C(L1,N1)*EXP(-(A+A1)*(2+(L1-1)+2))
210 NEXT L1
220 LET A(N1) = (4*(N1-1)+3)*F3
230 NEXT N1
234 FOR L1 = 1 TO M+1
240 LET L7 = 0

```

```
245 FOR N1 = L1 TO M+1
250 LET L7 = A(N1)*C(L1,N1)+L7
255 NEXT N1
260 LET D(L1) = L7*EXP(-A1*(2*(L1-1)+1))
265 NEXT L1
270 LET L6 = 0
275 FOR L1 = 1 TO M+1
280 LET L6 = D(L1)*G(L1)+L6
290 NEXT L1
340 PRINT A,L6
350 NEXT A
400 DATA
508 END
```

APPENDIX I

DERIVATIVES OF THE FUNCTION e^{-e^y}

Let the N^{th} derivative of $F = e^{-e^y}$ be F^N

assume
$$F^N = F \sum_{p=1}^N a_p^N x^p \quad x = e^y$$

$$F^{N+1} = F' \sum_{p=1}^N a_p^N x^p + F \sum_{p=1}^N a_p^N p x^{p-1}$$

$$F' = -F x$$

$$F^{N+1} = -F \sum_{p=1}^N a_p^N x^{p+1} + F \sum_{p=1}^N a_p^N p x^{p-1}$$

let $m = p+1$

$$F^{N+1} = F \left(- \sum_{m=2}^N a_{m-1}^N x^m + \sum_{p=2}^N a_p^N p x^{p-1} + (-1)^{N+1} - x \right)$$

letting $N \rightarrow N+1$,

the recursion rules are:

$$a_1^N = -1$$

$$a_N^N = (-1)^N$$

$$a_m^N = (m a_m^{N-1} - a_{m-1}^{N-1})$$

where $m \neq 1, N$

APPENDIX J

NUMERICAL DETERMINATION OF DERIVATIVES

From Abramowitz[13] Newton's forward difference formula for interpolation is:

$$1) \quad f(a_0 + hp) = \sum_{m=0}^s \binom{p}{m} \Delta_0^m$$

Δ_0^m is the m^{th} forward difference.

$$\Delta_0^m = \sum_{j=0}^m \binom{m}{j} F(a_0 + m - j)$$

Differentiating 1)

$$\frac{d^N}{dh^N} f(a_0 + hp) = \frac{1}{h^N} \sum_{m=0}^s \frac{d^N}{dp^N} \binom{p}{m} \Delta_0^m$$

The following recursion relation for derivatives of $\binom{p}{m}$ has been deduced.

$$(N+1) \frac{d^l}{dp^l} \binom{p}{N+1} = \left[(p-N) \frac{d^l}{dp^l} + l \frac{d^{l-1}}{dp^{l-1}} \right] \binom{p}{N}$$

APPENDIX K

CALCULATION OF ONE POINT OF
DECOMPOSITION GRAPH OF $Fe^{55}-Co^{57}$

The computer program Leg2 computes the following:

t_0 = thinnest aluminum
foil (0.005 cm)

$$Z_0 = \mu_0 \rho t_0$$

in this region

$$\rho = 2.7 \text{ gm/cm}^3$$

$$\mu_0 = c E_0^{-2.8}$$

$$E_0 \text{ in keV}$$

$$c = 0.05 \times 10^{-3}$$

$$1) Z_0 = c E_0^{-2.8} \rho t_0$$

$$A_N = \left(\frac{30}{e}\right)^{30} \sqrt{60\pi} (4N+3) \left(\frac{e}{Z_0}\right)^{30} \sum_{l=0}^N C_{lN} \left(\frac{30}{Z_0} + 2l + 2\right)^{-3l}$$

$$a'_s = \sum_{N=s}^4 A_N C_{sN}$$

$$C_{sN} = \binom{25+2N+2}{2N+1} \binom{2N+1}{N-s} \frac{(-1)^{N-s}}{2^{2N+1}}$$

S ranges from 0 to 4

the window output

$$W_0'(E_0) = \sum_{l=0}^4 Q_l'(E_0) D[(2l+1)t_0]$$

$D(t) \sim$ DATA in (cts/.01 sec)

$$D(t_0) = 0.509$$

$$D(3t_0) = 0.370$$

$$D(5t_0) = .335$$

$$D(7t_0) = .318$$

$$D(9t_0) = .295$$

a^1 s are dimensionless

$$a_0^1 = -.5322$$

$$a_1^1 = +3.561$$

$$a_2^1 = 10.712$$

$$a_3^1 = +25.783$$

$$a_4^1 = -20.572$$

$$E_0 = 7.5 \text{ kev (eq. 1)}$$

$$\begin{aligned} W_0^1(7.5) &= (.509)(-.5322) + (.370)(3.561) \\ &+ (.335)(-10.712) + (.318)(25.783) \\ &+ (.295)(-16.464) \end{aligned}$$

$$\begin{aligned} W_0^1(7.5) &= -.2708 + 1.317 - 3.589 \\ &+ 8.199 - 4.856 \end{aligned}$$

$$W_0^1(75) = 0.8$$

See Figure 22 for the results of this computation.